UC San Diego

UC San Diego Electronic Theses and Dissertations

Title

Modeling of Cerebrospinal Fluid Flow using Quantitative MRI for Clinical Application

Permalink

https://escholarship.org/uc/item/9mc5c8wd

Author

Sincomb, Stephanie

Publication Date

2022

Peer reviewed|Thesis/dissertation

eScholarship.org Powered by the California Digital Library
University of California

UNIVERSITY OF CALIFORNIA SAN DIEGO

Modeling of Cerebrospinal Fluid Flow using Quantitative MRI for Clinical Application

A dissertation submitted in partial satisfaction of the
requirements for the degree Doctor of Philosophy

in

Engineering Sciences with a Specialization in Multi-Scale Biology

by

Stephanie Sincomb

Committee in charge:

Professor Antonio L. Sánchez, Chair
Professor Lawrence Frank
Professor Victor Haughton
Professor Alexander Norbash
Professor Eugene Pawlak
Professor Lonnie Petersen

2022

Copyright

Stephanie Sincomb, 2022

All rights reserved.

The Dissertation of Stephanie Sincomb is approved, and it is acceptable in quality and form for publication on microfilm and electronically.

University of California San Diego

2022

DEDICATION

This dissertation is dedicated to my best friend and the love of my life, Troy Sincomb.

TABLE OF CONTENTS

LIST OF FIGURES

LIST OF TABLES

ACKNOWLEDGEMENTS

I am forever indebted to each person that has been involved in my PhD journey, whether small or large. It has been a unique journey that wouldn't be the same without each person.

I want to first and formally thank the chair of my committee and principal adviser, Professor Antonio Sánchez, for his rigor and support throughout my time at UCSD even prior to starting the graduate program.

Thank you to all of my collaborators that have made the research possible. Professor Wilfried Coenen, for providing an incredible amount of help and new ideas. Professor Cándido Gutiéerrez-Montes, for his help and support. Professor Carlos Martínez-Bazán, for offering wonderful insight into experimental design. Dr. Kevin King, for being the original radiologist to invite our, sometimes impractical, ideas to the MRI scan room. Professor Matthew Borzage, for offering expertise in MRI sequences and keeping it practical. Dr. Victor Haughton, an incredible neuroradiologist, who has welcomed our engineering perspective and has been driven to propel it into the medical community. He has also been a wonderfully kind and caring individual.

Thank you to all of my other members of my committee: Professor Lawrence Frank, who is also my Interfaces co-mentor, Professor Lonnie Petersen, Professor Alexander Norbash and Professor Eugene Pawlak.

Thank you to all those who were there from the start in the SME building: Ernesto, Amy, Cathleen, Toni, Alex, Maidu, Arijit, Miriam, Jenna and Jose. And to those who joined later: Obed and Emily. To Ernesto, you are a wonderful mentor and I am thankful I got to share an office with you and many memories filled with laughter and sometimes tears.

Thank you to all my friends and family who provided the love and support I needed to succeed. My sisters, Melissa and Rebecca, my nieces, Destiny and Amber, and nephew, Israel and the entire Sincomb family. My best friend, Desirae, and to all my close friends:

Connor, Arlene, Taylor, Gillian, Brandt, Kale and Mark.

To Troy, I feel so fortunate to have you beside me. You have been my source of true joy in life. You and I can conquer anything. Thank you for being all that you are.

I would like to also acknowledge Professor Juan Lasheras, who passed away early last year. He is the person responsible for me pursuing a PhD and providing me an avenue for it. His kindness and utmost concern for my success pushed me forward and I can only hope that this dissertation would have made him proud.

Chapter 2, in full with slight modifications, is a reprint of the material as it appears in the Journal of Fluid Mechanics, 2020. Sincomb, Stephanie.; Coenen, Wilfried; Sánchez, Antonio and Lasheras, Juan C. The dissertation author was the primary author of this paper.

Chapter 3, in full with slight modifications, is a reprint of the material as it appears in the American Journal of Neuroradiology, 2021. Sincomb, Stephanie; Coenen, Wilfried; Criado-Hidalgo, Ernesto; Wei, Ke; King, Kevin; Borzage, Matthew; Haughton, Victor and Sánchez, Antonio and Lasheras, Juan C. The dissertation author was the primary author of this paper.

Chapter 4, in part is currently being prepared for submission for publication. Sincomb, Stephanie; Singh, Akansha; Coenen, Wilfried; Gutiérrez-Montes, Cándido; Martínez-Bazáan, Carlos; and Sánchez, Antonio. The dissertation author was the primary author of the material.

Chapter 5, in full with slight modifications, is a reprint of the material as it appears in the Journal of Fluid Mechanics, 2022. Sincomb, Stephanie; Coenen, Wilfried; Gutiérrez-Montes, Cándido; Martínez-Bazáan, Carlos; Haughton, Victor and Sánchez, Antonio. The dissertation author was the primary author of this paper.

Chapter 6, in part is currently being prepared for submission for publication. Sincomb, Stephanie; Coenen, Wilfried; Gutiérrez-Montes, Cándido; Martínez-Bazáan, Carlos; and Sánchez, Antonio. The dissertation author was the primary author of the

material.

Finally, I am grateful to the Bill and Melissa Gates Foundation for their continuous support through a Gates Millennium Scholar fellowship. The work reported in Chapters 2 and 4 was funded by the National Science Foundation through grant no. 1853954. The work reported in Chapters 3, 5 and 6 was funded by the National Institute of Neurological Disorders and Stroke through contract no. 1R01NS120343-01.

VITA

2012-2022	Gates Millennium Scholar, University of California San Diego
2017	Aerospace Engineering (B.S.), University of California- San Diego
2018	Mechanical Engineering (M.S), University of California San Diego
2018-2022	Graduate Student Researcher, University of California San Diego
2020	Teaching Assistant, University of California San Diego
2022	Ph.D. in Mechanical Engineering with Specialization in Multi-Scale Biology, University of California San Diego

PUBLICATIONS

Sincomb, Stephanie; Coenen, Wilfried; Gutiéerrez-Montes, Cándido; Martínez-Bazán, Carlos; Haughton, Victor; Sánchez, Antonio. "A one-dimensional model for the pulsating flow of cerebrospinal fluid in the spinal canal" *Journal of Fluid Mechanics* (2022).

Sincomb, Stephanie; Coenen, Wilfried; Criado-Hidalgo, Ernesto; Wei, Ke; King, Kevin.; Borzage, Matthew; Haughton, Victor; Sánchez, Antonio; Lasheras, Juan C. "Transmantle Pressure Computed from MR Measurements of Aqueduct Flow and Dimensions" *American Journal of Neuroradiology* (2021).

Sincomb, Stephanie; Coenen, Wilfried; Sánchez, Antonio; Lasheras, Juan C. "A model for the oscillatory flow in the cerebral aqueduct" *Journal of Fluid Mechanics* (2020).

Coenen, Wilfried; Gutiéerrez-Montes, Cándido; Sincomb, Stephanie, Criado-Hidalgo, Ernesto; Wei, Ke; King, Kevin; Haughton, Victor; Martínez-Bazán, Carlos; Sánchez, Antonio; Lasheras J C. "Subject-specific evaluation of CSF bulk flow in the spinal canal: recirculating flow patterns and implications for ITTD drug dispersion". *American Journal of Neuroradiology* (2019).

Gutiéerrez-Montes, Cándido; Coenen, Wilfried; Vidorreta, Marta; Sincomb, Stephanie; Martínez-Bazán, Carlos; Sánchez, Antonio; Haughton, Victor; "Effect of normal breathing on the movement of CSF in the spinal subarachnoid space". *American Journal of Neuroradiology* (submitted).

Sincomb, Stephanie; Singh, Akansha; Coenen, Wilfried; Gutiéerrez-Montes, Cándido; Martínez-Bazán, Carlos; Sánchez, Antonio. "In-vitro Model of the Oscillatory CSF flow in the Cerebral Aqueduct" (In preparation).

Sincomb, Stephanie; Coenen, Wilfried; Gutiéerrez-Montes, Cándido; Martínez-Bazán, Carlos; Sánchez, Antonio. "Validation of the one-dimensional CSF flow model using lumbar pressure monitoring." (In preparation).

ABSTRACT OF THE DISSERTATION

Modeling of Cerebrospinal Fluid Flow using Quantitative MRI for Clinical Application

by

Stephanie Sincomb

Doctor of Philosophy in Engineering Sciences with a Specialization in Multi-Scale Biology

University of California San Diego, 2022

Professor Antonio L. Sánchez, Chair

Characterization of cerebrospinal fluid (CSF) dynamics in the central nervous system is fundamental for the study of CSF-related disorders, such as normal pressure hydrocephalus, Chiari malformation, and syringomyelia, which can help guide clinical diagnosis and treatment therapy. In this thesis, phase contrast, a non-invasive magnetic resonance imaging (MRI) technique that can map the phase accrual of the moving fluid region to velocity, is combined with rigorously derived simplified models of the CSF motion to enable patient-specific quantitative descriptions of the fluid flow and associated pressure variations for clinical use. Attention is focused on two specific problems, namely, flow in the cerebral aqueduct, a slender canal connecting the third and fourth ventricles of the

brain, and flow in the spinal canal. In the former case, special attention is given to the relation between the predicted flow rate and the interventricular pressure variation, which is subsequently used in a volunteer study to obtain indirect evaluations of the transmantle pressure from direct MRI flow measurements corresponding to 77 subjects. The model for the pulsating viscous motion in the spinal canal assumes a linearly elastic compliant tube of slowly varying section, with a Darcy pressure-loss term included to model the fluid resistance introduced by the microanatomy. As shown by the preliminary computations presented here, this simple one-dimensional model can serve as a basis for quantitative analyses targeting predictions of intracranial pressure temporal fluctuations based on MRI measurements of spinal-canal anatomy and CSF flow rate. Future directions are proposed concerning both flow problems, including further validation exercises involving in-vitro and in-vivo experiments.

Chapter 1

Introduction

1.1 Cerebrospinal fluid (CSF)

Cerebrospinal fluid (CSF) is a clear, colorless fluid with water-like properties (i.e. density of $\rho \simeq 10^3$ kg/m^3 and kinematic viscosity $\nu \simeq 0.71 \times 10^{-6}$ m^2/s) that fills the ventricles of the brain and the subarachnoid space (SAS) surrounding the brain and the spinal cord. This fluid plays a dual mechanical and physiological function in the body. The mechanical function of CSF is to cushion the brain within the skull and serve as a shock absorber. The physiological function of CSF is to maintain electrolyte levels, circulate nutrients and chemicals filtered from the blood, transport hormones and remove metabolic waste products. This fluid essentially helps the body remain in homeostasis and maintains metabolism [1].

CSF is primarily produced in the choroid plexuses of the ventricular system. The choroid plexus consists of two components, namely, the highly vascularized connective tissue of the pia mater and a plexus of choroid epithelium which forms the blood-CSF barrier. Synthesis of CSF involves diffusion and active transport from the arterial blood supply, resulting in a constant production rate of 0.2-0.7 ml/min [2]. CSF is mainly reabsorbed by arachnoid granulations which are protrusions of the arachnoid mater into the venous sinuses with villi that increase the surface area. CSF diffuses through the walls via a valvular pressure-driven mechanism. Most villi are located in the superior sagittal

and transverse sinuses. There are additional routes of CSF drainage through the olfactory mucosa, cranial nerve (optic, trigeminal, and facial nerves) sheaths, and into the lymphatic vessels around the cranial cavity [3, 4]. In healthy humans, CSF secretion and reabsorption are balanced, resulting in a constant mean intracranial pressure (ICP) of approximately 7-15 mmHg. Due to the fact that the locations of the sources (choroid plexuses) and sinks (arachnoid granulations) are not collocated, flow occurs through the ventricular system, albeit at a very slow rate. Most of the production occurs in the lateral ventricles where it travels through the Foramina of Monroe into the third ventricle. From the third ventricle, it flows through the cerebral aqueduct into the fourth ventricle where it outflows to the subarachnoid space (SAS) via the foramen of Magendie and the lateral foramina of Luschka. Of course, this is the traditional description of the CSF flow within the brain and it is understood to be much more complex [5], but provides a general understanding that is useful for the remaining chapters of this dissertation.

In addition to this slow motion between the production and consumption sites inside the cranial cavity, a faster oscillatory motion is induced by arterial pulsations. Specifically, the blood flow in and out of the cranial vault during each heartbeat causes the intracranial pressure to also fluctuate periodically with a frequency determined by the heart rate. This time-dependent pressure fluctuations drive the pulsatile motion of CSF in the cranial cavity and also along the spinal canal that surrounds the spinal cord. There are additional effects that modulate the CSF flow such as respiration, a subject's posture, jugular venous pressure, and physical activity [1]. For this dissertation, we will focus solely on the cardiac-driven motion of the CSF in the CNS. There are various imaging techniques available to characterize this cardiac-driven fluid flow. One technique known as phase contrast MR imaging will be used in this dissertation. Relevant previous contributions are reviewed in the following paragraphs.

The earliest study for assessment and quantification of the CSF fluid dynamics in healthy individuals using MR imaging was conducted by Feinberg and Mark (1987).

Their observations revealed that vascular-driven movement of the brain is the mechanism responsible for CSF pumping, a finding that challenged the earlier belief that the CSF is pumped by the expansion of the choroid plexus [6]. The role of vascular-driven motion was also confirmed later by studies of the CSF and blood flow using phase-contrast cine MRI (PC-MRI) [7, 8]. This imaging technique was used in studies pertaining to different regions of the central nervous system (CNS) including the cerebral SAS, spinal canal [9] and cerebral aqueduct [10].

In connection with the flow along the spinal canal, PC-MRI studies have shown that the velocity amplitude, which is the largest at the foramen magnum, decreases down along the length of the canal to reach a zero value at the closed-end sacral region [11, 12]. It has also been observed in many radiological studies that, in addition to the pulsatility of the arterial blood flow supplying the cranial vault, the respiration also produces a modulation of the intracranial pressure, resulting in a somewhat smaller additional oscillation of the CSF in the spinal canal at a lower frequency (12–18 cycles per minute in adults) [13, 14].

In addition to the fast pulsating motion driven by the cardiac and respiratory cycles, there exists a slow bulk motion, first observed in Di Chiro's experiments [15, 16], and later confirmed by numerous radiological observations. These studies revealed that a tracer injected in the lumbar region is detected moving upwards and reaching the basal cisterns of the cranial vault in 15–20 min [17], thereby suggesting a bulk flow rate with velocities on the order of 1 cm/min. Although not of direct interest to our work, it is worth mentioning that this bulk motion has recently been investigated by asymptotic analyses, which showed that steady streaming and Stokes' drift are responsible for the slow bulk motion [18]. The resulting bulk flow patterns have been shown to vary from individual to individual and with posture along the canal [19]. On-going quantitative studies regarding bulk flow are addressing the modulation of the intracranial pressure by the respiratory cycle, which results in a smaller additional component of the oscillation of the CSF in the spinal canal at a lower frequency.

Besides flow measurements in the spinal canal, studies have also used PC-MRI in regions of the brain, with most reports investigating the changes in the CSF flow that may occur due to neurological diseases such as normal pressure hydrocephalus (NPH) [20–25]. For example, one study found that a stroke volume (SV) in the cerebral aqueduct greater than or equal to 42 μL may indicate NPH patients who have a higher probability of improvement after shunting [20]. Phase-contrast MRI has shown NPH patients exhibit a higher stroke volume in the aqueduct as compared to healthy controls [20–22, 24, 25], but this may also depend on the extent of disease progression [23]. It has also been argued that the net flow rate is retrograde (toward the third ventricle) in those with NPH [26].

Previous modeling efforts addressing the CSF flow in the central nervous system have extended the understanding of the associated dynamics. Some studies utilized phase-contrast imaging along with computational and mathematical modeling to provide insight into CSF-related disorders. There are studies that employ computational fluid dynamics (CFD) [27–29], lumped-parameter models [30–32] and fluid-structure interaction [33]. Despite these previous efforts, there are still many open questions regarding the flow, as discussed in detail in a recent review [34]. Although previous models have contributed to the overall knowledge regarding the motion of CSF, which is critical for improving the diagnosis and treatment of CSF-related disorders, they are fundamentally limited in some ways. For example, in CFD subject-specific models, the use of computationally expensive and time-consuming CFD simulations is not well suited for clinical applications interested in studying a large subject cohort. Some of the models also critically depend on parameters such as brain tissue mechanical properties, which cannot be determined with sufficient accuracy.

Instead of relying on CFD, our study exploits simplifications stemming from the disparity of length and time scales present in the problem to contribute to an increased understanding of the CSF flow dynamics and develop simplified descriptions that can be integrated into clinical studies. Our approach combines PC-MRI measurements of CSF

flow rate with systematically derived flow models for the cerebral aqueduct and spinal canal. The model for the oscillatory CSF flow in the aqueduct is to be discussed in Chapter 2 [35]. Chapter 3 presents the implementation of the model in a large study cohort with wide age range [36]. Chapter 4 presents preliminary work concerning the validation of the cerebral aqueduct model using an in-vitro experimental setup. A one-dimensional model for the pulsating flow of cerebrospinal fluid in the spinal canal is reported in Chapter 5 [37]. Chapter 6 addresses additional validation efforts regarding the model developed for the spinal canal.

The rest of this chapter section discusses the phase-contrast MR flow imaging technique employed in our investigation, including a short introduction to magnetic resonance fundamentals and imaging.

1.2 MR fundamentals and imaging

We begin with a brief description of magnetic resonance imaging (MRI). This imaging modality has been central to several CSF flow studies described previously. Although the description here will not be detailed, it should provide the key aspects to understanding the physics behind MR imaging and thus the following description of the MRI imaging technique, known as phase-contrast (PC) MRI, which is used in our modeling efforts.

1.2.1 Basic principles of MR

In the most fundamental sense of MR imaging, low-frequency radio waves are transmitted into tissue and a signal is received from magnetized spins (protons) in the body. The magnetic spin of interest in most MR imaging is that of the hydrogen nucleus, which is a single, positively charged proton and spins about its axis. A hydrogen proton has two energy states denoted -1/2 and +1/2, which characterize the direction in which it spins and its associated magnetic field. It is important to realize that any proton, electron,

and neutron possess spin. When in even pairs the manifestations of spin are canceled, but when uneven, they exhibit angular momentum and hence spin. The spin is what generates a magnetic field and in turn, causes the nucleus to have a magnetic dipole moment.

Hydrogen protons also just so happen to be abundant in the human body and exist in all tissue at different densities. However, since they are randomly orientated, their resulting magnetic fields cancel out, in other words, the net magnetization is zero. The protons are essentially bar magnets, and when placed in an external magnetic field (denoted as B_0), most will line up in the direction of the magnetic field causing the net magnetization to point in the direction of B_0. The temporal evolution of the net magnetization shows an exponentially growing curve where the time it takes to achieve the final net magnetization (or longitudinal magnetization) depends on the tissue being imaged and the strength of the magnet. The resulting longitudinal magnetization of the spins is the source that will provide a signal used to obtain MR images.

An MRI scanner is a giant magnetic field that is typically greater than 1 Tesla (T). 1.5 T, for example, is 30,000 times stronger than the Earth's magnetic field. This is used to generate the net magnetization of the hydrogen spins in the body. The spins will also not only spin about their axis but will also precess (or rotate) about the axis of the external magnetic field. Precession is equivalent to the proton behaving like a spinning top about the axis of the external magnetic field. The rate of this precession is given by the Larmor equation:

$$\omega = \gamma B_0 \tag{1.1}$$

where ω is the angular precessional frequency, γ is the gyromagnetic ratio (dependent on the nucleus), and B_0 the strength of the magnetic field. Now we can exploit this process of spin precession by introducing a radiofrequency (RF) wave, which is electromagnetic, at the same frequency of the precessing spins resulting in resonance or addition of energy into the spins. Some spins will change their alignment and after the RF pulse, generate a

signal as they return to their original alignment which induces a voltage signal called free induction decay (FID). This is the MR signal measured.

However, to differentiate spatially where the signals are coming from requires the use of gradient coils. Specifically, if the strength of the magnetic field is altered in such a way that the spins at different locations precess at different frequencies (via gradient coils), then the spectral analysis would give information about the spatial location of the spins. Therefore, we apply an RF pulse multiple times while varying the gradients which produces multiple FIDs. The information from multiple FIDs can be combined to create an image. Thus, the process of obtaining an image using MRI can be summarized as follows:

1. Hydrogen protons in the body behave like bar magnets that align when placed in an external magnetic field (i.e. MRI scanner) generating a longitudinal magnetization and precess about the axis of the field.

2. A radiofrequency wave is transmitted to the spins at the precessional frequency (or resonant frequency) of the spins to flip the longitudinal magnetization and generate a signal.

3. To obtain spatial information of where the received signal is coming from, gradient coils in the MR scanner are used.

1.2.2 Phase contrast MRI (PC-MRI)

Local spin magnetization can be described in terms of magnitude and phase. The basis for phase-contrast (PC) MR imaging is to use encoding magnetic field gradients in a manner that induces flow-dependent phase accrual, which is illustrated in Figure 1.1. For linear field gradients, the amount of phase shift is proportional to the velocity of the spins being imaged. Stationary tissue phase shifts can be compensated by using a bipolar gradient, as illustrated in Figure 1.2. Phase shifts are measured between $\pm\pi$. The

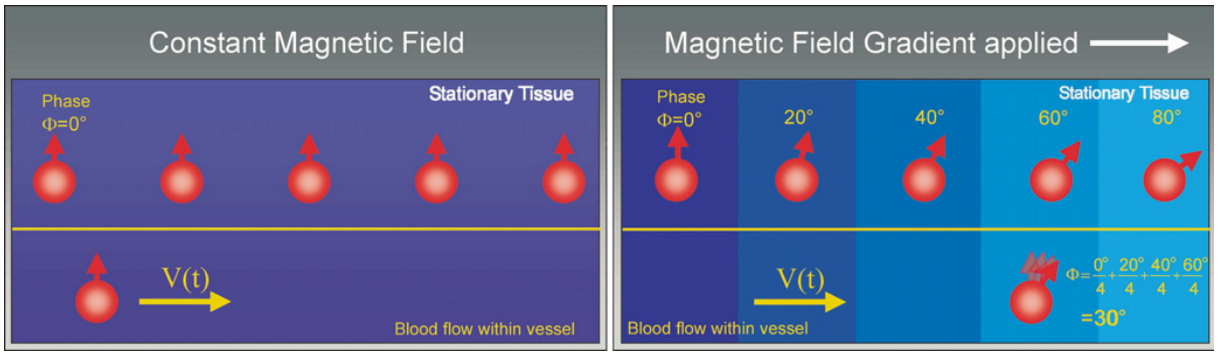

Figure 1.1. Diagrams show that spins moving along an external magnetic field gradient acquire a difference in the phase of their rotation (right), whereas nonmoving spins do not (left). The amount of phase difference is proportional to the velocity of the moving spin. t = time, V = velocity, ϕ = phase shift. Reproduced, with permission, from Lotz, J., Meier, C., Leppert, A., & Galanski, M., Radiographics, 2022, 22, p.652, Copyright 2002 by the Radiological Society of North America.

needed scaling requires some knowledge of the peak velocity of the flow that is being measured. This parameter choice is known as the velocity encoding (VENC) and defines the maximum and minimum detectable velocity encoded in the sequence. To resolve phase-contrast measurements in time, the acquisition is often synchronized (or gated) to the cardiac cycle (CINE). There are two gating techniques for cardiac cycle sampling, prospective and retrospective. Both require a trigger signal, which can be acquired through an EKG (electrocardiography) or from a PPG (photoplethysmography). In prospective gating, acquisition only starts after detection of a desired physiologic event such as an R wave. This ensures difficulty in sampling the entire cycle. IN retrospective gating, on the other hand, measurements are made continuously and the EKG (or PPG) signal is used to sort the measurements into their position along the cardiac cycle. The data is then interpolated to provide a mean cardiac cycle signal [38]. In general, retrospective gating provides more accurate results than prospective gating [39] and thus will be implemented in all imaging protocols used in this thesis.

Although PC-MRI has been validated in phantom studies, there are several limitations to this imaging technique. Some common mistakes in phase-contrast include a choice

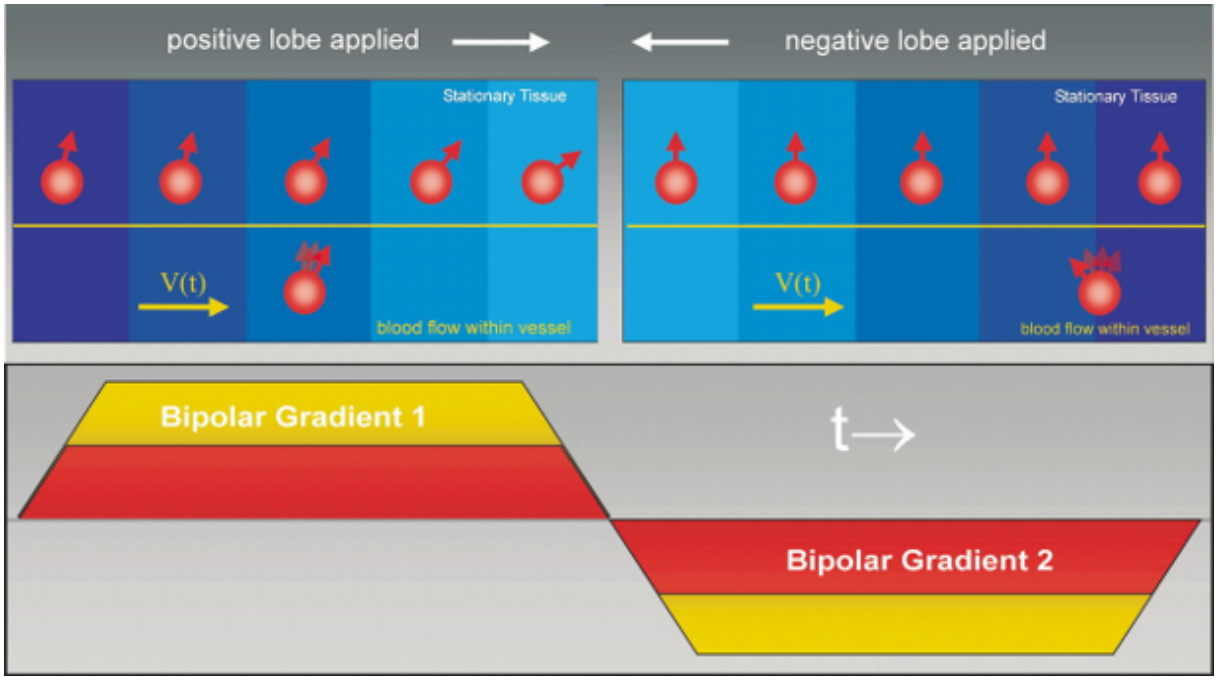

Figure 1.2. Principle of phase-contrast sequences available in most clinical MR imaging units. Diagram shows that two acquisitions are performed, each one with all parameters kept constant except for the flow-sensitizing bipolar gradients. The data of the two acquisitions are subtracted. The effective flow encoding is achieved by means of the difference in the bipolar gradients of the two acquisitions. This technique eliminates all phase shifts induced by imaging gradients. t = time, V = velocity. Reproduced, with permission, from Lotz, J., Meier, C., Leppert, A., & Galanski, M., Radiographics, 2022, 22, p.652, Copyright 2002 by the Radiological Society of North America.

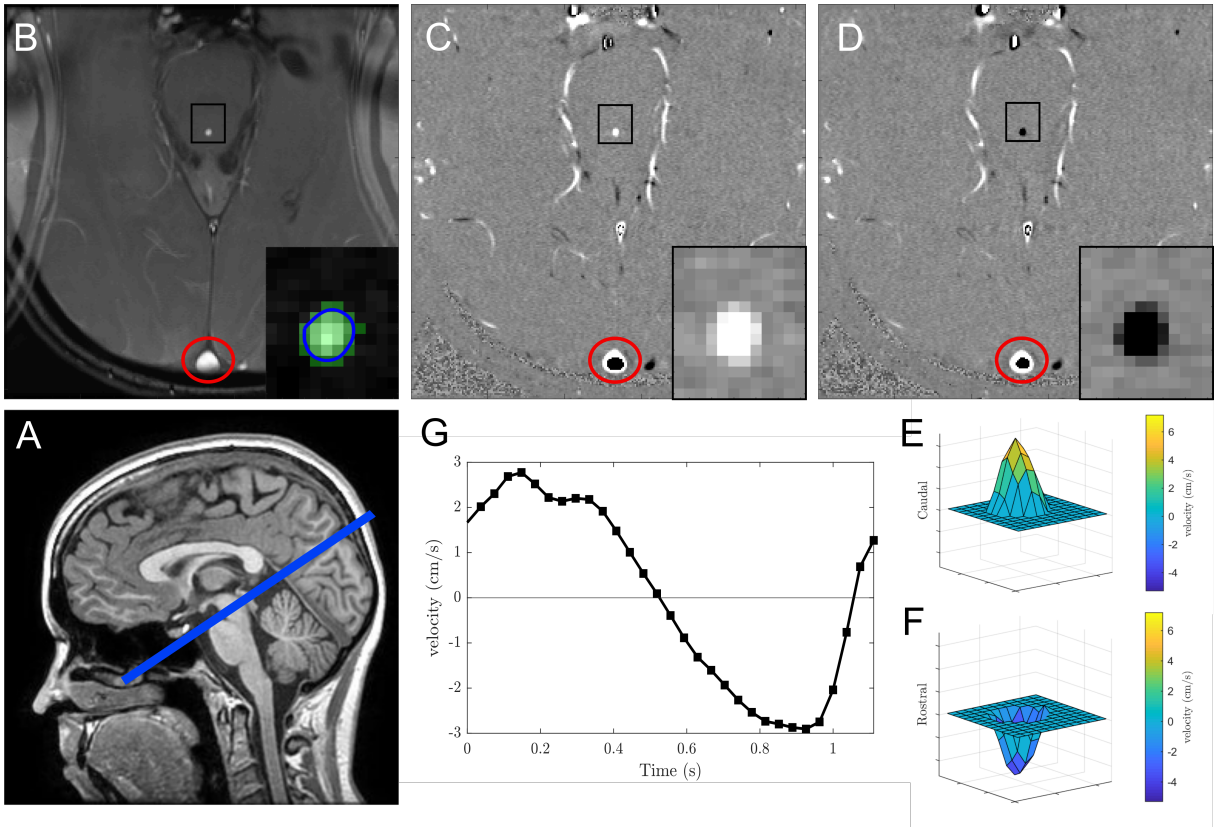

Figure 1.3. A) Sagittal MR image of midline brain showing cerebral aqueduct oblique imaging plane (blue line). B) Magnitude image of oblique phas- contrast MRI of the cerebral aqueduct with the inset showing the area of the aqueduct. C-D) Phase images at two points along the cardiac cycle with an inset showing area where white and black pixels correspond to caudal and rostral flow, respectively. E-F) Surface figures of the phase converted to velocity and G) the average velocity in the cross-sectional area. Note that the red circles mark the superior sagittal sinus in the phase images with observable aliasing (phase wrap) due to the wrong VENC.

of VENC that is too high. This results in poor sensitivity to the velocity of the moving fluid region of interest. On the other hand, if the chosen VENC is too low, the resulting phase images are phase wrapped also known as aliasing. An example of aliasing is shown in phase images of Figure 1.3(B-D), with the circle region marking the superior sagittal sinus. This error can easily be corrected with phase unwrapping algorithms, assuming that it only wraps once. Another potential mistake is significant deviation of the imaging plane, where the imaging plane is no longer perpendicular to the flow of interest. Other sources of error include inadequate temporal or spatial resolution, and phase offset errors (Eddy currents). These have been detailed previously [38]. In our studies, this imaging technique has been optimized to minimize these errors. An overview of the velocity conversion from phase images is illustrated in Figure 1.3.

Bibliography

[1] Laurent Sakka, Guillaume Coll, and Jean Chazal. Anatomy and physiology of cerebrospinal fluid. *European annals of otorhinolaryngology, head and neck diseases*, 128(6):309–316, 2011.

[2] Dean A Seehusen, Mark Reeves, and Demitri Fomin. Cerebrospinal fluid analysis. *American family physician*, 68(6):1103–1108, 2003.

[3] Erik NTP Bakker, Brian J Bacskai, Michal Arbel-Ornath, Roxana Aldea, Beatrice Bedussi, Alan WJ Morris, Roy O Weller, and Roxana O Carare. Lymphatic clearance of the brain: perivascular, paravascular and significance for neurodegenerative diseases. *Cellular and molecular neurobiology*, 36(2):181–194, 2016.

[4] N Joan Abbott, Michelle E Pizzo, Jane E Preston, Damir Janigro, and Robert G Thorne. The role of brain barriers in fluid movement in the cns: is there a 'glymphatic'system? *Acta neuropathologica*, 135(3):387–407, 2018.

[5] Thomas Brinker, Edward Stopa, John Morrison, and Petra Klinge. A new look at cerebrospinal fluid circulation. *Fluids and Barriers of the CNS*, 11(1):1–16, 2014.

[6] David A Feinberg and Alexander S Mark. Human brain motion and cerebrospinal fluid circulation demonstrated with mr velocity imaging. *Radiology*, 163(3):793–799, 1987.

[7] DR Enzmann and NfsJ Pelc. Normal flow patterns of intracranial and spinal cerebrospinal fluid defined with phase-contrast cine mr imaging. *Radiology*, 178(2):467–474, 1991.

[8] MC Henry-Feugeas, I Idy-Peretti, B Blanchet, D Hassine, G Zannoli, and E Schouman-Claeys. Temporal and spatial assessment of normal cerebrospinal fluid dynamics with mr imaging. *Magnetic resonance imaging*, 11(8):1107–1118, 1993.

[9] D Greitz, A Franck, and B Nordell. On the pulsatile nature of intracranial and spinal csf-circulation demonstrated by mr imaging. *Acta radiologica*, 34(4):321–328, 1993.

[10] Jeong Hyun Lee, Ho Kyu Lee, Jae Kyun Kim, Hyun Jeong Kim, Ji Kang Park, and Choong Gon Choi. Csf flow quantification of the cerebral aqueduct in normal volunteers using phase contrast cine mr imaging. *Korean journal of radiology*, 5(2): 81–86, 2004.

[11] Francis Loth, M Atif Yardimci, and Noam Alperin. Hydrodynamic modeling of cerebrospinal fluid motion within the spinal cavity. *J. Biomech. Eng.*, 123(1):71–79,

2001.

[12] V Haughton and K-A Mardal. Spinal fluid biomechanics and imaging: an update for neuroradiologists. *American Journal of Neuroradiology*, 35(10):1864–1869, 2014.

[13] Yi-Hsuan Kao, Wan-Yuo Guo, Adrain Jy-Kang Liou, Yi-Hui Hsiao, and Chih-Che Chou. The respiratory modulation of intracranial cerebrospinal fluid pulsation observed on dynamic echo planar images. *Magnetic resonance imaging*, 26(2):198–205, 2008.

[14] Steffi Dreha-Kulaczewski, Mareen Konopka, Arun A Joseph, Jost Kollmeier, Klaus-Dietmar Merboldt, Hans-Christoph Ludwig, Jutta Gärtner, and Jens Frahm. Respiration and the watershed of spinal csf flow in humans. *Scientific reports*, 8(1):1–7, 2018.

[15] Giovanni Di Chiro. Observations on the circulation of the cerebrospinal fluid. *Acta Radiologica. Diagnosis*, 5(P2):988–1002, 1966.

[16] Giovani Di Chiro, Mary K Hammock, and W Archie Bleyer. Spinal descent of cerebrospinal fluid in man. *Neurology*, 26(1):1–1, 1976.

[17] Torgny VB Greitz, Arne OL Grepe, Magnus SF Kalmér, and Jacinto Lopez. Pre-and postoperative evaluation of cerebral blood flow in low-pressure hydrocephalus. *Journal of neurosurgery*, 31(6):644–651, 1969.

[18] AL Sanchez, C Martinez-Bazan, C Gutierrez-Montes, E Criado-Hidalgo, G Pawlak, W Bradley, V Haughton, and JC Lasheras. On the bulk motion of the cerebrospinal fluid in the spinal canal. *Journal of Fluid Mechanics*, 841:203–227, 2018.

[19] W Coenen, C Gutiérrez-Montes, S Sincomb, E Criado-Hidalgo, K Wei, K King, V Haughton, C Martínez-Bazán, AL Sánchez, and JC Lasheras. Subject-specific studies of csf bulk flow patterns in the spinal canal: implications for the dispersion of solute particles in intrathecal drug delivery. *American Journal of Neuroradiology*, 40 (7):1242–1249, 2019.

[20] William G Bradley Jr, David Scalzo, John Queralt, Wolfgang N Nitz, Dennis J Atkinson, and Priscilla Wong. Normal-pressure hydrocephalus: evaluation with cerebrospinal fluid flow measurements at mr imaging. *Radiology*, 198(2):523–529, 1996.

[21] D-S Kim, Joong-Uhn Choi, Ryoong Huh, Pyeung-Ho Yun, and Dong-Ik Kim. Quantitative assessment of cerebrospinal fluid hydrodynamics using a phase-contrast cine mr image in hydrocephalus. *Child's nervous system*, 15(9):461–467, 1999.

[22] Patrick H Luetmer, John Huston, Jonathan A Friedman, Geoffrey R Dixon, Ronald C

Petersen, Clifford R Jack, Robyn L McClelland, and Michael J Ebersold. Measurement of cerebrospinal fluid flow at the cerebral aqueduct by use of phase-contrast magnetic resonance imaging: technique validation and utility in diagnosing idiopathic normal pressure hydrocephalus. *Neurosurgery*, 50(3):534–543, 2002.

[23] A Scollato, R Tenenbaum, G Bahl, M Celerini, B Salani, and N Di Lorenzo. Changes in aqueductal csf stroke volume and progression of symptoms in patients with unshunted idiopathic normal pressure hydrocephalus. *American journal of neuroradiology*, 29(1): 192–197, 2008.

[24] Geir Ringstad, KE Emblem, O Geier, N Alperin, and PK Eide. Aqueductal stroke volume: comparisons with intracranial pressure scores in idiopathic normal pressure hydrocephalus. *American Journal of Neuroradiology*, 36(9):1623–1630, 2015.

[25] Sara Qvarlander, Khalid Ambarki, Anders Wåhlin, Johan Jacobsson, Richard Birgander, Jan Malm, and Anders Eklund. Cerebrospinal fluid and blood flow patterns in idiopathic normal pressure hydrocephalus. *Acta neurologica Scandinavica*, 135(5): 576–584, 2017.

[26] Geir Ringstad, Kyrre Eeg Emblem, and Per Kristian Eide. Phase-contrast magnetic resonance imaging reveals net retrograde aqueductal flow in idiopathic normal pressure hydrocephalus. *Journal of neurosurgery*, 124(6):1850–1857, 2016.

[27] V. Kurtcuoglu, M. Soellinger, P. Summers, K. Boomsma, D. Poulikakos, P. Boesiger, and Y. Ventikos. Computational investigation of subject-specific cerebrospinal fluid flow in the third ventricle and aqueduct of sylvius. *J. Biomech.*, 40(6):1235–1245, 2007.

[28] S. Gupta, M. Soellinger, P. Boesiger, D. Poulikakos, and V. Kurtcuoglu. Three-dimensional computational modeling of subject-specific cerebrospinal fluid flow in the subarachnoid space. *J. Biomech. Eng.*, 131(2):021010, 2009.

[29] B. Sweetman, M. Xenos, L. Zitella, and A. A. Linninger. Three-dimensional computational prediction of cerebrospinal fluid flow in the human brain. *Med. Biol. Eng. Comput.*, 41(2):67–75, 2011.

[30] Khalid Ambarki, Olivier Baledent, Guy Kongolo, Robert Bouzerar, Sidy Fall, and Marc-Etienne Meyer. A new lumped-parameter model of cerebrospinal hydrodynamics during the cardiac cycle in healthy volunteers. *IEEE transactions on biomedical engineering*, 54(3):483–491, 2007.

[31] Andreas A Linninger, Michalis Xenos, Brian Sweetman, Sukruti Ponkshe, Xiaodong Guo, and Richard Penn. A mathematical model of blood, cerebrospinal fluid and brain dynamics. *Journal of mathematical biology*, 59(6):729–759, 2009.

[32] Bryn A Martin, Philippe Reymond, Jan Novy, Olivier Balédent, and Nikolaos Stergiopulos. A coupled hydrodynamic model of the cardiovascular and cerebrospinal fluid system. *American Journal of Physiology-Heart and Circulatory Physiology*, 302 (7):H1492–H1509, 2012.

[33] Nafiseh Masoumi, F Framanzad, Behnam Zamanian, AS Seddighi, MH Moosavi, S Najarian, and Dariush Bastani. 2d computational fluid dynamic modeling of human ventricle system based on fluid-solid interaction and pulsatile flow. *Basic and clinical neuroscience*, 4(1):64, 2013.

[34] Andreas A Linninger, Kevin Tangen, Chih-Yang Hsu, and David Frim. Cerebrospinal fluid mechanics and its coupling to cerebrovascular dynamics. *Annual Review of Fluid Mechanics*, 48:219–257, 2016.

[35] S Sincomb, W Coenen, AL Sánchez, and JC Lasheras. A model for the oscillatory flow in the cerebral aqueduct. *Journal of Fluid Mechanics*, 899, 2020.

[36] SJ Sincomb, Wilfried Coenen, E Criado-Hidalgo, K Wei, K King, M Borzage, V Haughton, AL Sánchez, and Juan Carlos Lasheras. Transmantle pressure computed from mr imaging measurements of aqueduct flow and dimensions. *American Journal of Neuroradiology*, 42(10):1815–1821, 2021.

[37] S Sincomb, W Coenen, C Gutiérrez-Montes, C Martínez Bazán, V Haughton, and AL Sánchez. A one-dimensional model for the pulsating flow of cerebrospinal fluid in the spinal canal. *Journal of Fluid Mechanics*, 939, 2022.

[38] Joachim Lotz, Christian Meier, Andreas Leppert, and Michael Galanski. Cardiovascular flow measurement with phase-contrast mr imaging: basic facts and implementation. *Radiographics*, 22(3):651–671, 2002.

[39] WR Nitz, WG Bradley Jr, AS Watanabe, RR Lee, B Burgoyne, RM O'sullivan, and MD Herbst. Flow dynamics of cerebrospinal fluid: assessment with phase-contrast velocity mr imaging performed with retrospective cardiac gating. *Radiology*, 183(2): 395–405, 1992.

Chapter 2

A model for the oscillatory flow in the cerebral aqueduct

2.1 Introduction

Cerebrospinal fluid flows between ventricles through their different interconnecting passages (or foramina), including the foramina of Monro, connecting the lateral ventricles with the third ventricle, the cerebral aqueduct (or aqueduct of Sylvius) connecting the third and fourth ventricles, and the foramen of Magendie and foramina of Luschka, connecting the fourth ventricle with the SAS shown in Figure 2.1. The resulting motion includes a steady component corresponding to the continuous flow from the ventricles, where CSF is secreted from the blood plasma in the choroid plexus, towards the subarachnoid space (SAS), where CSF is reabsorbed into the venous circulation at finger-like projections of the arachnoid membrane surrounding the brain, called villi. Besides this slow steady motion, the CSF is known to undergo a much faster pulsating motion driven by the cardiac and respiratory cycles, with peak volumetric flow rates $Q(t) \sim 0.1$ cm^3/s that are much larger than the steady flow rate ~ 0.005 cm^3/s corresponding to the continuous evacuation of the CSF produced in the ventricles [1]. The associated dynamics, involving complex nonlinear interactions between the fluid motion and the displacement of the soft tissues of the CNS, plays a fundamental role in the physiological function of CSF as a vehicle for metabolic-waste clearance as well as in the development of CNS diseases, such as idiopathic normal

pressure hydrocephalus (iNPH) [1]. In-vivo measurements using non-invasive experimental methods based on magnetic resonance imaging (MRI) [2] and advanced modelling studies employing computational-fluid-dynamics (CFD) techniques [3–5] have been instrumental in increasing our understanding of the underlying fluid-structure interaction problem. Despite recent progress, many fundamental questions remain open, as summarized in a recent review [1].

Attention is focused here on the pulsating flow in the cerebral aqueduct, driven by the interventricular pressure difference $\Delta p(t) \simeq p_3 - p_4$, where $p_3(t)$ and $p_4(t)$ are the time-dependent, nearly uniform [3] values of the pressure in the third and fourth ventricles. Approximate descriptions assuming fully developed unidirectional Womersley-like flow [6] or a simplified hydraulic model [7] are available, as well as computational studies of the associated flow including realistic anatomical shapes [3, 8–10]. In this chapter we report on the development of a simplified model accounting for the relevant controlling parameters, to be used in predicting the relation between the interventricular pressure difference $\Delta p(t) = p_3 - p_4$ and the resulting volume flow rate in the aqueduct $Q(t)$. Accurate knowledge of this relation is needed to quantify $\Delta p(t)$ from MRI measurements of CSF flow rate $Q(t)$ [6]. Since the cerebral aqueduct is the narrowest interventricular passage, most of the pressure drop associated with the CSF motion in the ventricular system occurs as the CSF flows between the third and fourth ventricles [5, 6]. As a result, the value of $\Delta p(t) \simeq p_3 - p_4$ provides an approximate representation for the so-called transmantle pressure [8, 9], the pressure difference between the lateral ventricles and the upper convexity of the SAS. Direct measurements of this quantity require very accurate simultaneous readings from two separate high-resolution pressure sensors [11], an invasive procedure with considerable risk factors [12], thereby fostering interest in indirect non-invasive techniques based on MRI measurements of $Q(t)$.

The interventricular pressure difference $\Delta p(t) = p_3 - p_4$ and the resulting volume flow rate in the aqueduct $Q(t)$ exhibit distinct quasi-periodic components associated with

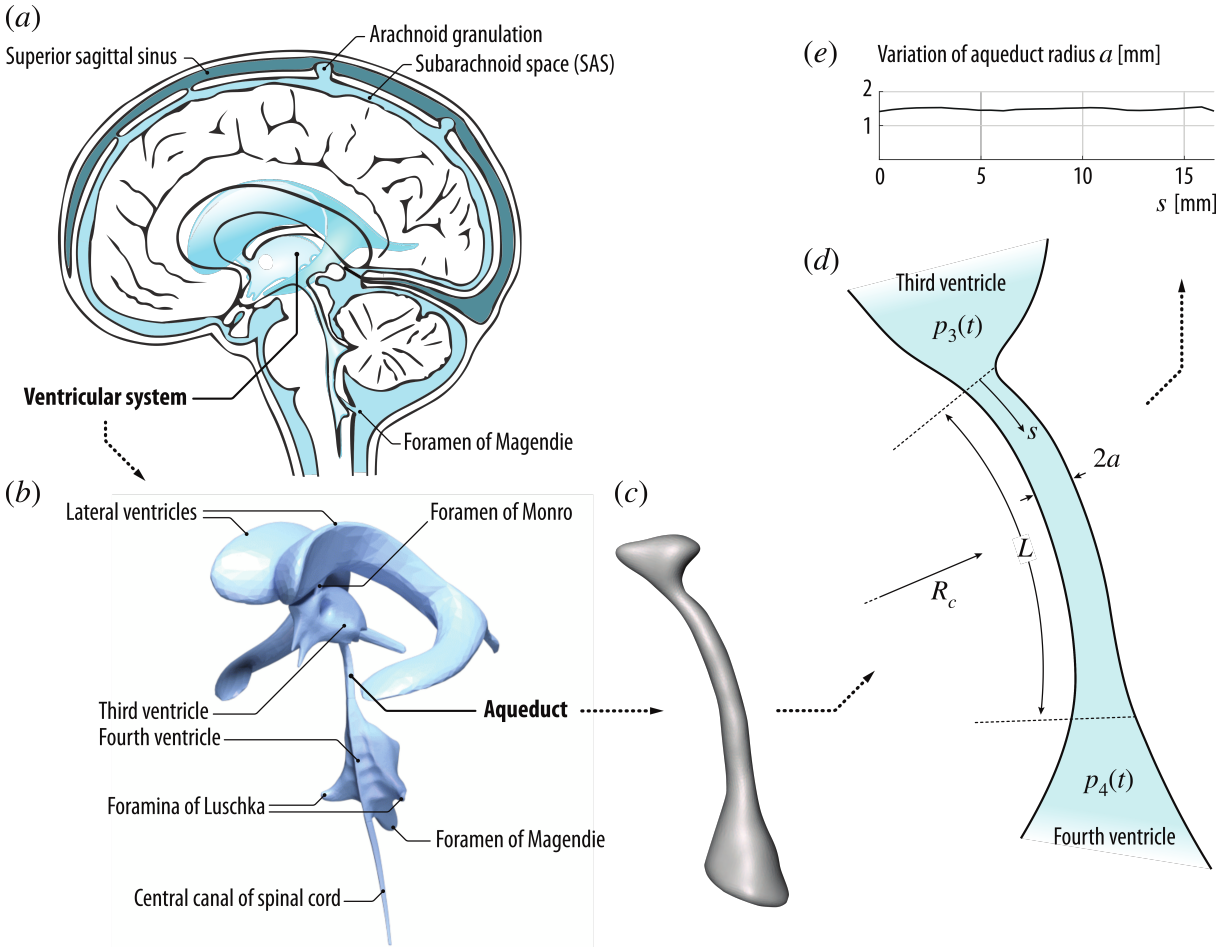

Figure 2.1. (a) Schematic views of the cranial cavity and (b) the cerebral ventricular system (BodyParts3D, © The Database Center for Life Science licensed under CC Attribution-Share Alike 2.1 Japan). Anatomic MR images are used to obtain (c) a smoothed surface mesh of the cerebral aqueduct of a healthy subject, which was used for (d) the simplified illustration highlighting the different flow regions and (e) the variation of the aqueduct radius with the distance to the third ventricle.

the cardiac and respiratory pulsations, with corresponding periods $T \sim 1\,\mathrm{s}$ and $T \sim 4-5\,\mathrm{s}$, respectively. Except for one study [13], all available MRI flow measurements [14–16] indicate that the cardiac component of the flow velocity is somewhat larger than the respiratory component, that being also the case for the flow elsewhere in the cranial cavity [17] and along the spinal canal [18], the latter flow displaying increasing effects of respiration on approaching the lumbar region. Since the pressure difference required to accelerate the flow in the aqueduct can be anticipated to be inversely proportional to the oscillation period, as follows from a balance between the local flow acceleration and the pressure force per unit mass, the interventricular pressure difference $\Delta p(t)$ associated with the cardiac cycle is much larger than that of the respiratory cycle, a conclusion supported by direct pressure measurements [11]. By way of contrast, the stroke length L_s (or stroke volume) of the oscillatory flow, linearly proportional to the oscillation period, is significantly larger for the respiratory-driven flow [11], as shown by MRI measurements [16, 19]. As a result, studies focusing on the determination of the stroke volume, an important parameter characterizing aqueductal flow in iNPH patients and their response to shunting [20, 21], must account for the effects of respiration. The present analysis is general, in that the parametric ranges investigated include conditions corresponding to both cardiac and respiratory driven motion.

2.2 Scales and order-of-magnitude estimates

The cerebral aqueduct, shown in Figure 2.1, is a slightly curved slender canal of length $L \sim 10-15$ mm and radius of curvature $R_c \sim 40-60$ mm. Its detailed anatomic shape is displayed in the outer contour given in Figure 2.1(c), measured in a healthy subject with MRI imaging techniques. The aqueduct's nearly cylindrical shape [10] can be described by assuming a circular section with slowly varying radius $a(s) \ll L$, with s representing the distance along the centerline of the aqueduct measured from the third

ventricle. The variation corresponding to the aqueduct of Figure 2.1(c), obtained after smoothing the segmented contour, is shown in 2.1(e). The corresponding aqueduct volume $\int_0^L \pi a^2 \mathrm{d}s$ can be equated to that of a circular cylinder with the same length L to define the characteristic aqueduct radius a_c from $\pi a_c^2 L = \int_0^L \pi a^2 \mathrm{d}s$, yielding typical values of order $a_c \sim 1 - 1.5\,\mathrm{mm} \ll L$.

We address the pulsating motion induced by the periodic pressure difference $\Delta p(t) \simeq p_3 - p_4$, resulting in a periodic volumetric flow rate $Q(t)$ with the same period T. The corresponding stroke volume $V_s = \frac{1}{2}\int_0^T |Q| \mathrm{d}t$ has been measured to be comparable to the aqueduct volume $\pi a_c^2 L$ [20–22]. Correspondingly, the characteristic stroke length $L_s = V_s/(\pi a_c^2)$ is comparable to the aqueduct length L. Since the temporal variations of the aqueduct volume, associated with the deformation of the bounding tissue, are much smaller than the aqueduct volume itself [3], the aqueduct can be assumed to be rigid for the analysis of the flow, as done below in our analysis. In this respect, the problem is fundamentally different from that of CSF flow in the spinal canal [1], where there exists close coupling between the fluid motion and the displacement of the canal walls, leading to a complex fluid-structure interaction problem that has been recently described with a linear elastic model adopted for the canal deformation [23, 24]. For the flow in the aqueduct, the errors associated with the use of the rigid-wall approximation can be anticipated to be on the order of the ratio of the cyclic variation of the aqueduct volume to the stroke volume, a quantity of the order of 10^{-2}, as revealed by MRI brain-motion scans [3].

The above estimates can be used to anticipate the character of the flow in the aqueduct, as done below. It is important to remark here that the analysis must consider the existence of three distinct regions, namely, the long central part of the aqueduct, where the flow is slender, and the two (much shorter) non-slender opening regions connecting the ends of the aqueduct with the ventricles.

Inside the aqueduct the flow is slender, with characteristic streamwise and transverse lengths L and $a_c \ll L$. Since the streamlines are always nearly aligned inside the

aqueduct, the transverse pressure variations are of order $(a_c/L)^2\Delta p \ll \Delta p$ and thus can be neglected in the first approximation. The characteristic streamwise velocity is given by $U_c = \omega L_s \sim L_s/T$ in terms of the angular frequency $\omega = 2\pi/T$, yielding $U_c^2/L = \omega^2 L_s^2/L$ and $\omega U_c = \omega^2 L_s$ for the orders of magnitude of the convective and local accelerations, respectively, their relative importance being therefore measured by the parameter $L_s/L \sim 1$, the inverse of the relevant Strouhal number. The viscous time across the aqueduct $a_c^2/\nu \sim 1\,\mathrm{s}$ is comparable in magnitude to the flow oscillation period T, thereby yielding order-unity values of the Womersley number $\alpha = (\omega a_c^2/\nu)^{1/2}$; the associated Stokes number α^2 representing the ratio of the magnitudes of the local acceleration to the viscous force (per unit mass). The order-of-magnitude analysis therefore reveals that inside the aqueduct all terms in the streamwise momentum equation have comparable magnitude. Since convective acceleration has a non-negligible effect, the relation between Δp and the flow rate $Q(t)$ is inherently nonlinear, thereby compromising the accuracy of studies adopting a presumed linear relation [7]. Also, analyses neglecting convective terms by assuming developed (i.e. Womersley-like) flow either everywhere [6] or at the aqueduct entrance [3, 11], a valid approximation when $L_s/L \ll 1$, are necessarily inaccurate when $L_s \sim L$, the prevailing condition found in healthy and iNPH subjects [20–22].

In the opening regions, of characteristic size a_c, the flow is non-slender, with characteristic velocity $U_c = \omega L_s$, corresponding to a Strouhal number $a_c/L_s \sim a_c/L \ll 1$ and a Reynolds number $U_c a_c/\nu \sim \alpha^2/(a_c/L) \gg 1$. Since local acceleration and viscous forces have small effects scaling with $a_c/L \ll 1$, the flow in the opening regions is quasi-steady and inviscid in the first approximation. As seen in previous CFD simulations of the flow in the third ventricle [3], the resulting streamline pattern is very different for outflow, when the stream separates to form a jet that discharges into the ventricle, and for inflow, where the CSF accelerates from rest approaching the aqueduct entrance from all directions, with the sum of the pressure and the kinetic energy remaining constant along

any given streamline. Since $L_s \sim L$, the associated pressure drop in the opening region, of order $\rho U_c^2 = \rho\omega^2 L_s^2$, is comparable in magnitude to the pressure drop along the aqueduct, of order $\rho U_c \omega L = \rho\omega^2 L_s L$, so that both contributions must be accounted for in evaluating the interventricular pressure $\Delta p(t) = p_3 - p_4$ for a given volumetric flow rate $Q(t)$.

2.3 Simplified description of the flow

The aqueduct is seen as a slender canal connecting two large reservoirs whose pressure varies periodically in time. The problem will be posed as that of determining the interventricular pressure difference $\Delta p(t)$ that results in a given volume flow rate $Q(t)$, with the latter having a zero mean value, i.e. $\int_0^T Q\mathrm{d}t = 0$. The slender-flow approximation $a_c/L \ll 1$ will be employed in simplifying the solution, with the dimensionless problem reducing to that of finding the pressure difference $\Pi = \Delta p/(\rho\omega U_c L)$ associated with a dimensionless flow rate $\bar{Q} = Q/(\omega V_s)$ for a given aqueduct anatomy, defined by the distribution of aqueduct radius $\bar{a} = a/a_c$, and given values of the controlling parameters $L_s/L \sim 1$ and $\alpha^2 = \omega a_c^2/\nu \sim 1$.

The function $\bar{Q}$ must satisfy $\int_0^{2\pi} |\bar{Q}|\mathrm{d}\tau = 2$, as follows from the definition of the stroke volume $V_s = \frac{1}{2}\int_0^T |Q|\mathrm{d}t$, with $\tau = \omega t$ representing a dimensionless time. For the cardiac-induced motion, the typical temporal variation $\bar{Q}(\tau)$ over a cycle is represented by the solid curve on the upper plot of figure 2.2, to be discussed later, corresponding to cardiac-gated MRI measurements of the aqueduct flow rate in a healthy subject. A Fourier analysis of the signal reveals that the first-mode, of period $2\pi/\omega$, is dominant [6], so that for many quantitative purposes a simple sinusoidal function $\bar{Q}(\tau) = \frac{1}{2}\sin\tau$ can be used to represent the flow.

The computation of $\Pi(\tau)$ for a given $\bar{Q}(\tau)$ requires consideration of the flow both inside the aqueduct and in the opening regions connecting the aqueduct to the ventricles. The slender flow in the aqueduct is described in terms of the dimensionless streamwise

distance from the third ventricle $x = s/L$ and the dimensionless radius r, the latter obtained by scaling the radial distance with the characteristic aqueduct radius a_c. Neglecting small terms of order $(a_c/L)^2$ and a_c/R_c in writing the conservation equations inside the aqueduct leads to the axisymmetric boundary-layer problem

$$\frac{\partial u}{\partial x} + \frac{1}{r}\frac{\partial}{\partial r}(rv) = 0, \tag{2.1}$$

$$\frac{\partial u}{\partial \tau} + \frac{L_s}{L}\left(u\frac{\partial u}{\partial x} + v\frac{\partial u}{\partial r}\right) = -\frac{\partial p'}{\partial x} + \frac{1}{\alpha^2}\frac{1}{r}\frac{\partial}{\partial r}\left(r\frac{\partial u}{\partial r}\right), \tag{2.2}$$

where the dimensionless streamwise and radial velocity components u and v are scaled with $U_c = \omega L_s$ and $U_c a_c/L$, respectively. The axial velocity must satisfy $\bar{Q}(\tau) = \int_0^{\bar{a}} 2ru\mathrm{d}r$, as follows from the selected scaling. The streamwise pressure gradient $P_x(x,\tau) = \partial p'/\partial x$, where p' denotes the spatial pressure difference scaled with $\rho\omega U_c L$, is unknown and must be determined as part of the integration.

Equations (2.1) and (2.2) must be integrated for $0 \le x \le 1$ and $0 \le r \le \bar{a}(x)$ subject to the boundary conditions

$$\frac{\partial u}{\partial r} = v = 0 \quad \text{at} \quad r = 0 \qquad \text{and} \qquad u = v = 0 \quad \text{at} \quad r = \bar{a}(x). \tag{2.3}$$

To write the needed boundary conditions for u at the two ends of the canal $x = 0, 1$ consideration must be given to the CSF motion in the near-field region, corresponding to distances from the canal opening of order $a_c \ll L$, where the flow is non-slender, with characteristic velocities of order U_c. Using a_c and U_c as characteristic scales of length and velocity, reduces the momentum equation to

$$\left(\frac{a_c}{L}\right)\frac{\partial \mathbf{v}}{\partial \tau} + \frac{L_s}{L}\mathbf{v}\cdot\nabla\mathbf{v} = -\nabla p' + \frac{1}{\alpha^2}\left(\frac{a_c}{L}\right)\nabla^2\mathbf{v}. \tag{2.4}$$

This dimensionless equation reveals that, in the limit $a_c/L \ll 1$ considered here, with

$\alpha \sim 1$ and $L_s/L \sim 1$, the flow in the opening regions is quasi-steady and nearly inviscid in the first approximation. The resulting streamline pattern, shown in Fig. 5 of [3], is drastically different for inflow (i.e. $\bar{Q} > 0$ at $x = 0$ or $\bar{Q} < 0$ at $x = 1$) and outflow (i.e. $\bar{Q} < 0$ at $x = 0$ or $\bar{Q} > 0$ at $x = 1$). For outflow, the stream separates to form a jet that discharges into the ventricle, with the pressure across the jet being approximately equal to that of the ventricle. In the boundary-layer approximation employed here in describing the flow inside the aqueduct, no boundary condition is needed for the flow velocity at the canal end when outflow is present.

For inflow, on the other hand, the CSF accelerates from rest approaching the aqueduct entrance from all directions. As follows from the steady inviscid form of (2.4), the stagnation pressure in the opening region, outside from a thin near-wall viscous boundary layer, is equal to the pressure in the feeding reservoir. Since the streamlines align on entering the aqueduct, the pressure is uniform across the entire entrance section, so that the condition $p' + (L_s/L)|\mathbf{v}|^2/2 =$ constant implies that the velocity must also be uniform there, thereby leading to the alternating boundary conditions

$$\begin{cases} \bar{Q} > 0: \quad u = \bar{Q}(\tau)/\bar{a}^2(0) \quad \text{at } x = 0 \\ \bar{Q} < 0: \quad u = \bar{Q}(\tau)/\bar{a}^2(1) \quad \text{at } x = 1 \end{cases}, \tag{2.5}$$

involving the dimensionless local radii $\bar{a}(0) = a(0)/a_c$ and $\bar{a}(1) = a(L)/a_c$ at the two aqueduct's ends. Correspondingly, the pressure drop between the ventricle and the entrance of the aqueduct is $(L_s/L)[\bar{Q}/\bar{a}(0)]^2/2$ if $\bar{Q} > 0$ and $(L_s/L)[\bar{Q}/\bar{a}(1)]^2/2$ if $\bar{Q} < 0$, as follows from conservation of stagnation pressure.

As revealed by (2.4), the assumption of quasi-steady flow in the entrance region, valid over most of the cycle, can be expected to fail when $\bar{Q}$ vanishes, during short flow-reversal stages of relative duration $\Delta\tau \simeq a_c/L_s$ when the velocity is of order a_c/L_s. As a result, the local acceleration becomes comparable to the convective acceleration

in the entrance region, while viscous forces are still negligible there. During this short stage the flow is inviscid also inside the aqueduct, where the momentum balance (2.2) reduces to $\partial u/\partial\tau = -\partial p'/\partial x$, which can be integrated across the section to show that $-\partial p'/\partial x = \mathrm{d}\bar{Q}/\mathrm{d}\tau|_0$, involving the rate of variation of the flow rate at the instant of flow reversal $\mathrm{d}\bar{Q}/\mathrm{d}\tau|_0$. Integrating this last equation shows that, during this short stage, the pressure drop along the aqueduct is given by $\mathrm{d}\bar{Q}/\mathrm{d}\tau|_0 \sim 1$, while the corresponding pressure drop across the entrance region is small, of order a_c/L_s.

For given values of L_s/L and α, a given aqueduct shape $\bar{a}(x)$, and a given 2π-periodic dimensionless flow rate $\bar{Q}(\tau)$, integration of (2.1) and (2.2) subject to the boundary conditions stated in (2.3) and (2.5) determines the velocity field $u(x, r, \tau)$ and $v(x, r, \tau)$ and associated pressure gradient $P_x(x, \tau)$. As previously explained, the interventricular pressure difference $p_3 - p_4$ is the sum of the pressure loss along the slender portion of the aqueduct and the pressure loss at the aqueduct entrance, the latter evaluated earlier, below (2.5), with use of Bernoulli's law. In our dimensionless formulation, the result can be expressed in the form

$$\Pi(\tau) = \frac{p_3 - p_4}{\rho\omega^2 L_s L} = -\int_0^1 P_x \mathrm{d}x \begin{cases} +\frac{1}{2}\frac{L_s}{L}\frac{\bar{Q}^2}{\bar{a}^4(0)} & \text{if} \quad \bar{Q} > 0 \\ -\frac{1}{2}\frac{L_s}{L}\frac{\bar{Q}^2}{\bar{a}^4(1)} & \text{if} \quad \bar{Q} < 0 \end{cases} . \tag{2.6}$$

This result is to be compared with the pressure drop

$$\Pi(\tau) = \frac{8\bar{Q}}{\alpha^2}\int_0^1 \frac{\mathrm{d}x}{\bar{a}^4(x)} \tag{2.7}$$

corresponding to the quasi-steady Poiseuille velocity profile $u = -\frac{1}{4}\alpha^2 P_x(\bar{a}^2 - r^2)$, obtained in the present formulation when taking the limit $\alpha \ll 1$. Additional closed-form analytical

solutions can be found in the inviscid limit $\alpha \gg 1$, when (2.6) can be seen to reduce to

$$\Pi(\tau) = \left(\int_0^1 \frac{\mathrm{d}x}{\bar{a}^2(x)} \right) \frac{\mathrm{d}\bar{Q}}{\mathrm{d}\tau} \begin{cases} +\frac{1}{2}\frac{L_s}{L}\frac{\bar{Q}^2}{\bar{a}^4(1)} & \text{if} \quad \bar{Q} > 0 \\ -\frac{1}{2}\frac{L_s}{L}\frac{\bar{Q}^2}{\bar{a}^4(0)} & \text{if} \quad \bar{Q} < 0 \end{cases}, \tag{2.8}$$

and also for $L_s/L \ll 1$, when convective terms have a small effect on the aqueduct flow, as can be inferred from (2.2), resulting in a linear Womersley-like problem that can be solved explicitly using a complex Fourier series representation for the flow rate

$$\bar{Q}(\tau) = \mathrm{Re}\left(\sum_{n=1}^{\infty} Q_n \mathrm{e}^{\mathrm{i}n\tau} \right) \tag{2.9}$$

to give $P_x = \mathrm{Re}\left(\sum_{n=1}^{\infty} A_n \mathrm{e}^{\mathrm{i}n\tau}\right)$, where

$$A_n(x) = -\frac{\mathrm{i}\, nQ_n}{\bar{a}^2(x)} \left(1 + \frac{J_1(\beta_n)}{(\beta_n/2)J_0(\beta_n) - J_1(\beta_n)} \right) \quad \text{and} \quad \beta_n(x) = \frac{\mathrm{i}-1}{\sqrt{2}} \sqrt{n}\alpha \bar{a}(x) \tag{2.10}$$

are complex functions that vary along the aqueduct, with Re() denoting the real part of a complex expression and J_0 and J_1 representing the Bessel functions of order 0 and 1, respectively. Since the pressure drop at the aqueduct entrance becomes negligibly small for $L_s/L \ll 1$, the dimensionless interventricular pressure difference (2.6) reduces in this case to

$$\Pi(\tau) = \mathrm{Re}\left[\mathrm{i} \sum_{n=1}^{\infty} nQ_n \mathrm{e}^{\mathrm{i}n\tau} \int_0^1 \frac{1}{\bar{a}^2} \left(1 + \frac{J_1(\beta_n)}{(\beta_n/2)J_0(\beta_n) - J_1(\beta_n)} \right) \mathrm{d}x \right]. \tag{2.11}$$

2.4 Selected numerical results

The governing equations were discretized using a Krause zig-zag finite-difference scheme in x and t [25] (uniform $\Delta x = 1/200$; adaptive time step with mean $\Delta\tau = 2\pi/800$), combined with Chebyshev spectral collocation in r (32 points). At each step in time, the

equations are marched from $x = 0$ to 1 when $Q > 0$, and from $x = 1$ to 0 when $Q < 0$. The nonlinearity in the convective term is handled by an iterative fixed-point procedure at every marching step in x. The computation was run in time until a 2π-periodic solution was reached, with convergence occurring after about 5–10 cycles. Special attention was given to the transition between outflow and inflow, occurring once at each end of the aqueduct during the flow cycle. In the proposed scheme, the velocity profile at the canal end where outflow is present is computed as part of the boundary-layer computation, with the corresponding velocity at the other end given by (2.5). As previously discussed, this approximation can be expected to fail during the short stages of flow reversal, as the quasi-steady approximation breaks down in the opening region. This was apparent in the numerical integrations, which revealed that, when $\bar{Q}$ vanishes, the resulting outflow velocity, although very small (typical peak values not exceeding 10^{-1}), was not exactly zero, leading to a discontinuity in the temporal evolution at the canal end when switching between the boundary conditions in (2.5). This was accounted for in the numerical integration by incorporating a short transition stage, with duration $\Delta\tau \ll 1$ following the change of sign of $\bar{Q}$, during which the inflow velocity profile was continuously adapted with a linear temporal fit from that found at the end of the outflow period to the inflow uniform value defined in (2.5). The resulting value of $\Pi(\tau)$ was found to be independent of $\Delta\tau$ provided that $10^{-2} \ll \Delta\tau \ll 10^{-1}$.

The bottom plot in Figure 2.2 shows illustrative results corresponding to a canal of constant radius $\bar{a} = 1$. The shape $\bar{Q}$ of the specific flow rate employed in this computation, shown as a solid curve in the upper plot, as well as the values of $L_s/L = 0.93$, $\alpha = 3.23$ correspond to those obtained using cardiac-gated MRI measurements of the aqueduct flow in a healthy human subject [26]. The periodic function $\Pi(\tau)$ evaluated from (2.6) is shown as a solid curve. Because of the effect of the nonlinear convective terms, the average interventricular pressure, identically zero in the linear limit $L_s/L \ll 1$, takes a small non-zero value $\int_{\tau}^{\tau+2\pi} \Pi \mathrm{d}\tau/(2\pi) = 0.04$, in agreement with previous findings [27]. For

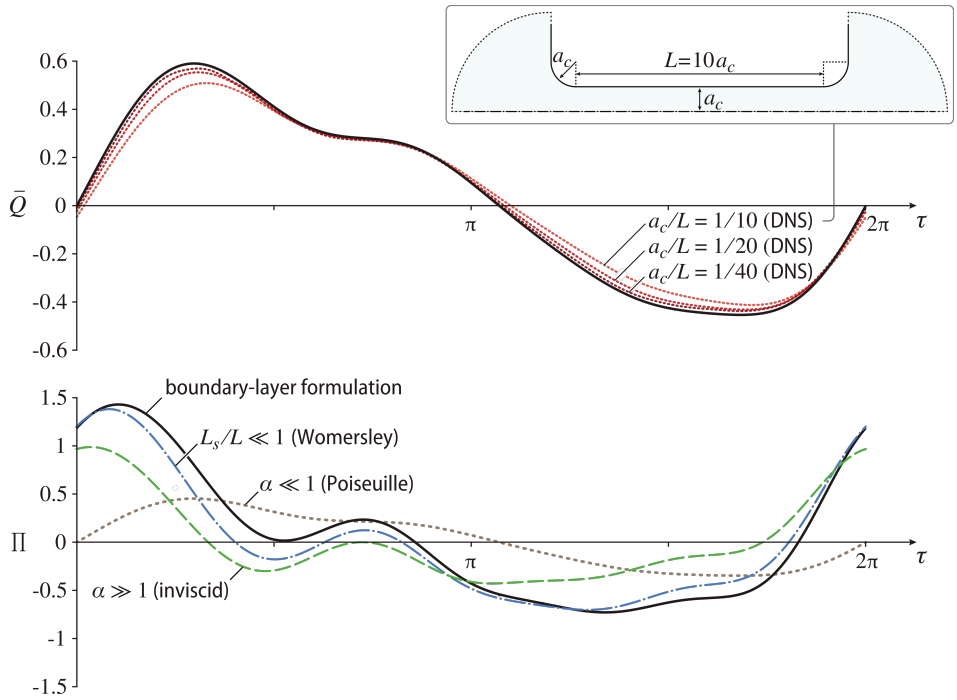

Figure 2.2. The solid curve in the lower plot represents the dimensionless pressure difference $\Pi(\tau)$ determined from the simplified model with $L_s/L = 0.93$, $\alpha = 3.23$, and $\bar{a} = 1$ for the dimensionless function $\bar{Q}(\tau)$ represented by the solid curve in the upper plot, corresponding to the Fourier decomposition of MRI measurements of the volumetric flow rate in the aqueduct of a healthy 36-year old male subject using phase contrast [26]. The additional dot-dashed, dashed, and dotted curves in the lower plot represent, respectively, the results of the Womersley approximation (2.11), of the inviscid approximation (2.8), and of the quasi-steady Poiseuille flow (2.7). The dotted curves in the upper plot are obtained from direct numerical simulations (DNS) using the interventricular pressure difference $\Pi(\tau)$ represented by the solid curve in the lower plot for different values of a_c/L.

completeness, the figure also includes the pressure predictions obtained with Poiseuille flow and also in the two limits $L_s/L \ll 1$ (Womersley) and $\alpha \gg 1$ (inviscid). As can be seen, for this specific case the former limit, neglecting nonlinear terms while retaining the local acceleration, provides a largely satisfactory description of the interventricular pressure, with quantitative departures remaining below 20% over most of the cycle. In contrast, the quasi-steady Poiseuille solution leads to severe underpredictions of interventricular pressure difference.

The dimensionless interventricular pressure shown in Figure 2.2 can be expressed

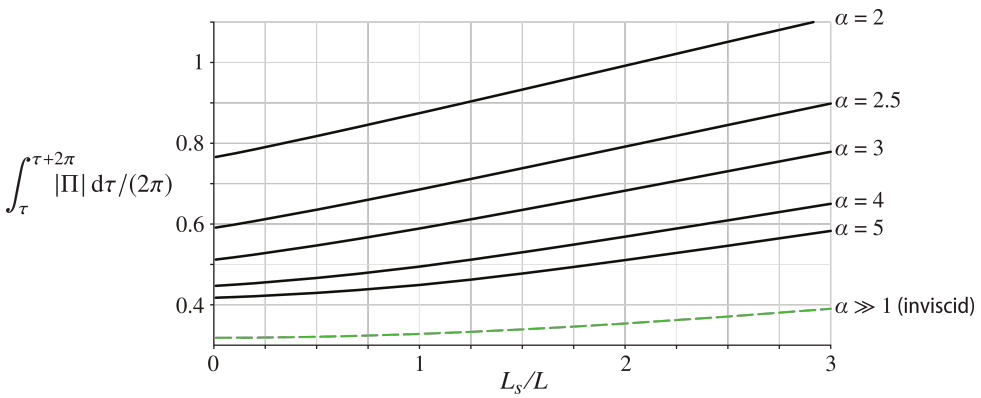

Figure 2.3. The variation of $\int_\tau^{\tau+2\pi} |\Pi| \mathrm{d}\tau/(2\pi)$ with L_s/L obtained from the simplified flow model for $\bar{a} = 1$, $\bar{Q}(\tau) = \frac{1}{2}\sin\tau$, and different values of α.

in dimensional form with use of $\Delta p = \rho\omega^2 L_s L \Pi$. Using in the evaluation $L = 10$ mm for the aqueduct length along with the standard cardiac frequency $\omega = 2\pi$ s^{-1} reveals that the dimensionless peak value $\Pi \simeq 1.5$ in Figure 2.2 corresponds to an overpressure $\Delta p = p_3 - p_4 \simeq 5.5$ Pa, consistent with existing measurements [11, 28] and computations [5] of instantaneous spatial pressure variations in the cranial cavity. As expected, the corresponding maximum overpressure predicted with Poiseuille velocity $p_3 - p_4 \simeq 1.66$ Pa, corresponding to the peak $\Pi = 0.452$ in Figure 2.2, is significantly smaller.

Direct numerical simulations were used to test the accuracy of the simplified model. The computations considered the geometry illustrated in the inset of Figure 2.2, corresponding to a duct of length L and constant radius a_c connecting two quasi-infinite reservoirs, with the smooth convex surface connecting the pipe with the reservoir having radius a_c. The axisymmetric Navier-Stokes equations were integrated for different values of a_c/L using as boundary condition the interventricular pressure difference $\Pi(\tau)$ shown as a solid curve in the lower plot of Figure 2.2. Resulting flow rates $\bar{Q}(\tau)$ are represented in the upper plot. As can be seen, the results rapidly converge to the original flow rate used in the simplified model, with relative differences scaling approximately with a_c/L.

The model was used to quantify the parametric dependence of $\int_\tau^{\tau+2\pi} |\Pi| \mathrm{d}\tau/(2\pi)$, a measure of the oscillating force exerted on the brain. Results corresponding to $\bar{a} = 1$

and $\bar{Q}(\tau) = \frac{1}{2}\sin\tau$ are plotted in Figure 2.3 as a function of L_s/L for different values of α, including the inviscid result $\int_{\tau}^{\tau+2\pi} |\Pi| \mathrm{d}\tau/(2\pi) = 1/\pi + (L_s/L)/16$ corresponding to the limit $\alpha \gg 1$. The figure covers the range of conditions typically found in healthy subjects, characterized by values of L_s/L of order unity and Womersley numbers ranging from $\alpha \simeq 2$ for the respiratory cycle to $\alpha \simeq 4$ for the cardiac cycle. The plot can also be used in connection with iNPH patients, who typically show enlarged aqueducts and higher tidal volumes [20–22], corresponding to larger values of the parameters α and L_s/L.

2.5 Concluding remarks

The simplified flow model presented above can be instrumental in developing protocols for non-invasive patient-specific quantification of the transmantle pressure difference between the lateral ventricles and the SAS from MRI measurements of the aqueduct radius $a(s)$ and volumetric flow rate $Q(t)$. These models have the potential for improving our current understanding of intracranial flow dynamics, associated with the development of CNS diseases, enabling the development of early-diagnosis techniques.

Acknowledgments

Chapter 2, in full with slight modifications, is a reprint of the material as it appears in the Journal of Fluid Mechanics, 2020. Sincomb, Stephanie.; Coenen, Wilfried; Sánchez, Antonio L. and Lasheras, Juan C. The dissertation author was the primary author of this paper.

Bibliography

[1] A. A. Linninger, K. Tangen, C.-Y. Hsu, and D. Frim. Cerebrospinal fluid mechanics and its coupling to cerebrovascular dynamics. *Annu. Rev. Fluid Mech.*, 48:219–257, 2016.

[2] D. A. Feinberg and A. S. Mark. Human brain motion and cerebrospinal fluid circulation demonstrated with mr velocity imaging. *Radiology*, 163(3):793–799, 1987.

[3] V. Kurtcuoglu, M. Soellinger, P. Summers, K. Boomsma, D. Poulikakos, P. Boesiger, and Y. Ventikos. Computational investigation of subject-specific cerebrospinal fluid flow in the third ventricle and aqueduct of sylvius. *J. Biomech.*, 40(6):1235–1245, 2007.

[4] S. Gupta, M. Soellinger, P. Boesiger, D. Poulikakos, and V. Kurtcuoglu. Three-dimensional computational modeling of subject-specific cerebrospinal fluid flow in the subarachnoid space. *J. Biomech. Eng.*, 131(2):021010, 2009.

[5] B. Sweetman, M. Xenos, L. Zitella, and A. A. Linninger. Three-dimensional computational prediction of cerebrospinal fluid flow in the human brain. *Med. Biol. Eng. Comput.*, 41(2):67–75, 2011.

[6] G. Bardan, F. Plouraboué, M. Zagzoule, and O. Baledent. Simple patient-based transmantle pressure and shear estimate from cine phase-contrast MRI in cerebral aqueduct. *IEEE Trans. Biomed. Eng.*, 59(10):2874–2883, 2012.

[7] P. Longatti, A. Fiorindi, P. Peruzzo, L. Basaldella, and F. M. Susin. Form follows function: estimation of CSF flow in the third ventricle–aqueduct–fourth ventricle complex modeled as a diffuser/nozzle pump. *J. Neurosurg.*, 1(aop):1–8, 2019.

[8] E. E. Jacobson, D. F. Fletcher, M. K. Morgan, and I. H. Johnston. Fluid dynamics of the cerebral aqueduct. *Pediatr. Neurosurg.*, 24(5):229–236, 1996.

[9] E. E. Jacobson, D. F. Fletcher, M. K. Morgan, and I. H. Johnston. Computer modelling of the cerebrospinal fluid flow dynamics of aqueduct stenosis. *Med. Biol. Eng. Comput.*, 37(1):59–63, 1999.

[10] L. Fin and R. Grebe. Three dimensional modeling of the cerebrospinal fluid dynamics and brain interactions in the aqueduct of sylvius. *Comput. Methods Biomech. Biomed. Engin.*, 6(3):163–170, 2003.

[11] V. Vinje, G. Ringstad, E. K. Lindstrøm, L. M. Valnes, M. E. Rognes, P. K. Eide, and K.-A. Mardal. Respiratory influence on cerebrospinal fluid flow–a computational study based on long-term intracranial pressure measurements. *Sci. Rep.*, 9(1):1–13, 2019.

[12] R. D. Penn, M. C. Lee, A. A. Linninger, K. Miesel, S. N. Lu, and L. Stylos. Pressure gradients in the brain in an experimental model of hydrocephalus. *J. Neurosurg.*, 102 (6):1069–1075, 2005.

[13] S. Dreha-Kulaczewski, A. A. Joseph, K.-D. Merboldt, H.-C. Ludwig, J. Gärtner, and J. Frahm. Inspiration is the major regulator of human CSF flow. *J. Neurosci.*, 35(6): 2485–2491, 2015.

[14] L. Chen, A. Beckett, A. Verma, and D. A. Feinberg. Dynamics of respiratory and cardiac CSF motion revealed with real-time simultaneous multi-slice epi velocity phase contrast imaging. *Neuroimage*, 122:281–287, 2015.

[15] K. Takizawa, M. Matsumae, S. Sunohara, S. Yatsushiro, and K. Kuroda. Characterization of cardiac-and respiratory-driven cerebrospinal fluid motion based on asynchronous phase-contrast magnetic resonance imaging in volunteers. *Fluids Barriers CNS*, 14(1):25, 2017.

[16] S. Yatsushiro, S. Sunohara, H. Atsumi, M. Matsumae, and K. Kuroda. Visualization and characterization of cerebrospinal fluid motion based on magnetic resonance imaging. *Hydrocephalus: Water on the Brain*, page 9, 2018.

[17] S. Yildiz, S. Thyagaraj, N. Jin, X. Zhong, Heidari P. S., B. A. Martin, F. Loth, J. Oshinski, and K. G. Sabra. Quantifying the influence of respiration and cardiac pulsations on cerebrospinal fluid dynamics using real-time phase-contrast MRI. *J Magn Reson Imaging*, 46(2):431–439, 2017.

[18] S Friese, U Hamhaber, M Erb, W Kueker, and U Klose. The influence of pulse and respiration on spinal cerebrospinal fluid pulsation. *Invest. Radiol.*, 39(2):120–130, 2004.

[19] S. Yamada, M. Miyazaki, Y. Yamashita, C. Ouyang, M. Yui, M. Nakahashi, S. Shimizu, I. Aoki, Y. Morohoshi, and J. G. McComb. Influence of respiration on cerebrospinal fluid movement using magnetic resonance spin labeling. *Fluids Barries CNS*, 10(1): 36, 2013.

[20] G. Ringstad, K. E. Emblem, O. Geier, N. Alperin, and P. K. Eide. Aqueductal stroke volume: comparisons with intracranial pressure scores in idiopathic normal pressure hydrocephalus. *Am. J. Neuroradiol.*, 36(9):1623–1630, 2015.

[21] J. Shanks, K. Markenroth Bloch, K. Laurell, K. G. Cesarini, M. Fahlström, E.-M. Larsson, and J. Virhammar. Aqueductal CSF stroke volume is increased in patients with idiopathic normal pressure hydrocephalus and decreases after shunt surgery. *Am. J. Neuroradiol.*, 40(3):453–459, 2019.

[22] K. Markenroth Bloch, J. Töger, and F. Ståhlberg. Investigation of cerebrospinal fluid flow in the cerebral aqueduct using high-resolution phase contrast measurements at 7T MRI. *Acta Radiol.*, 59(8):988–996, 2018.

[23] A. L. Sánchez, C. Martínez-Bazan, C. Gutiérrez-Montes, E. Criado-Hidalgo, G. Pawlak, W. Bradley, V. Haughton, and J. C. Lasheras. On the bulk motion of the cerebrospinal fluid in the spinal canal. *J. Fluid Mech.*, 841:203–227, 2018.

[24] J. J. Lawrence, W. Coenen, A. L. Sánchez, G. Pawlak, C. Martínez-Bazán, V. Haughton, and J. C. Lasheras. On the dispersion of a drug delivered intrathecally in the spinal canal. *J. Fluid Mech.*, 861:679–720, 2019.

[25] J. C. Tannehill, D. A. Anderson, and R. H. Pletcher. *Computational Fluid Mechanics and Heat Transfer*. Taylor & Francis, 2 edition, 1997.

[26] K. King. Private Communication, 2019.

[27] H. Stephensen, M. Tisell, and C. Wikkelsö. There is no transmantle pressure gradient in communicating or noncommunicating hydrocephalus. *Neurosurgery*, 50(4):763–773, 2002.

[28] P. K. Eide and T. Sæhle. Is ventriculomegaly in idiopathic normal pressure hydrocephalus associated with a transmantle gradient in pulsatile intracranial pressure? *Acta Neurochir. (Wien)*, 152(6):989–995, 2010.

Chapter 3

Transmantle pressure computed from MR measurements of aqueduct flow and dimensions

3.1 Introduction

Transmantle pressure, the instantaneous pressure difference between the lateral ventricles and the cranial subarachnoid space (SAS), drives cyclic cerebrospinal fluid flow in and out of the ventricles through the cerebral aqueduct. The aqueductal flow velocities driven by transmantle pressure have clinical potential value in triaging patients with normal pressure hydrocephalus [1, 2], investigating the pathogenesis of hydrocephalus [3], and understanding the effects of craniotomy (trephination) [4, 5] or lumbar puncture [6] and in other indications. Transmantle pressure can be measured using simultaneous readings from dual pressure sensors placed surgically into the cranial vault. However, there is a need to develop an accurate methodology to calculate it through non-intrusive methods. This represents a challenge since the transmantle pressure is very small. Results of direct measurements in both humans and animals typically show small differences or differences within the experimental error of measurement.[7–10] Therefore, some prior studies have argued that these small changes of transmantle pressure could not be responsible for the development of hydrocephalus.[9, 10]

Pressure drop is approximately proportional to the fluid acceleration, which increases in narrow channels such as the cerebral aqueduct. The pressure drop between the lateral ventricles and the subarachnoid space is then mainly due to that occurring along the aqueduct, which is the lengthiest narrow passage in the ventricular system.[11] Therefore, non-invasive calculations of transmantle pressure typically focus on measuring the flow acceleration along the cerebral aqueduct.[11–14] These non-invasive computational studies estimate small transmantle pressure values on the order of a few Pascals, consistent with those measured invasively. However, previously reported calculations of transmantle pressure were done on a limited number of subjects, neglected relevant flow effects like convective acceleration, and/or relied on full computational fluid dynamics (CFD) simulations that are difficult to implement clinically.

The goal of this study was to compute transmantle pressure from non-invasive aqueduct flow measurements using the simplified non-dimensional fluid mechanics model presented in the preceding chapter [15], which accounts for the specific anatomical features of the aqueduct and relevant effects of local fluid acceleration, convective acceleration, and viscous forces. We applied this novel methodology to a group of volunteers to investigate differences related to age, sex, flow and variations such as stroke volume, aqueduct length and cross-sectional area on the transmantle pressure.

3.2 Materials and methods

3.2.1 Study subjects

Subjects for this study were participants in a brain aging study funded by the LK Whittier Foundation (n = 48) and patients (n = 34) in a brain health and memory loss clinic and healthy student volunteers (n = 5). All subjects signed consent for enrollment in this IRB approved. Individuals with known neurologic or neurosurgical disorders were excluded. In the memory loss clinic group, individuals with a Clinical Dementia Rating of

greater than 0.5 of 5 were excluded [16]. Written informed consent for inclusion in the study was obtained for all participants. All images were reviewed by a neuroradiologist to identify and exclude cases of acute or obstructive hydrocephalus and other abnormalities. Subjects' blood pressure and/or arterial pulse pressure was not recorded for this study.

3.2.2 MRI acquisition

Imaging was performed with a 3T Signa scanner (software Version HD23; GE Healthcare, Milwaukee, Wisconsin) with an 8-channel head coil. The MR imaging sequences included the routine localizer, axial, coronal and sagittal T1 and T2 weighted images. Sequences obtained included a sagittal 3D inversion recovery fast spoiled gradient echo (FSPGR) sequence with the following parameters: TR/TE = 6.9/2.5 ms, inversion time = 600 ms, flip angle = 8°, acquisition voxels were 0.9 x 0.9 x 1.2 mm, and a single-shot gradient recalled-echo 2D phase contrast sequence which was acquired perpendicular to the cerebral aqueduct, with the following parameters: TR/TE = 20/10 ms, encoding velocity (VENC) = 5-20 cm/s, flip angle = 20°, peripheral pulse gating with 30 retrospective cardiac phases, voxel size = 0.2 x 0.2 x 5.0 mm to 0.47 x 0.47 x 5.0 mm.

3.2.3 Flow analysis

PC-MRI images were processed in MATLAB (version R2019a, The Mathworks, Natick, MA). The investigator placed a cursor on the aqueduct in the average magnitude image. The program generated an optimal rectangular ROI around the cursor for Otsu's threshold algorithm and converted pixels in the ROI to a binary scale (graythresh). A boundary was computed separating the black and white pixels and the cross-sectional area of the aqueduct was calculated automatically as the area within the boundary (bwboundaries) (Figure3.1). Flow in each white pixel of the aqueduct area was calculated by linear magnitude weighted conversion of phase to velocity and background correction [17, 18]. If the temporal velocity difference in a voxel was larger than 1.1 times the velocity

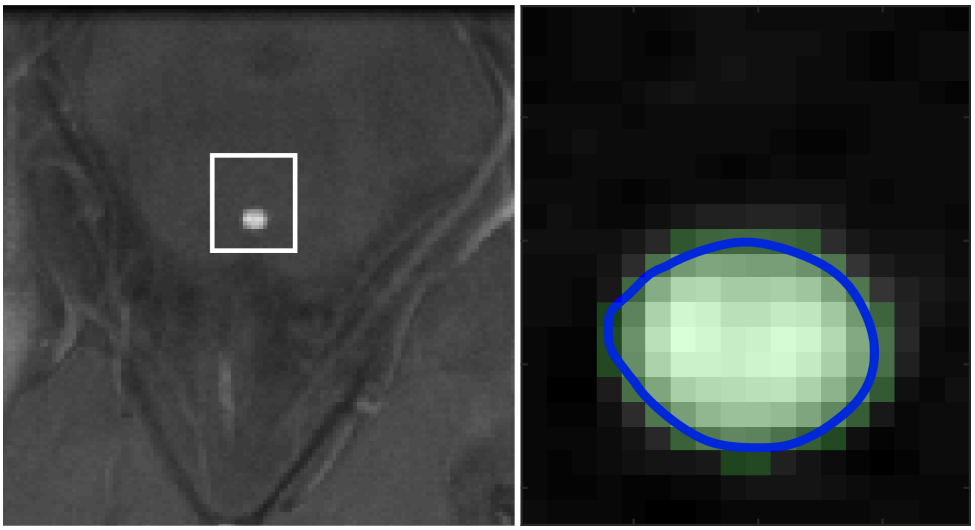

Figure 3.1. Axial PC-MRI magnitude image (left) illustrating the aqueduct and optimal ROI window (white line) and corresponding binary image (right) from Otsu's algorithm (light green) displaying the boundary (blue line) placed automatically overlaid onto the magnitude image.

encoding, anti-aliasing was performed [19]. The flow rate $Q(t)$, was computed by averaging the velocity magnitudes of all pixels within the aqueduct ROI and multiplying by the cross-sectional area. Caudal flow has a positive sign and rostral flow a negative sign [20]. The stroke volume was computed as half the integral of the flow rate [2]. Subjects with evident motion-related artifacts were excluded. In one subject imaged twice, inter-examination repeatability of the flow rate was calculated.

FSPGR images were used to segment the aqueduct semi-automatically using ITK-SNAP (Version 3.6.0; www.itksnap.org) [21]. The rostral and caudal ends of the aqueduct were identified manually as the point where the fluid lumen increased by 50%. The resulting 3D binary image stack was subsequently processed in MATLAB (version R2019a, The Mathworks, Natick, MA). The geometric centroids of the aqueduct cross-sectional area were automatically identified in the axial plane of the 3D image stack which was used along with the slice spacing to compute the length of the aqueduct (Figure 3.2).

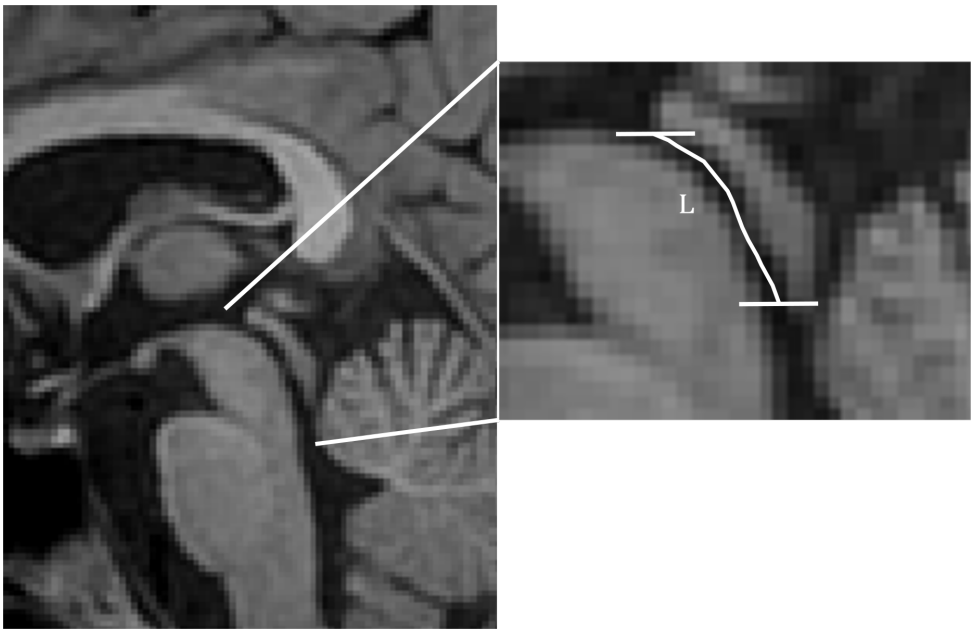

Figure 3.2. Sagittal FSPGR MR image (left) showing the aqueduct, third and fourth ventricles and a collimated image (right). Enlarged MR image (right) showing the length of the aqueduct by means of a line connecting its centroid at each slice (white line) and the horizontal lines showing the junction of the aqueduct with the third and fourth ventricles.

3.2.4 Transmantle pressure computation

The pressure difference between the third and fourth ventricles was calculated using the fully non-dimensional computational fluid dynamics method previously described in Sincomb et al. [15] One advantage of non-dimensionalization is that it reduces the computational cost while retaining The computation methodology accounts for all important physical phenomena affecting the pressure variation including the local acceleration, convective acceleration, and viscous forces. In this respect the model is superior in accuracy to one term formulas directly applicable to PC-MR image [22]. The main inputs to the model include the aqueduct length, aqueduct cross-sectional area, flow rate $Q(t)$, stroke volume, and heart rate. The cross-sectional area of the aqueduct was assumed to be constant along the length of the aqueduct for this computation. Each variable is scaled with its corresponding characteristic value. The density and kinematic viscosity of CSF were assumed as $\rho \simeq 103$ kg/m^3 and $\nu \simeq 0.71 \cdot 10^{-6}$ m^2/s, respectively. As mentioned

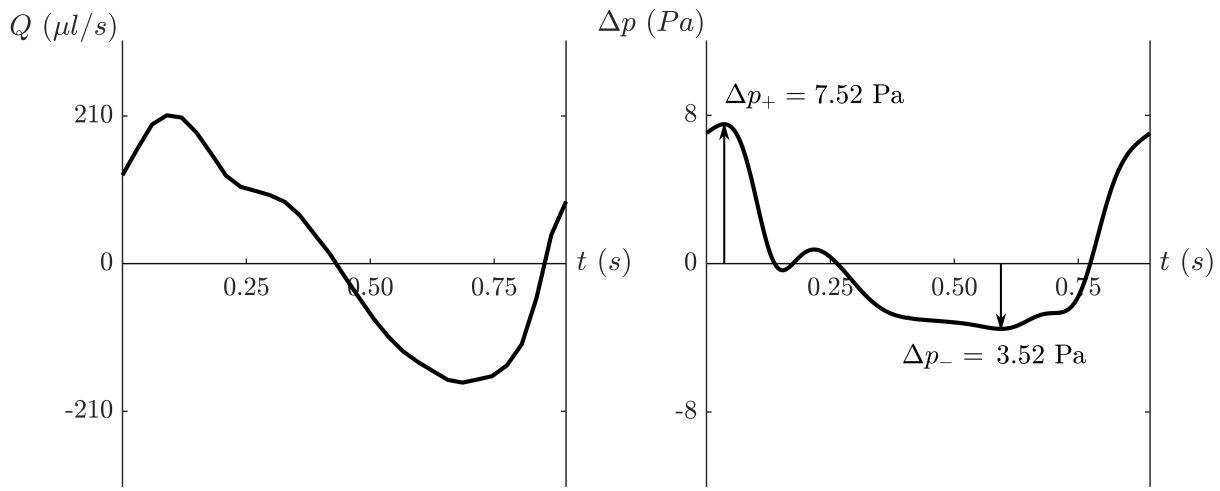

Figure 3.3. Plot of aqueduct flow (left) in a healthy 37-year old male with average heart rate of 67 BPM. Plot of the transmantle pressure (right) after entering variables into the nondimensional model [15] and converting back to dimensional pressure (in Pascals). On the plot of transmantle pressure the peak positive (Δp_+) and negative (Δp_-) transmantle pressures are demonstrated by arrows, representing peak pressures during caudal and rostral aqueduct flow, respectively

previously, the resulting transmantle pressure is calculated as the pressure difference between the third and fourth ventricle, given as $\Delta p = p_3(t) - p_4(t)$, since the drop in pressure across the foramen of Monro and the median aperture are an order of magnitude smaller. This estimate of the transmantle pressure also neglects spatial pressure variations in the SAS, because there the pressure is nearly uniform at any instant in time, and as such the spatial pressure differences never exceed a fraction of a Pascal as revealed in detailed CFD simulations of the entire cranial cavity [11]. Therefore, any obstruction in the subarachnoid space would result in a pressure estimate that would decrease the accuracy of the transmantle pressure. For this study we excluded subjects with an abnormal MRI.

For all subjects we computed the variation of transmantle pressure over a cardiac cycle (Figure 3.3). The variation of the transmantle pressure was then used to determine the peak positive transmantle pressure difference and negative transmantle pressure difference during caudal and rostral flow, respectively.

3.2.5 Statistical analysis

Differences in flow, anatomic and transmantle pressure values between males and females were tested by means of Mann-Whitney U test. Spearman rank correlation was used to assess the relationship between peak transmantle pressure values with aqueduct flow, age, heart rate, aqueduct length and aqueduct area. These relationships were illustrated with scatter plots. Statistical significance was set as a P-value ¡0.05.

3.3 Results

3.3.1 Study subjects

Of the 87 subjects, 9 subjects were excluded due to imaging artifacts such as motion. One subject with stroke volume greater than three times the average was excluded as an outlier which did not affect significant p-values. The subjects for this study included 77 individuals, 28 male and 49 female, ages 25 to 92 years (average 69±14 years) (Table 3.1). No subjects were excluded based on review of MR images. Male and female subjects on average had similar ages and heart rates (Table 3.1).

3.3.2 Flow analysis

Eight subjects had high velocities that exceeded our VENC and thus benefited from anti-aliasing. The subject scanned twice for inter-examination repeatability showed a difference in estimated cross-sectional area of 5.6% and peak flow rates of 3.2% (Figure 3.4). In the 77 subjects, the cross-sectional area of the aqueduct averaged 3.15±1.03 mm2 and differed significantly (P = 0.016) between female and male. The aqueduct length averaged 17.3±2.8 mm and the stroke volume 40±20 μl. (Table 3.1).

3.3.3 Transmantle pressure

During caudal aqueduct CSF flow the peak positive transmantle pressure (higher pressure in the third ventricle than in fourth ventricle) in our participants, averaged 14.44±6.49 Pa and ranged from 1.63-31.77 Pa. During rostral aqueduct CSF flow, the negative transmantle pressure (higher pressure in the fourth ventricle than in the third) averaged 6.94±2.82 Pa and ranged from 1.80-14.01 Pa. Differences between females and males in transmantle pressures were not significant (Table 3.1).

3.3.4 Statistical analysis

Peak transmantle pressure during caudal flow correlates significantly with age (ρ = 0.33, P = 0.004), aqueduct length (ρ = 0.33, P = 0.004) and stroke volume (ρ = 0.51, P <0.001) (Table 2). It does not correlate with heart rate or aqueduct cross-sectional area, although the p value is near significance. Peak transmantle pressure during rostral flow correlates with aqueduct cross-sectional area (ρ = -0.28, P = 0.013), aqueduct length (ρ = 0.37, P = 0.001) and stroke volume (ρ = 0.28, P = 0.014). It does not correlate with heart rate or age (Table 3.2). Scatter plots of peak positive and negative transmantle pressure with age, heart rate, aqueduct cross-sectional area, aqueduct length and stroke volume are shown in Figures 3.5-3.6.

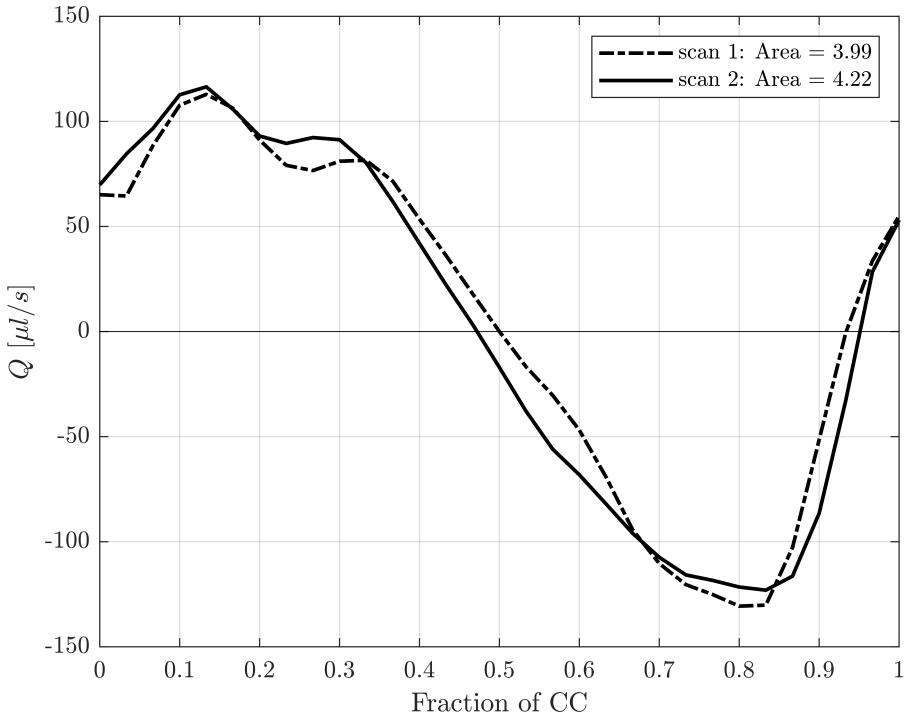

Figure 3.4. Flow rates measurements from same subject scanned at two different dates two months apart with same imaging protocol. For scan 1 and scan 2 the aqueduct cross-sectional area was computed as 3.99 mm^2 and 4.22 mm^2 and peak flow rates were computed as 112.9 μl/s and 116.4 μl/s, respectively.

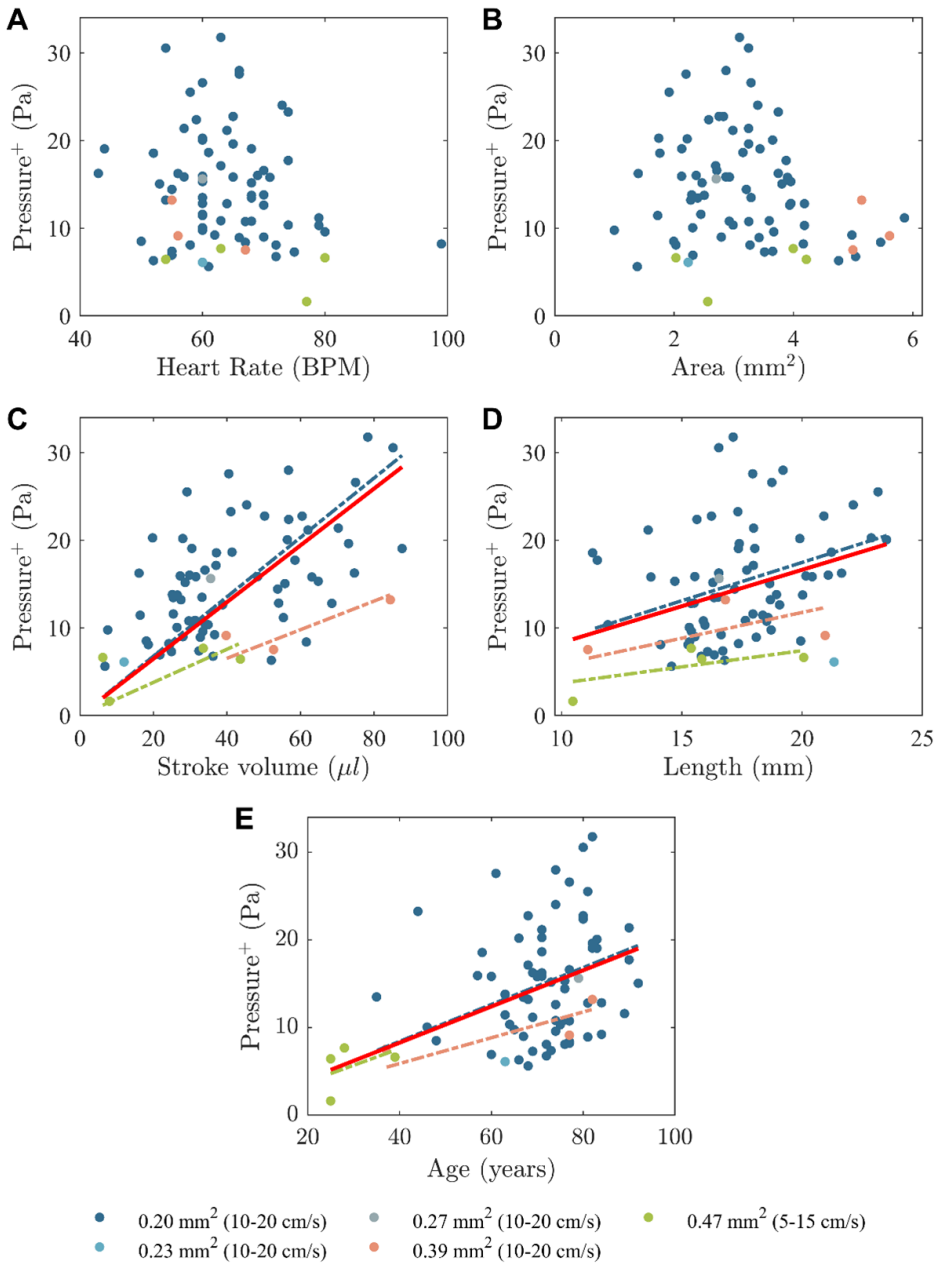

Figure 3.5. Peak transmantle pressure for all subjects and for subgroups of different voxel sizes (and VENC values) during caudal flow plotted against heart rate (A), aqueduct cross-sectional area (B), stroke volume (C), aqueduct length (D), and age (E) with trendlines including all subjects (red solid) and subgroups of different voxel sizes with greater than one subject. Transmantle pressure increases with stroke volume ($\rho = 0.51$, P <0.001), aqueduct length ($\rho = 0.33$, P = 0.004) and age ($\rho = 0.33$, P = 0.004) for all subjects. Transmantle pressure also increases in each subgroup, but not significantly.

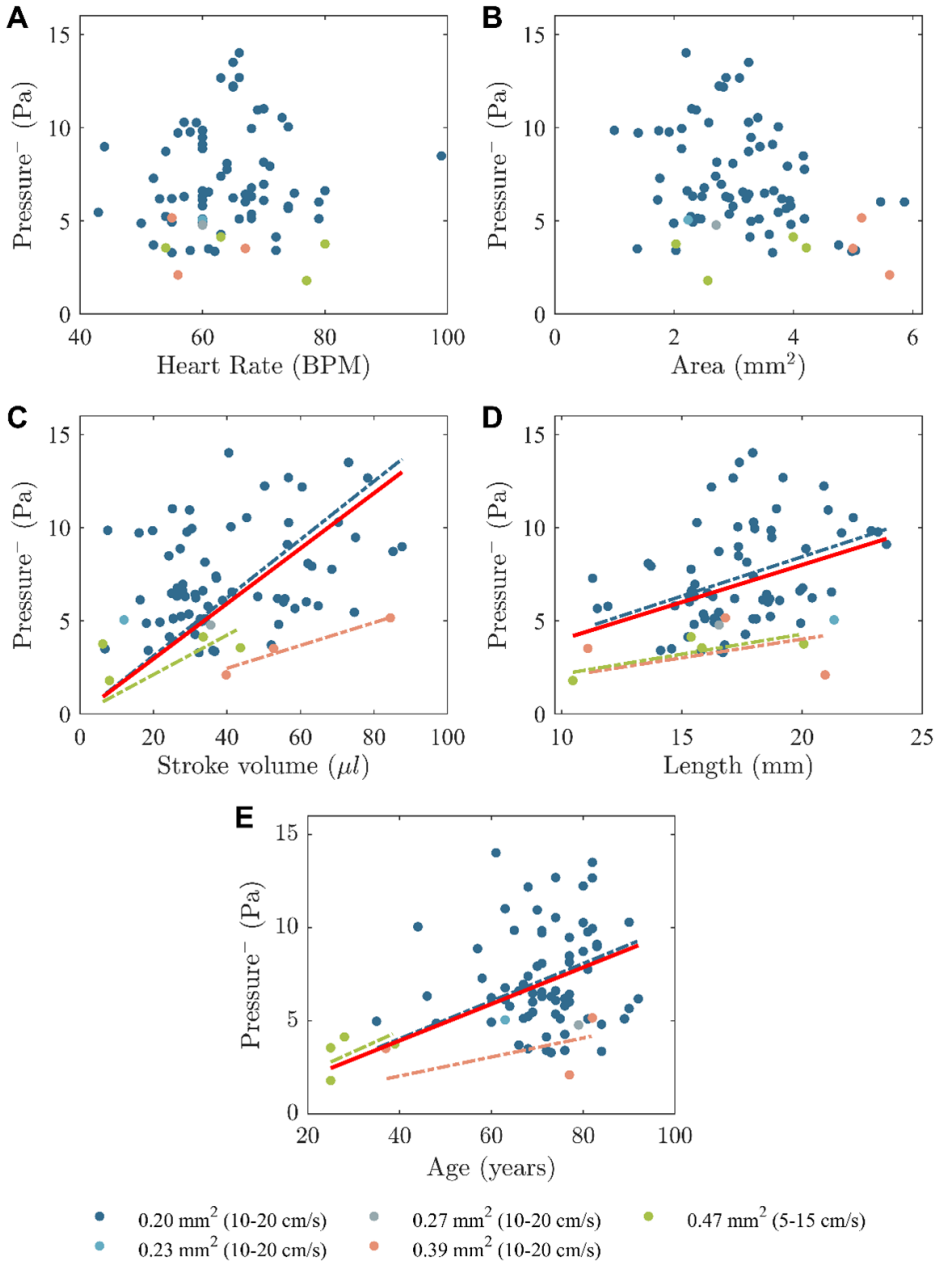

Figure 3.6. Peak transmantle pressure for all subjects and for subgroups of different voxel sizes (and VENC values) during rostral flow plotted against heart rate (A), aqueduct cross-sectional area (B), stroke volume (C), aqueduct length (D), and age (E) with trendlines including all subjects (red solid) and subgroups of different voxel sizes with greater than one subject. Transmantle pressure increases with stroke volume ($\rho = 0.28$, P = 0.014) and aqueduct length ($\rho = 0.37$, P = 0.001) for all subjects. The transmantle pressure tends to increase with age for the total group but does not reach significance ($\rho = 0.18$, P = 0.107). Transmantle pressure also increases in each subgroup, but not significantly.

Table 3.1. Age, heart rate, aqueduct flow and anatomic features and peak transmantle pressures

	Total n =77	Female n = 49	Male n =28	Sex P
Age (years)	69±14	72±13	65±16	0.114
Heart Rate (BPM)	64±9	63±7	66±11	0.305
Flow and Anatomic Features				
Area (mm^2)	3.15±1.03	2.90±0.88	3.58±1.13	0.016
Stroke volume (μl)	40±20	40±20	42±20	0.571
Length (mm)	17.3±2.8	16.9±2.8	18.0±2.5	0.065
Peak Transmantle Pressure				
Pressure+ (Pa)	14.44±6.49	14.54±6.13	14.25±7.18	0.564
Pressure- (Pa)	6.94±2.82	7.02±2.69	6.79±3.07	0.586

Table 3.2. Correlation of peak positive and negative transmantle pressure with age, heart rate, aqueduct area, stroke volume and aqueduct length

	Pressure$^+$ Pa		Pressure$^-$ (Pa)	
	Correlation Coefficient	P	Correlation Coefficient	P
Age (years)	0.33	0.004	0.18	0.107
Heart Rate (BPM)	-0.12	0.284	0.11	0.343
Area (mm^2)	-0.19	0.093	-0.28	0.013
Stroke volume (μl)	0.51	0.001	0.28	0.014
Length (mm)	0.33	0.004	0.37	0.001

$^+$Peak positive pressure during caudal flow
$^-$Peak negative pressure during rostral flow

3.4 Discussion

We found that peak transmantle pressure during caudal flow increased with age from 1.62 Pa in one 25-year-old subject to 15.05 Pa in the 92-year-old subject. This indicates the relevance of age in the estimation of transmantle pressure. Aqueduct length and stroke volume correlated significantly with transmantle pressures in both the caudal and rostral direction. Peak transmantle pressure is inversely correlated with aqueduct cross-sectional area during caudal flow in the aqueduct, but not significantly during the typically less rapid rostral flow, suggesting that viscous boundary layer effects must be

taken into consideration when computing the transmantle pressure.

Peak transmantle pressure computed with the non-dimensional computational model varied during the cardiac cycle from an average of 14.44±6.49 Pa during caudal flow in the aqueduct to 6.94±2.82 Pa during rostral flow. The computed peak transmantle pressure during caudal and rostral flow in this study are in general agreement with those in other computational studies [23–25] and also with measurements made with invasive methods in humans [9, 10] and in animals [7]. In reports in which tranmantle pressures were immeasurably small, the pressure sensors placed in the cranial vault had a resolution of 66 Pa which is greater than the typical transmantle pressure in our study [8]. To our knowledge, the peak pressures during both caudal and rostral flow have not been previously reported separately as we have done. This is important as the dynamics for caudal and rostral CSF flow (during systole and diastole respectively) are distinct and may reflect influences of different system properties. Some investigators have suggested that the ratio of peak transmantle pressures between systole and diastole may be useful, but we have not calculated that ratio. A ratio of values could be incorporated in future studies. The stroke volumes we measured in our volunteers also had similar magnitude to those in previous studies including healthy younger and elderly subjects [18, 26–28].

The study reported here is significant because it shows that computational fluid mechanics methods based on a non-dimensional formulation have sufficient precision to detect differences in transmantle pressure due to age or aqueduct dimensions, two important issues that have not been sufficiently evaluated to date. Our approach is also very different from previous studies related to transmantle pressure. For example, Sartoretti et al. [22], employs Bernoulli's equation written in the form $\Delta p = 4V_{max}^2$ to determine the pressure difference. This approach is only valid for steady flow, a condition that is not satisfied for the flow in the aqueduct. Holmlund et al. [29] implements a full computational fluid simulation that is computationally expensive and require specialized software. The computation used here can be performed with a readily available straightforward computer

program in a few minutes and may be easily applied in the clinical setting.

Computation of transmantle pressure may be preferable to measurement of aqueduct velocity or stroke volume as an index of abnormal CSF dynamics. Computational studies of transmantle pressures are warranted in NPH, pediatric communicating hydrocephalus and in other conditions with altered CSF dynamics. It should be noted that even small increases in the transmantle pressure with age may be significant in the development of NPH and other CSF altered conditions. Owing to the viscoelastic nature of the brain parenchyma even very small transmantle pressure may result in a gradual enlargement of the ventricles through the accumulation of small residual strain over months or years (tens of millions of cardiac cycles) while the mean intracranial pressure remains constant [30]. This methodology to estimate transmantle pressure may have a role in studies of factors affecting ventricular morphology [31].

This study has limitations. The normality of the volunteers was not rigorously tested. However, acute or obstructive hydrocephalus and other abnormal brain conditions detectable by MR that affect CSF dynamics were excluded by the neuroradiologist's review of MR images in each case. For PC-MRI acquisition, variation of VENC and in-plane resolution may have introduced some bias through velocity noise and partial volume effect, respectively [32, 33]. However, groups with the same in-plane resolution show the same trend for age and peak transmantle pressure. Neglecting longitudinal changes in cross-sectional area of the aqueduct, for example at the ampulla, may have diminished the accuracy of the pressure computations. We did not study the effect of respiration on transmantle pressure, although it may be relevant [34]. The test-retest precision of the pressure computation was not quantified, and it requires further study. Validation of the method also requires additional in-vivo and in-vitro experimentation.

Acknowledgements

Chapter 3, in full, is a reprint of the material as it appears in the American Journal of Neuroradiology, 2021. Sincomb, Stephanie; Coenen, Wilfried; Criado-Hidalgo, Ernesto; Wei, Ke; King, Kevin; Borzage, Matthew; Haughton, Victor and Sánchez, Antonio and Lasheras, Juan C. The dissertation author was the primary author of this paper.

Bibliography

[1] Dan Greitz. Radiological assessment of hydrocephalus: new theories and implications for therapy. *The neuroradiology journal*, 19(4):475–495, 2006.

[2] William G Bradley Jr, David Scalzo, John Queralt, Wolfgang N Nitz, Dennis J Atkinson, and Priscilla Wong. Normal-pressure hydrocephalus: evaluation with cerebrospinal fluid flow measurements at mr imaging. *Radiology*, 198(2):523–529, 1996.

[3] William G Bradley Jr, Gautam Bahl, and John F Alksne. Idiopathic normal pressure hydrocephalus may be a "two hit" disease: benign external hydrocephalus in infancy followed by deep white matter ischemia in late adulthood. *Journal of Magnetic Resonance Imaging: An Official Journal of the International Society for Magnetic Resonance in Medicine*, 24(4):747–755, 2006.

[4] Mark E Wagshul, Shams Rashid, James P McAllister, and Martin U Schuhmann. The effect of decompressive craniectomy on csf pulsatility in experimental communicating hydrocephalus. *Cerebrospinal Fluid Research*, 7(1):1–2, 2010.

[5] Antonio Scollato, Pasquale Gallina, Gautam Bahl, and Nicola Di Lorenzo. Decompressive craniectomy arrests pulsatile aqueductal csf flux: an in vivo demonstration using phase-contrast mri. case report. *British journal of neurosurgery*, 29(3):440–442, 2015.

[6] AM Blitz, J Shin, O Baledent, G Page, LW Bonham, DA Herzka, AR Moghekar, and D Rigamonti. Does phase-contrast imaging through the cerebral aqueduct predict the outcome of lumbar csf drainage or shunt surgery in patients with suspected adult hydrocephalus? *American Journal of Neuroradiology*, 39(12):2224–2230, 2018.

[7] E Scott Conner, Lorraine Foley, and Peter McL Black. Experimental normal-pressure hydrocephalus is accompanied by increased transmantle pressure. *Journal of neurosurgery*, 61(2):322–327, 1984.

[8] Richard D Penn, Max C Lee, Andreas A Linninger, Keith Miesel, Steven Ning Lu, and Lee Stylos. Pressure gradients in the brain in an experimental model of hydrocephalus. *Journal of neurosurgery*, 102(6):1069–1075, 2005.

[9] Hannes Stephensen, Magnus Tisell, and Carsten Wikkelsö. There is no transmantle pressure gradient in communicating or noncommunicating hydrocephalus. *Neurosurgery*, 50(4):763–773, 2002.

[10] Per Kristian Eide and Terje Sæhle. Is ventriculomegaly in idiopathic normal pressure hydrocephalus associated with a transmantle gradient in pulsatile intracranial pressure? *Acta neurochirurgica*, 152(6):989–995, 2010.

[11] Brian Sweetman, Michalis Xenos, Laura Zitella, and Andreas A Linninger. Three-dimensional computational prediction of cerebrospinal fluid flow in the human brain. *Computers in biology and medicine*, 41(2):67–75, 2011.

[12] Erica E Jacobson, David F Fletcher, Michael K Morgan, and Ian H Johnston. Fluid dynamics of the cerebral aqueduct. *Pediatric neurosurgery*, 24(5):229–236, 1996.

[13] Erica E Jacobson, David F Fletcher, Michael K Morgan, and Ian H Johnston. Computer modelling of the cerebrospinal fluid flow dynamics of aqueduct stenosis. *Medical & biological engineering & computing*, 37(1):59–63, 1999.

[14] Gérald Bardan, Franck Plouraboué, Mokhtar Zagzoule, and Olivier Balédent. Simple patient-based transmantle pressure and shear estimate from cine phase-contrast mri in cerebral aqueduct. *IEEE transactions on biomedical engineering*, 59(10):2874–2883, 2012.

[15] Stephanie Sincomb, Wilfried Coenen, AL Sánchez, and JC Lasheras. A model for the oscillatory flow in the cerebral aqueduct. *Journal of Fluid Mechanics*, 899, 2020.

[16] Charles P Hughes, Leonard Berg, Warren Danziger, Lawrence A Coben, and Ronald L Martin. A new clinical scale for the staging of dementia. *The British journal of psychiatry*, 140(6):566–572, 1982.

[17] Costanza Simoncini. *Patient specific numerical modelling for the optimisation of HCC selective internal radiation therapy an image based approach*. PhD thesis, Rennes 1, 2017.

[18] Dieter R Enzmann and Norbert J Pelc. Cerebrospinal fluid flow measured by phase-contrast cine mr. *American journal of neuroradiology*, 14(6):1301–1307, 1993.

[19] Erika Kristina Lindstrøm, Geir Ringstad, Kent-Andre Mardal, and Per Kristian Eide. Cerebrospinal fluid volumetric net flow rate and direction in idiopathic normal

pressure hydrocephalus. *NeuroImage: Clinical*, 20:731–741, 2018.

[20] Vincent Puy, Jadwiga Zmudka-Attier, Cyrille Capel, Roger Bouzerar, Jean-Marie Serot, Anne-Marie Bourgeois, Jérome Ausseil, and Olivier Balédent. Interactions between flow oscillations and biochemical parameters in the cerebrospinal fluid. *Frontiers in aging neuroscience*, 8:154, 2016.

[21] Khalid Ambarki, Tomas Lindqvist, Anders Wåhlin, Erika Petterson, Marcel Jan Bertus Warntjes, Richard Birgander, Jan Malm, and Anders Eklund. Evaluation of automatic measurement of the intracranial volume based on quantitative mr imaging. *American journal of neuroradiology*, 33(10):1951–1956, 2012.

[22] Thomas Sartoretti, Michael Wyss, Elisabeth Sartoretti, Carolin Reischauer, Nicolin Hainc, Nicole Graf, Christoph Binkert, Arash Najafi, and Sabine Sartoretti-Schefer. Sex and age dependencies of aqueductal cerebrospinal fluid dynamics parameters in healthy subjects. *Frontiers in aging neuroscience*, 11:199, 2019.

[23] David N Levine. The pathogenesis of normal pressure hydrocephalus: a theoretical analysis. *Bulletin of mathematical biology*, 61(5):875–916, 1999.

[24] David N Levine. Intracranial pressure and ventricular expansion in hydrocephalus: have we been asking the wrong question? *Journal of the neurological sciences*, 269 (1-2):1–11, 2008.

[25] Andreas A Linninger, Michalis Xenos, David C Zhu, MahadevaBharath R Somayaji, Srinivasa Kondapalli, and Richard D Penn. Cerebrospinal fluid flow in the normal and hydrocephalic human brain. *IEEE Transactions on Biomedical Engineering*, 54 (2):291–302, 2007.

[26] Olivier Balédent, Catherine Gondry-Jouet, Marc-Etienne Meyer, Giovanni De Marco, Daniel Le Gars, Marie-Cécile Henry-Feugeas, and Ilana Idy-Peretti. Relationship between cerebrospinal fluid and blood dynamics in healthy volunteers and patients with communicating hydrocephalus. *Investigative radiology*, 39(1):45–55, 2004.

[27] Souraya Stoquart-ElSankari, Pierre Lehmann, Agnès Villette, Marek Czosnyka, Marc-Etienne Meyer, Hervé Deramond, and Olivier Balédent. A phase-contrast mri study of physiologic cerebral venous flow. *Journal of Cerebral Blood Flow & Metabolism*, 29 (6):1208–1215, 2009.

[28] Armelle Lokossou, Serge Metanbou, Catherine Gondry-Jouet, and Olivier Balédent. Extracranial versus intracranial hydro-hemodynamics during aging: a pc-mri pilot cross-sectional study. *Fluids and Barriers of the CNS*, 17(1):1–11, 2020.

[29] Petter Holmlund, Sara Qvarlander, Jan Malm, and Anders Eklund. Can pulsatile

csf flow across the cerebral aqueduct cause ventriculomegaly? a prospective study of patients with communicating hydrocephalus. *Fluids and Barriers of the CNS*, 16(1): 1–10, 2019.

[30] Stephanie Sincomb, Victor Haughton, Antonio Sanchez, Ernesto Criado-Hidalgo, and Juan C Lasheras. Strain accumulation visco-elastic ventriculomegaly hypothesis for the onset of idiopathic normal pressure hydrocephalus (inph). *Biophysical Journal*, 118(3):452a, 2020.

[31] William W Chiang, Christos G Takoudis, Sang H Lee, Annette Weis-McNulty, Roberta Glick, and Noam Alperin. Relationship between ventricular morphology and aqueductal cerebrospinal fluid flow in healthy and communicating hydrocephalus. *Investigative radiology*, 44(4):192–199, 2009.

[32] Chao Tang, Duane D Blatter, and Dennis L Parker. Accuracy of phase-contrast flow measurements in the presence of partial-volume effects. *Journal of Magnetic Resonance Imaging*, 3(2):377–385, 1993.

[33] Joachim Lotz, Christian Meier, Andreas Leppert, and Michael Galanski. Cardiovascular flow measurement with phase-contrast mr imaging: basic facts and implementation. *Radiographics*, 22(3):651–671, 2002.

[34] Vegard Vinje, Geir Ringstad, Erika Kristina Lindstrøm, Lars Magnus Valnes, Marie E Rognes, Per Kristian Eide, and Kent-Andre Mardal. Respiratory influence on cerebrospinal fluid flow–a computational study based on long-term intracranial pressure measurements. *Scientific reports*, 9(1):1–13, 2019.

Chapter 4

Experimental validation of the cerebral aqueduct flow model: preliminary results

4.1 Introduction

Normal pressure hydrocephalus (NPH) is a disease that is characterized by disturbed gait, dementia, and enlarged lateral ventricles (ventriculomegaly), in the absence of elevated intracranial pressure (ICP) and blockage of any passages within the ventricular system. It typically affects the elderly population, those older than 60 years old, with a prevalence that varies amongst reports due to under-diagnosis [1]. Both men and women are equally affected [2]. NPH is diagnosed clinically through assessment of symptoms like gait using a walking test after external lumbar puncture [3], but is often difficult to assess because symptoms overlap with those of other neurogenerative diseases such as Alzheimer's. This disease is particularly interesting because it has been deemed as the only potentially reversible neurogenerative disease [4]. The standard treatment for NPH, ventriculoperitoneal shunting, an invasive method requiring surgery to remove the excess CSF, results in anywhere between 24-100% success rate in relieving symptoms [5]. It is worth noting that, even decades since its initial description, the exact etiology of NPH is still unknown.

It has been argued that transmantle differences in pulsatile intracranial pressure play a role in enlarging the ventricles [6]. Transmantle pressure can be measured using simultaneous readings from dual pressure sensors placed surgically into the cranial vault, an invasive procedure with inherent risks, including hemorrhage and infection [7]. An alternative non-invasive estimate of the transmantle pressure using phase-contrast (PC) MRI to model the aqueduct flow has been proposed in Chapter 2, with resulting transmantle pressure predictions lying within the range of values obtained by direct measurement [8].

Our mathematical model, based on rigorous asymptotic reduction of the Navier-Stokes equations, achieves reasonably good computational efficiency while accounting for all relevant flow effects. It provides results that are more accurate than those obtained with ad-hoc flow models, including fully developed unidirectional Womersley-like flow [9] and a simplified hydraulic model [10], at a fraction of the computational cost involved in CFD studies [11–14]. As discussed in Chapter 3, the model was used in a clinical study to determine the effect of age, gender, heart rate, and aqueduct dimensions on transmantle pressure, with results published in [15]. However, the validation of our CSF-flow model has been restricted to comparisons with results of direct numerical simulations.

The goal of this study is to provide in-vitro validation by comparing computed results directly with measured pressure differences in an experimental model representing the aqueduct, third and fourth ventricle. In the preliminary results presented below, the aqueduct is represented by a rigid cylindrical tube. Additional experiments are to be conducted with the use made of an anatomically correct model, 3D printed using high-resolution MR images of the aqueduct, third and fourth ventricles. Although the model size is approximately ten times larger than the human aqueduct, as needed to enable pressure measurements to be made, care is taken to maintain physical similarity by ensuring that the main dimensionless flow parameters are kept constant in scaling the problem, which will require changes in the flow frequency and properties of the working fluid. A programmable pump (ViVitro Labs Inc.) will be used to generate a flow rate

signal with a cyclical time variation. Besides a flow rate of sinusoidal form, the experiments consider the specific waveform measured in phase contrast MRI measurements of the aqueduct flow. The differential pressure measurements will be used to compare with our mathematical model.

4.2 Geometrical and physical similarity

To validate the model, one could design an experiment mimicking exactly the cerebral aqueduct conditions. The setup would involve a tiny canal whose shape and size would have to be identical to those of the human aqueduct (i.e. $L \simeq 10 - 20$ mm and $a_c \simeq 1 - 2$ mm), a micropump able to deliver oscillating flow rates with peak values on the order of 0.1 ml/s, and a sensor with the capability of measuring pressure differences of a few pascals with sufficient accuracy. Of course, such an experiment would be extremely difficult, both because handling such a small size would be challenging and because the devices that are required to deliver/measure accurately such small flow rates/pressure differences are not readily available. What we need instead is to scale up the aqueduct model as well as the resulting flow rate and pressure difference, in such a way that the experiment can be performed in the lab using the available resources. The purpose of this section is that of describing the guidelines followed in the design.

To guarantee that the results of the experiment represent the flow in the human aqueduct, the experimental model must be geometrically similar to the human aqueduct, that is, its shape, including its aspect ratio a_c/L, must be identical to that found in the human brain, but its size could be larger, thereby facilitating the experimental manipulation. Also, the experimental conditions must be physically similar to those found in the human aqueduct, in that all dimensionless governing parameters must take the same values in the experiment and the human brain. One could identify the governing parameters simply by inspection of the dimensionless formulation presented earlier in Chapter 2, but it is

more instructive to use directly the familiar Buckingham Π theorem, as explained in the following paragraph.

Consider oscillating flow in a cylindrical canal connecting two large vessels. The amplitude of the pressure difference between the containers changes periodically. Its peak-to-peak amplitude Δp depends on the size of the canal, measured for example by its length, on the properties of the fluid (i.e. its density ρ and kinematic viscosity ν), on the stroke volume being displaced back and forth along the canal V, and on the frequency of the oscillatory motion (for the aqueduct flow, we may use the heart rate HR to characterize the frequency). This functional dependence can be expressed in the form

$$\Delta p = \Delta p(L, \rho, \nu, V, \mathrm{HR}). \tag{4.1}$$

Since the dependence enters through five parameters, three of which have independent dimensions, a straightforward application of the Π theorem allows us to reduce the dependence from five-dimensional parameters to two dimensionless parameters. If we choose to eliminate L, ρ, and HR, then the result can be expressed in the form

$$\frac{\Delta p}{\rho\,\mathrm{HR}^2\,L^2} = f\left(\frac{\nu}{L^2\,\mathrm{HR}}, \frac{V}{L^3}\right). \tag{4.2}$$

This last equation reveals that if two flows involving geometrically similar canals with different size have the same values of $\nu/(L^2\,\mathrm{HR})$ and V/L^3, then the resulting values of the dimensionless pressure amplitude $\Delta p/(\rho\,\mathrm{HR}^2\,L^2)$ would be the same in both. Therefore, to guarantee physical similarity, the heart rate, stroke volume, and kinematic viscosity of the experiment (denoted by the subscript E) must be related to those of the human aqueduct (denoted by the subscript H) by

$$\frac{\nu_E/\nu_H}{\mathrm{HR}_E/\mathrm{HR}_H} = \chi^2 \quad \text{and} \quad \frac{V_E}{V_H} = \chi^3 \tag{4.3}$$

where $\chi = L_E/L_H$ is the scaling factor. When the above relations are satisfied, then the interventricular pressure difference Δp_H can be computed in terms of the pressure difference measured between the containers (Δp_E) with use made of

$$\frac{\Delta p_E}{\Delta p_H} = \frac{\rho_E}{\rho_H}\left(\frac{\mathrm{HR}_E}{\mathrm{HR}_H}\right)^2 \chi^2. \tag{4.4}$$

Using the first equation in (4.3) in (4.4) to eliminate the heart rate yields

$$\frac{\Delta p_E}{\Delta p_H}\chi^2 = \frac{\rho_E}{\rho_H}\left(\frac{\nu_E}{\nu_H}\right)^2, \tag{4.5}$$

which indicates that in order for the size and pressure differential of the experiment to be larger than those of the cerebral aqueduct, the working fluid in the experiment must be significantly more viscous than CSF, thereby motivating the use of glycerol and water mixture.

4.3 Experimental setup

The Super Pump AR (ViVitro Labs, Victoria, Canada) was used for generating the flow rate. We use both a sine wave and a customized waveform, shown in Fig. 4.1, matching the subject's signal in the cerebral aqueduct, as measured by PC MRI. The waveform is normalized for import into the pump. As a functionality of the pump, a stroke volume can be chosen so the amplitude of the flow rate is adjustable within the limits of the pump. This includes that the heart rate is between 3-200 BPM, and the stroke volume must be between 0-180 mL/stroke.

An image of the complete setup can be seen in Figure 4.2b. The pump was connected with semi-rigid tubing to a ball valve that is then connected to the first reservoir. Between the reservoirs is an acrylic tube 0.75" ID ($a_c = 0.95$ cm) secured using acrylic cement, with silicone glue surrounding the seam to ensure no leakage. The reservoirs are

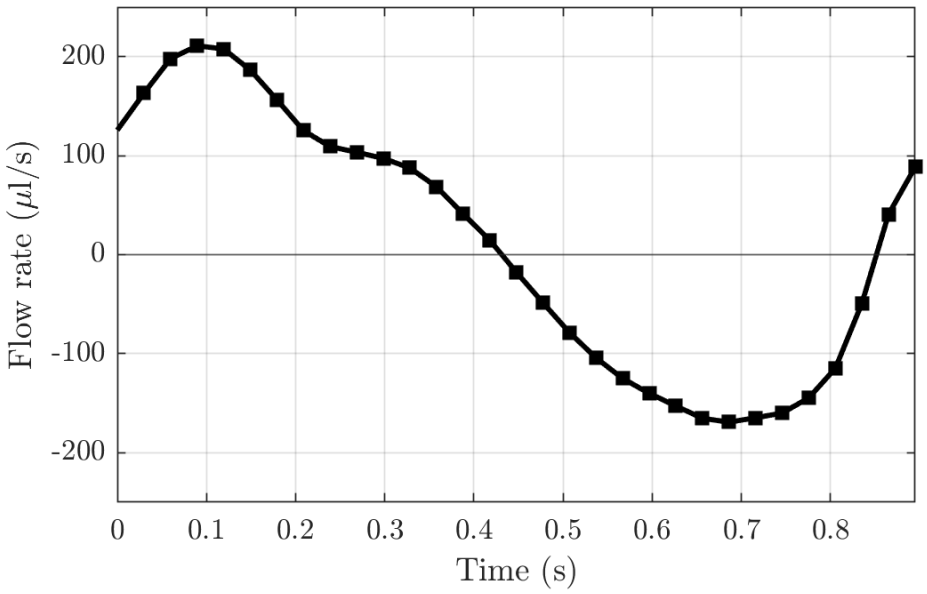

Figure 4.1. Flow rate signal from MRI phase contrast of a healthy subject used for input into the pulsatile pump.

constructed using 1/2" acrylic sheets and assembled with acrylic cement to an inner size of 5"x5"x5". The size of the reservoirs was chosen to ideally match the dynamics reported in the third ventricle [14]. A latex balloon was partially filled with air and included in the reservoir to allow for compliance. The assembly was carefully filled to avoid air bubbles with water or glycerol-water mixture.

High-resolution anatomic MRI images were used to segment the aqueduct CSF using ITK-SNAP (Version 3.6.0; www.itksnap.org) [16]. The resulting segmentation model was then scaled by a factor of 10 and smoothed (Autodesk Meshmixer). The segmentation represents the lumen of the cerebral aqueduct and was offset by 3 mm to create a hollow model with sufficient thickness to withstand the hydrostatic pressure. End attachment flanges were designed in Autodesk Fusion 360 and added to the model in Meshmixer. The final model was exported as a stereo-lithography (STL) file to use for 3D printing.

The final model including the flanges was printed on a Form 3 Stereolithography (SLA) resin desktop 3D printer using clear resin (Formlabs). Printing was performed at a

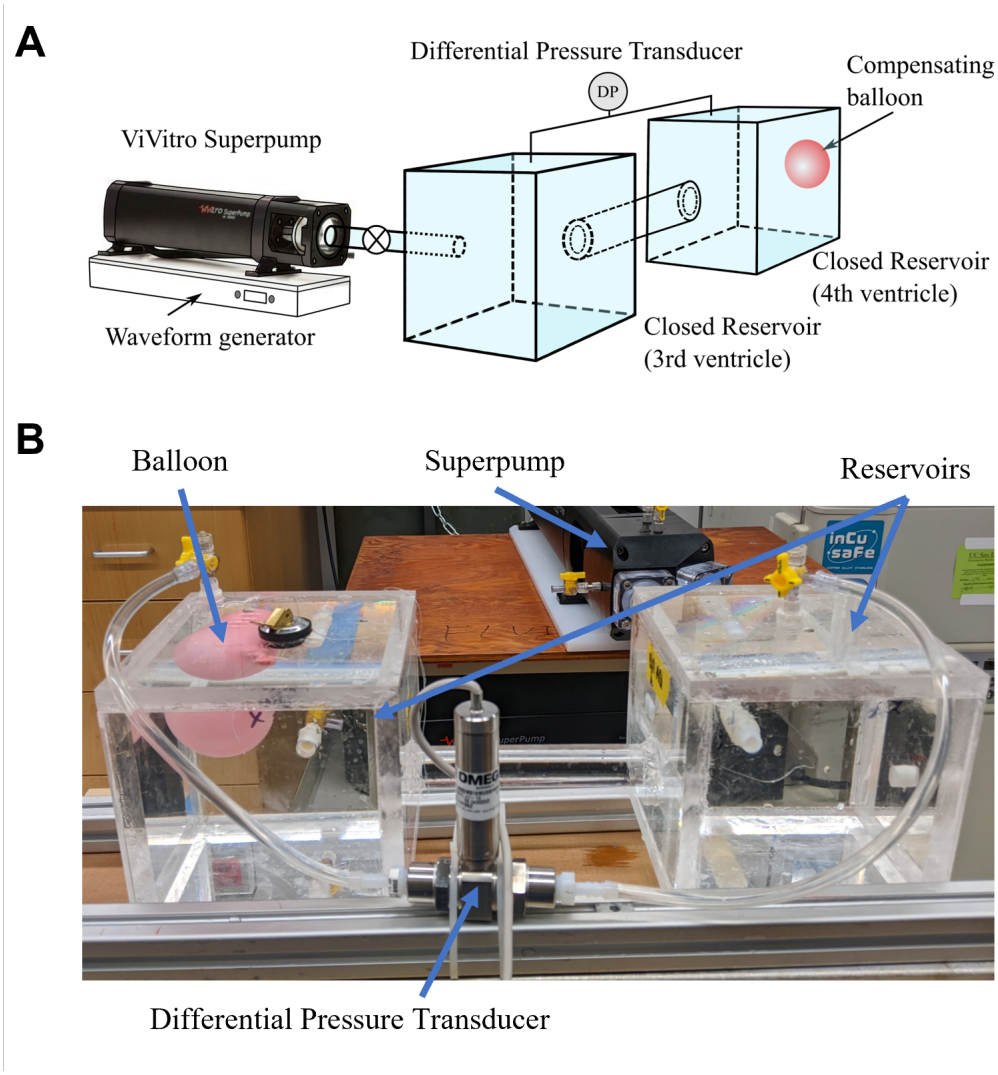

Figure 4.2. A) Illustration of canonical experimental setup with cylindrical tube representing the aqueduct. B) Image of experimental setup with appropriate labels.

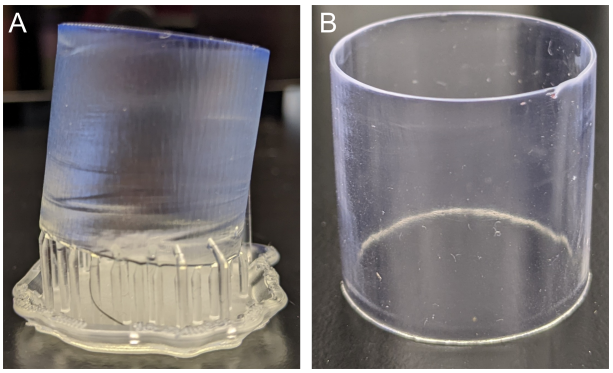

Figure 4.3. A) Simple 2 mm thick hollow cylinder before post-processing and support removal. B) Part after washing, curing, removing supports, sanding and polishing for transparency.

fine resolution (0.05 mm) which helped balance the resolution and total print time. After printing was complete the printed part was post-processed to achieve an optical clarity to enable future use of a fluid imaging technique known as Particle Image Velocimetry (PIV). The printed part is cleaned in isopropyl alcohol (IPA) to remove uncured resin from the print surfaces. The model is then UV-cured and wet-sanded using grit paper from 800-3000. It is cleaned and polished following the Novus plastic polish kit and once dried, coated with a UV-resistant clear gloss (Krylon). An example of the level of transparency that can be achieved is seen in Figure 4.3.

Differential pressure measurements were made using an Omega pressure transducer (Item#: MMDWB10WUSBHW3D0T9A2). The customized details are provided in Table 4.1. Pressure signals were low-pass filtered at the cardiac frequency to remove noise and zero-meaned. Accurate readings require minimum pressure differences greater than 20 Pa, a condition that was always achieved in our scaled model.

4.4 Preliminary results

A sinusoidal flow rate was used in the first set of measurements, with the stroke volume of the pump chosen as $V_E = 40$ ml/stroke to be within the pump's operational limits. The values of the different parameters for these tests are provided in Table 4.2. All tests

Table 4.1. Differential pressure transducer configuration.

Name	Description
Transducer Material	316L Stainless Steel
Process fitting	1/4-18 NPT Female
Pressure type	Differential Wet/Wet Bidirectional
Range unit	in-H2O (4°C)
in-H2O	10
Pressure transducer output	USB (high-speed)
Pressure transducer accuracy	±0.08% B.S.L.
Electrical termination	Cable (2m, 6ft)
Temperature range	18 to 85°C (-0 to 185°F)
Thermal accuracy: Zero shift / Span shift	±0.80% / ±0.60%

were conducted at ambient temperature. The resulting pressure difference measurements are shown in Figure 4.4 as an averaged single cycle for each case. The results are compared with the predictions obtained with our simplified model. As expected, the differential pressure increases with increasing heart rate.

Reasonably good agreement is found between the pressure variation measured in the experiments and the theoretical predictions. There are several sources of random and systemic errors that may contribute to the observed differences. For low-pressure differences, such as for 30 BPM, the signal-to-noise was very small, but the pressure transducer is sensitive to abrupt fluid motion, such as sudden increase of stroke volume or a fast heart rate. This was only remedied through slow transition and balancing the stroke volume and heart rate. Also, the presence of some air bubbles was inevitable and varied by experiment even when the experiment was set carefully and identically. Therefore, to reduce the random error induced by noise from the pressure transducer we sampled over many cycles and repeated the experiment several times. We do not anticipate, however, that these greatly alter the measured pressure difference. We believe the main source of the magnitude differences results from systematic errors. Particularly, the curved edge between the connected acrylic tube and faceplate. There was curvature but was limited by the thickness of the plate (1/2") and therefore the minimal curvature achieved may have

Table 4.2. Experimental parameters for sine waveform

Parameter				
Flow rate signal	$\sin(\omega t)$	$\sin(\omega t)$	$\sin(\omega t)$	$\sin(\omega t)$
Fluid	water	water	water	60% glycerol/water
Density ρ (kg/m^3)	1000	1000	1000	1156
Viscosity ν (m^2/s)	$0.71{\cdot}10^{-6}$	$0.71{\cdot}10^{-6}$	$0.71{\cdot}10^{-6}$	$1.0{\cdot}10^{-5}$
Heart rate (BPM)	30	60	80	60
Radius a_c (cm)	0.95	0.95	0.95	0.95
Length L (cm)	15.2	15.2	15.2	15.2
a_c/L	0.06	0.06	0.06	0.06
Stroke Length L_s (cm)	14.1	14.1	14.1	14.1
L_s/L	0.93	0.93	0.93	0.93
α	20	28	32	7.5

contributed to the error in providing a source of pressure loss. The exit from the piston head may be an additional source of pressure loss. The overall size of the reservoirs may not have been sufficiently large as well. These possible systematic errors will be corrected for in future work incorporating the 3D-printed aqueduct.

4.5 Concluding remarks

In this chapter, we sought to validate our previously proposed model for the flow in the cerebral aqueduct [8] with the use made of experiments conducted with a scaled physical model. The experimental setup for the canonical case, a simple cylindrical tube representing the cerebral aqueduct, was created to be a geometrical scale of 10. Both a sine wave and real flow rate signal were integrated into a pulsatile pump to mimic the oscillatory flow, although results are presented here only for the former case. Due to the volumetric size of the experimental set up we were limited on the range of stroke volumes and heart rates that can be applied to the system as well as to the pressure transducer. Despite this, we found that our experimental differential pressure measurements for a sine wave match the order of magnitude and temporal variation to respective simulated results.

This is the first attempt at an in-vitro validation of the flow model for the cerebral

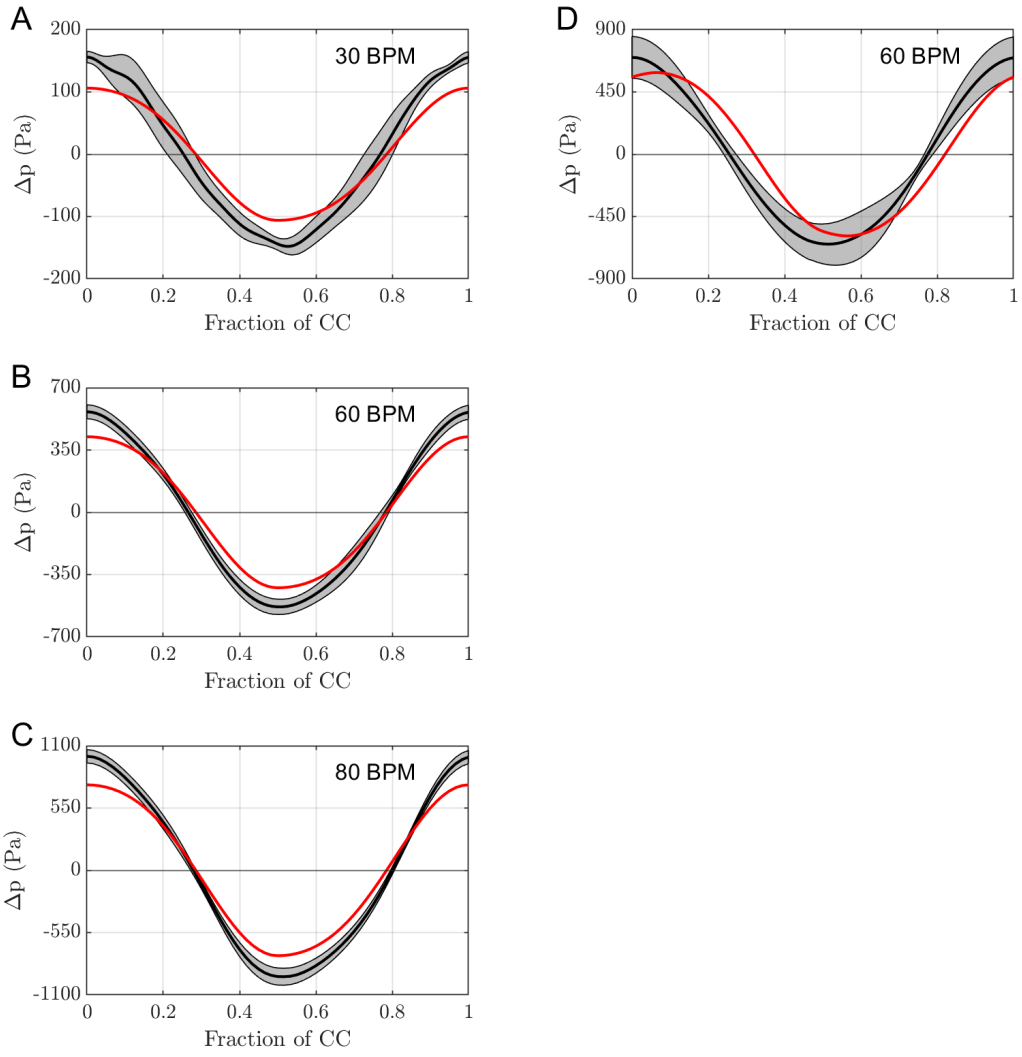

Figure 4.4. Measured (black) with error (gray) and simulated (red) pressure difference with water for 30 BPM (A), 60 BPM (B), 80 BPM (C) and 60% glycerol-water for 60 BPM (D) at 40 ml/stroke. Measured pressure signal for water is an average from about 40 cardiac cycles repeated 6 times.

aqueduct previously reported [8]. To the best of our knowledge, there exists only one study that conducts an in-vitro bench model of the aqueduct [17]. However, in that report bench experiments were conducted at the same scale and did not report the temporal variation of the differential pressure measurements. With our experimental setup, we can modify various input parameters (signal waveform, fluid viscosity, aqueduct geometry) allowing us to measure the corresponding effects on the differential pressure. Future studies should consider the systematic variation of these parameters to understand certain diseases. In addition, the use of particle image velocity (PIV) to visualize the fluid motion in experiments with anatomically-correct geometries can shed light on the flow structure at the aqueduct ends.

Acknowledgements

Chapter 4, in part is currently being prepared for submission for publication. Sincomb, Stephanie; Singh, Akansha; Coenen, Wilfried; Gutiérrez-Montes, Cándido; Martínez-Bazán, Carlos; and Sánchez, Antonio. The dissertation author was the primary author of the material.

Bibliography

[1] Rubén Martín-Láez, Hugo Caballero-Arzapalo, Luis Ángel López-Menéndez, Juan Carlos Arango-Lasprilla, and Alfonso Vázquez-Barquero. Epidemiology of idiopathic normal pressure hydrocephalus: a systematic review of the literature. *World neurosurgery*, 84(6):2002–2009, 2015.

[2] Daniel Jaraj, Katrin Rabiei, Thomas Marlow, Christer Jensen, Ingmar Skoog, and Carsten Wikkelsø. Prevalence of idiopathic normal-pressure hydrocephalus. *Neurology*, 82(16):1449–1454, 2014.

[3] Michael A Williams and Norman R Relkin. Diagnosis and management of idiopathic normal-pressure hydrocephalus. *Neurology: Clinical Practice*, 3(5):375–385, 2013.

[4] RD Adams, CM Fisher, Si Hakim, RG Ojemann, and WH Sweet. Symptomatic occult

hydrocephalus with normal cerebrospinal-fluid pressure: a treatable syndrome. *New England Journal of Medicine*, 273(3):117–126, 1965.

[5] Adam O Hebb and Michael D Cusimano. Idiopathic normal pressure hydrocephalus: a systematic review of diagnosis and outcome. *Neurosurgery*, 49(5):1166–1186, 2001.

[6] David N Levine. Intracranial pressure and ventricular expansion in hydrocephalus: have we been asking the wrong question? *Journal of the neurological sciences*, 269 (1-2):1–11, 2008.

[7] Karen Brastad Evensen and Per Kristian Eide. Measuring intracranial pressure by invasive, less invasive or non-invasive means: limitations and avenues for improvement. *Fluids and Barriers of the CNS*, 17(1):1–33, 2020.

[8] Stephanie Sincomb, Wilfried Coenen, AL Sánchez, and JC Lasheras. A model for the oscillatory flow in the cerebral aqueduct. *Journal of Fluid Mechanics*, 899, 2020.

[9] G. Bardan, F. Plouraboué, M. Zagzoule, and O. Baledent. Simple patient-based transmantle pressure and shear estimate from cine phase-contrast MRI in cerebral aqueduct. *IEEE Trans. Biomed. Eng.*, 59(10):2874–2883, 2012.

[10] P. Longatti, A. Fiorindi, P. Peruzzo, L. Basaldella, and F. M. Susin. Form follows function: estimation of CSF flow in the third ventricle–aqueduct–fourth ventricle complex modeled as a diffuser/nozzle pump. *J. Neurosurg.*, 1(aop):1–8, 2019.

[11] E. E. Jacobson, D. F. Fletcher, M. K. Morgan, and I. H. Johnston. Fluid dynamics of the cerebral aqueduct. *Pediatr. Neurosurg.*, 24(5):229–236, 1996.

[12] E. E. Jacobson, D. F. Fletcher, M. K. Morgan, and I. H. Johnston. Computer modelling of the cerebrospinal fluid flow dynamics of aqueduct stenosis. *Med. Biol. Eng. Comput.*, 37(1):59–63, 1999.

[13] L. Fin and R. Grebe. Three dimensional modeling of the cerebrospinal fluid dynamics and brain interactions in the aqueduct of sylvius. *Comput. Methods Biomech. Biomed. Engin.*, 6(3):163–170, 2003.

[14] V. Kurtcuoglu, M. Soellinger, P. Summers, K. Boomsma, D. Poulikakos, P. Boesiger, and Y. Ventikos. Computational investigation of subject-specific cerebrospinal fluid flow in the third ventricle and aqueduct of sylvius. *J. Biomech.*, 40(6):1235–1245, 2007.

[15] SJ Sincomb, Wilfried Coenen, E Criado-Hidalgo, K Wei, K King, M Borzage, V Haughton, AL Sánchez, and Juan Carlos Lasheras. Transmantle pressure computed from mr imaging measurements of aqueduct flow and dimensions. *American Journal*

of Neuroradiology, 42(10):1815–1821, 2021.

[16] Paul A. Yushkevich, Joseph Piven, Heather Cody Hazlett, Rachel Gimpel Smith, Sean Ho, James C. Gee, and Guido Gerig. User-guided 3D active contour segmentation of anatomical structures: Significantly improved efficiency and reliability. *Neuroimage*, 31(3):1116–1128, 2006.

[17] P. Holmlund, S. Qvarlander, J. Malm, and A. Eklund. Can pulsatile CSF flow across the cerebral aqueduct cause ventriculomegaly? a prospective study of patients with communicating hydrocephalus. *Fluids Barries CNS*, 16(1):1–10, 2019.

Chapter 5

A one-dimensional model for the pulsating flow of cerebrospinal fluid in the spinal canal

5.1 Introduction

The motion of CSF in the central nervous system, which has important physiological functions and plays a role in the development of different neurological diseases, has been the subject of numerous studies, as reviewed in [1]. Recent efforts include numerical simulations of the entire cranial cavity [2] and investigations of flow in the perivascular spaces of cerebral arteries [3–5] and along the cerebral aqueduct [6, 7], for example. The present chapter deals with the motion along the spinal subarachnoid space (SSAS), a slender compliant canal of length $L \simeq 60$ cm bounded internally by the pia mater surrounding the spinal cord and externally by the deformable dura membrane (see Figure 5.1(a)). The arterial blood flow in and out of the rigid cranial vault causes the intracranial pressure (ICP) to fluctuate in time following the cardiac cycle [8–10], driving the pulsatile motion of CSF along the SSAS.

Continuous ICP monitoring is key in the assessment of surgical intervention and also for guiding therapy for cases of traumatic brain injury (TBI), normal pressure hydrocephalus (NPH) and other neurointensive states. Although the mean ICP value is

often used clinically, it is of interest to also assess the pulsatile ICP variation or morphology. As shown in Figure 5.1(b), the ICP waveform generally has three peaks associated with the cardiac cycle whose amplitudes decrease in a stepwise manner in a healthy individual [11]. The waveform is altered due to the changes in intracranial volume [12], an important result in the context of disease conditions that produce an increase in mean intracranial pressure (TBI or edema formation), which can result in the waveform becoming more rounded [13], or NPH, which leads to greater fluctuation amplitudes [14]. The insertion of ICP sensors requires a burr hole made into the skull. Since the procedure has inherent risks, including hemorrhage and infection [15], there is interest in developing noninvasive techniques for ICP characterization. The approach postulated here exploits the close connection existing between the ICP waveform and the resulting CSF motion along the spinal canal. It is reasoned that detailed knowledge of the flow rate along the canal, obtained via phase-contrast magnetic resonance imaging (PC-MRI) techniques [16], can be used to infer the associated ICP waveform.

The flow in the canal fundamentally involves a fluid-structure interaction problem, which depends on detailed anatomical features of the canal determining its compliance and flow resistance [1]. As summarized in [17], most previous modelling efforts are based on numerical simulations with different levels of complexity. Analytic flow models involving a reduced number of parameters can be more useful in enabling inverse predictions of ICP from measurements of flow rates. One-dimensional models for pressure/flow wave propagation along the spinal canal have been developed in the past using a coaxial cylindrical tube configuration [18–20]. More elaborate three-dimensional flow models assuming a thin annular canal of nonuniform width are also available [21–23]. These previous efforts have assumed the canal section to be open, thereby neglecting the pressure loss introduced by spinal microstructures, effects of which have been quantified numerically in [24]. This previous analysis showed that most of the increase in pressure loss is associated with the arachnoid trabeculae [24], which are thin collagen-reinforced columns that form

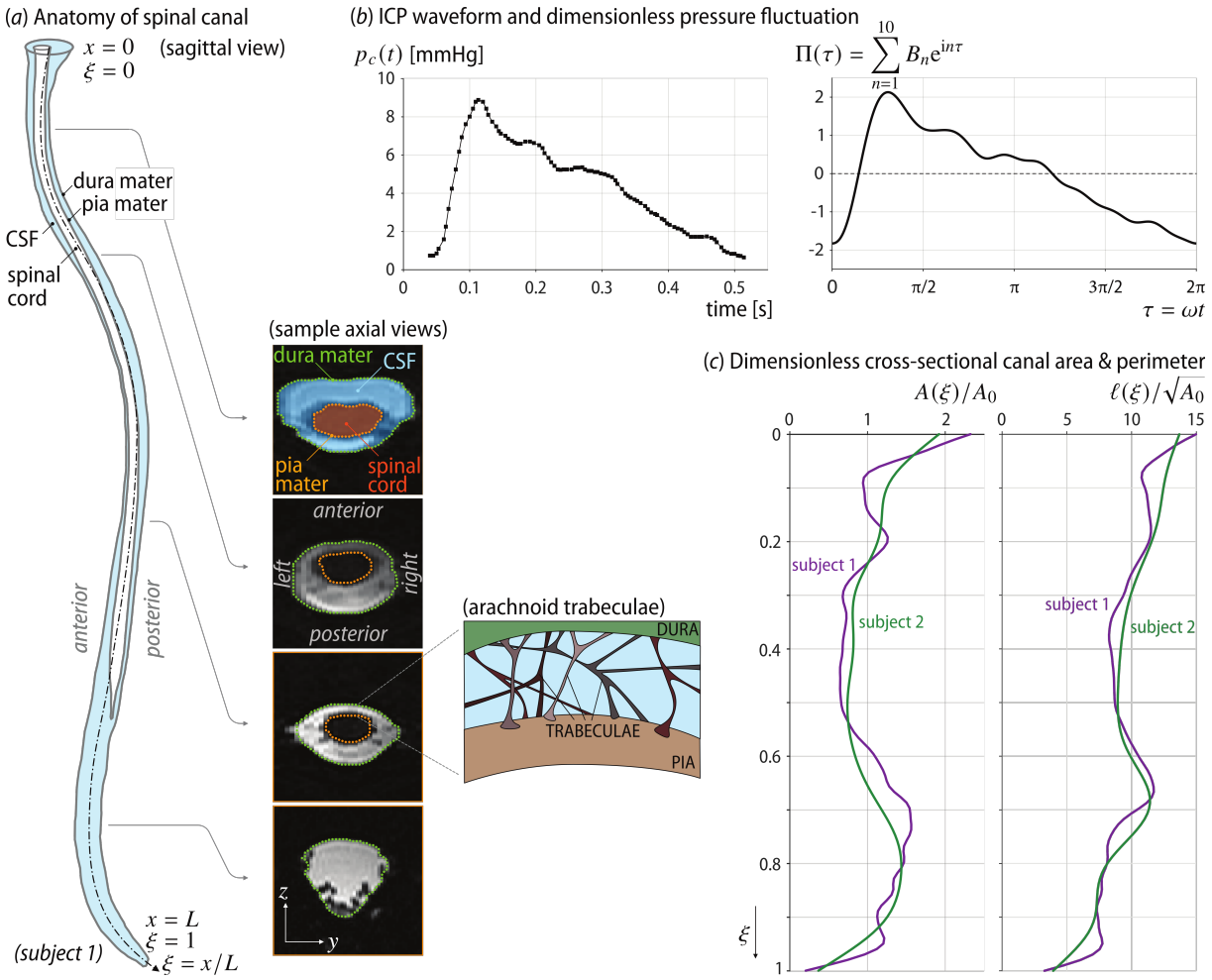

Figure 5.1. (*a*) Main anatomical features of the spinal canal for subject 1; (*b*) ICP wave form [27] CC BY 2.0 (left) and dimensionless (right); (*c*) Dimensionless canal functions for subjects 1 and 2.

a weblike structure stretching across the SSAS [25]. Following [26], our analysis will model the complex trabeculae network as a porous medium of variable permeability. For increased generality, no specific shape will be assumed for the canal cross-section, thereby generalizing our previous analyses [21–23], postulating the SSAS to be a thin annular canal surrounding the spinal cord, an assumption that necessarily fails in the sacral region, as shown in the cross-sectional views of Figure 5.1(a).

5.2 Preliminary considerations

5.2.1 The intracranial pressure

Attention will be focused on the motion induced by the cardiac cycle, associated with the periodic temporal fluctuations of the intracranial pressure $p_c(t)$ from its mean value $\langle p_c \rangle = T^{-1} \int_t^{t+T} p_c \mathrm{d}t$, where $T \simeq 1$ s is the period of the cardiac cycle. These fluctuations can in general be represented in the form $p_c(t) - \langle p_c \rangle = \Delta p \, \Pi(\omega t)$, involving the mean fluctuation amplitude $\Delta p = T^{-1} \int_t^{t+T} |p_c - \langle p_c \rangle| \mathrm{d}t$, which typically takes values on the order of $\Delta p \sim 50 - 100$ Pa, along with a dimensionless function $\Pi(\omega t)$ describing the waveform, with $\omega = 2\pi/T$ denoting the relevant angular frequency. Note that the function Π must satisfy $\int_t^{t+T} \Pi \mathrm{d}t = 0$ and $T^{-1} \int_t^{t+T} |\Pi| \mathrm{d}t = 1$, for consistency with the definition of Δp.

5.2.2 The canal geometry

In deriving a simple one-dimensional model for the flow dynamics, the spinal canal will be modeled as a tube displaying a slowly varying shape over its length $L \simeq 50 - 70$ cm. The flow is to be described in terms of curvilinear coordinates (x, y, z), with the streamwise distance x measured from the open end, connected to the cranial cavity through the foramen magnum, with the closed sacral end corresponding to $x = L$, as indicated in Figure 4.1(a). As seen in Figure 4.1(a), in the stretch of canal occupied by the spinal cord the cross-sectional shape is an annulus, bounded internally by the pia matter and externally by the dura mater. In the one-dimensional model developed below the morphology of the cross section enters only through two related quantities that vary along the spinal canal, namely, the cross-sectional area occupied by CSF at each transverse section $A(x)$ and the length of the wetted boundary $\ell(x)$, the latter including the pia matter surrounding the spinal cord. The average cross-sectional area is given by $A_o = V_{\mathrm{CSF}}/L \simeq 1.5$ cm^2, where $V_{\mathrm{CSF}} = \int_0^L A \mathrm{d}x \simeq 80$ cm^3 is the total volume of CSF in the SSAS [28]. Since

the characteristic transverse length $A_o^{1/2}$ satisfies $A_o^{1/2} \ll L$, the flow is fundamentally slender, in that fluid motion predominantly occurs in the axial direction. The streamwise velocity $u(x, y, z, t)$ driven by the streamwise pressure distribution $p(x, t)$ [21], assumed to be uniform across the canal section, as is consistent with the slender-flow approximation.

5.2.3 Governing equations

During each cardiac cycle, the ICP pulsation drives a small volume $\Delta V \sim 1$ cm^3 of CSF in and out of the spinal canal [1]. This oscillating flow is accommodated by the displacement of fat tissue and venous blood, which results in a periodic change ΔA of the local cross-sectional area A at a given location. Since the characteristic stroke volume ΔV is much smaller than the total CSF volume V_{CSF}, these temporal changes are small, i.e., $\Delta A \sim (\Delta V/V_{\text{CSF}})A_o \sim 1$ mm^2. To model these changes, we shall adopt the linear elastic model

$$\frac{\partial A}{\partial t} = \gamma \frac{\partial p}{\partial t} \tag{5.1}$$

involving a local compliance $\gamma(x)$ having dimensions of surface over pressure with mean value $\gamma_o = L^{-1} \int_0^L \gamma(x) \mathrm{d}x$.

To maximize the simplicity and facilitate comparisons with in-vivo results, CSF motion is to be characterized with use of the local volumetric flow rate $Q(x, t) = \int \int u \, \mathrm{d}y \mathrm{d}z$, obtained by integrating the streamwise velocity $u(x, y, z, t)$ across the canal section. Its streamwise variation is related with the temporal variation of the cross-sectional area through the integrated continuity equation $\partial Q/\partial x + \partial A/\partial t = 0$, which can be rewritten in the form

$$\frac{\partial Q}{\partial x} + \gamma(x) \frac{\partial p}{\partial t} = 0 \tag{5.2}$$

after substitution of (5.1). On the other hand, the axial component of the momentum balance equation can be simplified by neglecting convective acceleration, whose magnitude can be shown to be a factor $\Delta V/V_{\text{CSF}}$ smaller than that of the local acceleration [21],

along with the contribution of streamwise derivatives to the viscous force. Furthermore, following [26], the pressure loss caused by the trabeculae network is modeled using Darcy's law, yielding [29]

$$\frac{\partial u}{\partial t} = -\frac{1}{\rho}\frac{\partial p}{\partial x} + \nu\left(\frac{\partial^2 u}{\partial y^2} + \frac{\partial^2 u}{\partial z^2}\right) - \frac{\nu}{\kappa}u, \tag{5.3}$$

where $\kappa(x)$ is the SSAS permeability, whose value depends on the number and structure of the arachnoid trabeculae.

5.2.4 The inviscid wave model

It is illustrative to consider first the inviscid case $\nu = 0$, for which integration of (5.3) across the canal yields

$$\frac{\partial Q}{\partial t} + \frac{A(x)}{\rho}\frac{\partial p}{\partial x} = 0. \tag{5.4}$$

In writing the above equation, we have neglected the small temporal variation of the cross-sectional area A, as is consistent with the condition $\Delta A \ll A_o$ previously discussed. Equations (5.2) and (5.4) can be integrated with boundary conditions $p = p_c$ at $x = 0$ and $Q = 0$ at $x = L$ to determine the periodic variation of the pressure and flow rate along the canal. The wave nature of the flow can be emphasized by considering a canal with constant section $A(x) = A_o$ and constant compliance $\gamma(x) = \gamma_o$, for which (5.2) and (5.4) can be combined to give

$$\frac{\partial^2 p}{\partial t^2} = c^2\frac{\partial^2 p}{\partial x^2} \quad \text{and} \quad \frac{\partial^2 Q}{\partial t^2} = c^2\frac{\partial^2 Q}{\partial x^2}, \tag{5.5}$$

where

$$c = \left(\frac{A_o}{\rho\gamma_o}\right)^{1/2} \tag{5.6}$$

is the elastic wavespeed of the problem [30]. For a harmonic ICP fluctuation $p_c - \langle p_c \rangle = \Delta p\,(\pi/2)\,\cos(\omega t)$, the above wave equation can be solved to give

$$Q = -\frac{\pi}{2}\gamma_o L\omega\Delta p \sin(\omega t)\frac{\sin[k(1-x/L)]}{k\cos k}, \tag{5.7}$$

where

$$k = \frac{L\omega}{c} = \left(\frac{\rho\gamma_o L^2\omega^2}{A_o}\right)^{1/2} \tag{5.8}$$

is a relevant dimensionless wave number. The flow rate (5.7) oscillates in phase along the entire canal, that being a fundamental limitation of the inviscid model, which is unable to reproduce the streamwise phase lag of the flow rate that has been consistently observed in MRI measurements [10, 24, 31]. As shown below, consideration of viscous pressure losses, including those associated with the trabeculae, is needed to describe both the phase-lag and the rate of streamwise attenuation of the flow rate.

5.3 A dimensionless flow model accounting for flow resistance

To reduce the parametric dependence, it is convenient to formulate the problem in dimensionless form using ω^{-1}, L, and $A_o^{1/2}$ as scales for the time and for the longitudinal and transverse length scales, respectively. In looking for appropriate scales for Q and p, one may note from (5.2) that the characteristic value Q_c of the volume flux associated with an ICP fluctuation of magnitude Δp is $Q_c = \gamma_o\omega L\Delta p$, and from (5.4) that the corresponding streamwise variations of the pressure are of order $p - p_c \sim k^2\Delta p$, with k denoting the wave number defined in (5.8). These scales lead to the new variables

$$\tau = \omega t,\ \xi = \frac{x}{L},\ \hat{y} = \frac{y}{A_o^{1/2}},\ \hat{z} = \frac{z}{A_o^{1/2}},\ \hat{u} = \frac{u}{Q_c/A_o},\ \hat{Q} = \frac{Q}{Q_c},\ \hat{p} = \frac{p-p_c}{k^2\Delta p}. \tag{5.9}$$

Similarly, A_o and γ_o are used to define the functions $\hat{A} = A/A_o$ and $\hat{\gamma} = \gamma/\gamma_o$.

The development begins by writing the continuity equation (5.2) in the reduced form

$$\frac{\partial \hat{Q}}{\partial \xi} + \hat{\gamma}\left(\frac{\mathrm{d}\Pi}{\mathrm{d}\tau} + k^2 \frac{\partial \hat{p}}{\partial \tau}\right) = 0. \tag{5.10}$$

With the scales selected, the momentum equation (5.3) takes the dimensionless form

$$\frac{\partial \hat{u}}{\partial \tau} = -\frac{\partial \hat{p}}{\partial \xi} + \frac{1}{\alpha^2}\left(\frac{\partial^2 \hat{u}}{\partial \hat{y}^2} + \frac{\partial^2 \hat{u}}{\partial \hat{z}^2}\right) - \mathcal{R}(\xi)\hat{u}, \tag{5.11}$$

where $\alpha = (A_o\omega/\nu)^{1/2}$ is the relevant Womersley number and $\mathcal{R}(\xi) = \nu/(\kappa\omega)$ is a dimensionless resistance coefficient. The velocity must satisfy the no-slip condition $\hat{u} = 0$ on the canal boundary Σ. Integrating the above equation across the canal section yields

$$\frac{\partial \hat{Q}}{\partial \tau} + \hat{A}(\xi)\frac{\partial \hat{p}}{\partial \xi} = -\frac{1}{\alpha^2}\int_{\Sigma} \hat{\tau}_f \mathrm{d}s - \mathcal{R}(\xi)\hat{Q}, \tag{5.12}$$

where $\mathrm{d}s$ the element of arc length measured at a given section along the canal boundary Σ and $\hat{\tau}_f = \partial\hat{u}/\partial n$ is the dimensionless viscous stress at $n = 0$, where n denotes the dimensionless distance from the wall.

5.3.1 Simplifications for $\alpha \gg 1$

The solution can be simplified by taking into account that the characteristic viscous time across the canal section A_o/ν is fairly large compared with the characteristic pulsation time ω^{-1}. In the associated limit $\alpha \gg 1$, the longitudinal velocity is uniform outside a thin near-wall Stokes layer of rescaled thickness $\alpha^{-1} \ll 1$. The uniform velocity in the inviscid core varies along the canal according to $\hat{u} = \hat{Q}(\xi,\tau)/\hat{A}(\xi)$, while the accompanying pressure gradient is $\partial\hat{p}/\partial\xi = -(\partial\hat{Q}/\partial\tau + \mathcal{R}\hat{Q})/\hat{A}$. Viscous forces are important in the Stokes layer, across which the velocity $\hat{u}_\mathrm{s}$ evolves from the inviscid value $\hat{Q}/\hat{A}$ to a zero

value at $n = 0$, as described by the reduced problem

$$\frac{\partial \hat{u}_\mathrm{S}}{\partial \tau} - \frac{1}{\hat{A}(\xi)}\frac{\partial \hat{Q}}{\partial \tau} = \frac{\partial^2 \hat{u}_\mathrm{S}}{\partial \eta^2} + \mathcal{R}(\xi)\left(\frac{\hat{Q}}{\hat{A}(\xi)} - \hat{u}_\mathrm{S}\right) \begin{cases} \eta = 0: & \hat{u}_\mathrm{S} = 0 \\ \eta \to \infty: & \hat{u}_\mathrm{S} \to \hat{Q}/\hat{A} \end{cases}, \tag{5.13}$$

where $\eta = \alpha n$. The solution to (5.13) determines in particular the value of $\hat{u}'_o(\xi, \tau) = \partial \hat{u}_\mathrm{S}/\partial \eta|_{\eta=0}$, which can be used to write (5.12) in the form

$$\frac{\partial \hat{Q}}{\partial \tau} + \hat{A}(\xi)\frac{\partial \hat{p}}{\partial \xi} = -\frac{\hat{\ell}(\xi)}{\alpha}\hat{u}'_o - \mathcal{R}(\xi)\hat{Q}. \tag{5.14}$$

As expected, since at leading order in the limit $\alpha \gg 1$ the structure of the Stokes layer is identical all around the canal wall, the term $-\hat{\ell}\,\hat{u}'_o/\alpha$ representing in (5.14) the viscous force $-\int_\Sigma \hat{\tau}_f \mathrm{d}s/\alpha^2$ is linearly proportional to the dimensionless length of the wetted boundary $\hat{\ell}(\xi) = \ell/A_o^{1/2}$.

5.3.2 Solution in terms of Fourier expansions

The problem can be solved for a given general periodic function

$$\Pi(\tau) = \sum_{n=1}^{\infty} \mathrm{Re}\left(B_n \mathrm{e}^{\mathrm{i}n\tau}\right) \tag{5.15}$$

where Re indicates the real part, i is the imaginary unit, and B_n are complex constants, by introducing accompanying Fourier expansions:

$$\begin{cases} \hat{p} = \sum_{n=1}^{\infty} \mathrm{Re}\left(B_n P_n(\xi)\mathrm{e}^{\mathrm{i}n\tau}\right) \\ \hat{Q} = \sum_{n=1}^{\infty} \mathrm{Re}\left(B_n \mathrm{i}n Q_n(\xi)\mathrm{e}^{\mathrm{i}n\tau}\right) \\ \hat{u}_\mathrm{S} = \frac{1}{\hat{A}(\xi)}\sum_{n=1}^{\infty} \mathrm{Re}\left(B_n \mathrm{i}n Q_n(\xi) f_n(\eta)\mathrm{e}^{\mathrm{i}n\tau}\right) \end{cases} \tag{5.16}$$

for the pressure, volume flow rate, and Stokes-layer velocity, with $P_n(\xi)$, $Q_n(\xi)$, and $f_n(\eta)$ representing complex functions. The function $f_n = 1 - \exp\left[-(\mathrm{i}\,n + \mathcal{R})^{1/2}\eta\right]$ is obtained

from the reduced Stokes problem

$$(\mathrm{i}\,n+\mathcal{R})(f_n-1)=\frac{\mathrm{d}^2 f_n}{\mathrm{d}\eta^2}\begin{cases}\eta=0: & f_n=0\\ \eta\to\infty: & f_n\to 1\end{cases}, \tag{5.17}$$

which follows from introduction of (5.16) into (5.13), thereby yielding $\mathrm{d}f_n/\mathrm{d}\eta(0) = (\mathrm{i}\,n+\mathcal{R})^{1/2}$ and

$$\hat{u}_o'=\frac{1}{\hat{A}(\xi)}\sum_{n=1}^{\infty}\mathrm{Re}\left[B_n \mathrm{i} n Q_n(\xi)[\mathrm{i}\,n+\mathcal{R}(\xi)]^{1/2}\mathrm{e}^{\mathrm{i}n\tau}\right]. \tag{5.18}$$

Substituting (5.16) and (5.18) into (5.10) and (5.14) leads to the first-order linear ODEs

$$\frac{\mathrm{d}Q_n}{\mathrm{d}\xi}+\hat{\gamma}(\xi)\left[1+k^2P_n\right]=0 \tag{5.19}$$

$$\hat{A}(\xi)\frac{\mathrm{d}P_n}{\mathrm{d}\xi}=\left\{n^2-\mathrm{i}\,n\left[\frac{\hat{\ell}(\xi)}{\alpha\hat{A}(\xi)}[\mathrm{i}\,n+\mathcal{R}(\xi)]^{1/2}+\mathcal{R}(\xi)\right]\right\}Q_n. \tag{5.20}$$

which can be further combined to generate the boundary-value problem

$$\frac{\mathrm{d}}{\mathrm{d}\xi}\left[\frac{1}{\hat{\gamma}(\xi)}\frac{\mathrm{d}Q_n}{\mathrm{d}\xi}\right]+\frac{k^2}{\hat{A}(\xi)}\left\{n^2-\mathrm{i}\,n\left[\frac{\hat{\ell}(\xi)}{\alpha\hat{A}(\xi)}[\mathrm{i}\,n+\mathcal{R}(\xi)]^{1/2}+\mathcal{R}(\xi)\right]\right\}Q_n=0;$$
$$\frac{\mathrm{d}Q_n}{\mathrm{d}\xi}(0)+\hat{\gamma}(0)=Q_n(1)=0 \tag{5.21}$$

for $Q_n(\xi)$, with the value of $\mathrm{d}Q_n/\mathrm{d}\xi$ at $\xi=0$ following from using $P_n(0)=0$ in (5.19).

It is worth noting that the terms in the large square brackets in (5.20) represent the pressure losses associated with the Stokes layer developing on the canal boundary (the term proportional to $[\mathrm{i}\,n+\mathcal{R}]^{1/2}$) and with the trabeculae (the term proportional to $\mathcal{R}$). The two pressure losses have different phase, so that they have distinct effects on the resulting flow rate, as can be inferred from (5.21). Since the resistance exerted by the Stokes layer is inversely proportional to α, it tends to have a lesser effect, especially on

the first Fourier mode $n = 1$, for which the pressure loss associated with the trabeculae is significantly higher. Although simplified flow descriptions neglecting the presence of the Stokes layer are worth exploring in future work, for completeness the computations presented below utilize the full equation (5.21) in evaluating the flow rate.

For a canal of uniform section, uniform compliance, and uniform permeability (i.e. $\hat{A} = \hat{\gamma} = 1$, $\hat{\ell}$ =constant and $\mathcal{R}$ =constant) the solution reduces to

$$Q_n = \sin[\beta_n(1-\xi)]/(\beta_n \cos\beta_n),$$

with

$$\beta_n = kn\left\{1 + \left[\frac{1-\mathrm{i}}{(\alpha/\hat{\ell})\sqrt{2n}}\left(1 - \frac{\mathcal{R}\mathrm{i}}{n}\right)^{1/2} - \frac{\mathcal{R}\mathrm{i}}{n}\right]\right\}^{1/2}. \tag{5.22}$$

It is worth noting that the inviscid limit considered earlier corresponds to $\beta_n = kn$, the limiting form of (5.22) for $\alpha \gg 1$ and $\mathcal{R} = 0$. For the case $B_1 = \pi/2$ and $B_n = 0$ for $n > 1$, associated with the harmonic intracranial pressure $p_c = \Delta p\,(\pi/2)\cos(\omega t)$, the Fourier series for the flow rate reduces to the single term

$$\hat{Q} = \mathrm{Re}\left(\frac{\pi}{2}\mathrm{i}\frac{\sin[k(1-\xi)]}{k\cos k}\mathrm{e}^{\mathrm{i}\tau}\right) = -\frac{\pi}{2}\sin\tau\frac{\sin[k(1-\xi)]}{k\cos k}, \tag{5.23}$$

consistent with (5.7).

5.4 Illustrative sample applications

In general, numerical integration of (5.21) is needed to determine $Q_n(\xi)$. The solution depends on the anatomical characteristics of the SSAS, including its length L, average cross-sectional area A_o, and geometric functions $\hat{A} = A/A_o$ and $\hat{\ell} = \ell/A_o^{1/2}$. For a given subject, the necessary anatomical data can be determined from high-resolution MRI images, as explained for instance in [32]. The computations reported below correspond to two subjects: a healthy 27-year-old female with $L = 60$ cm, $A_o = 182$ mm^2 and

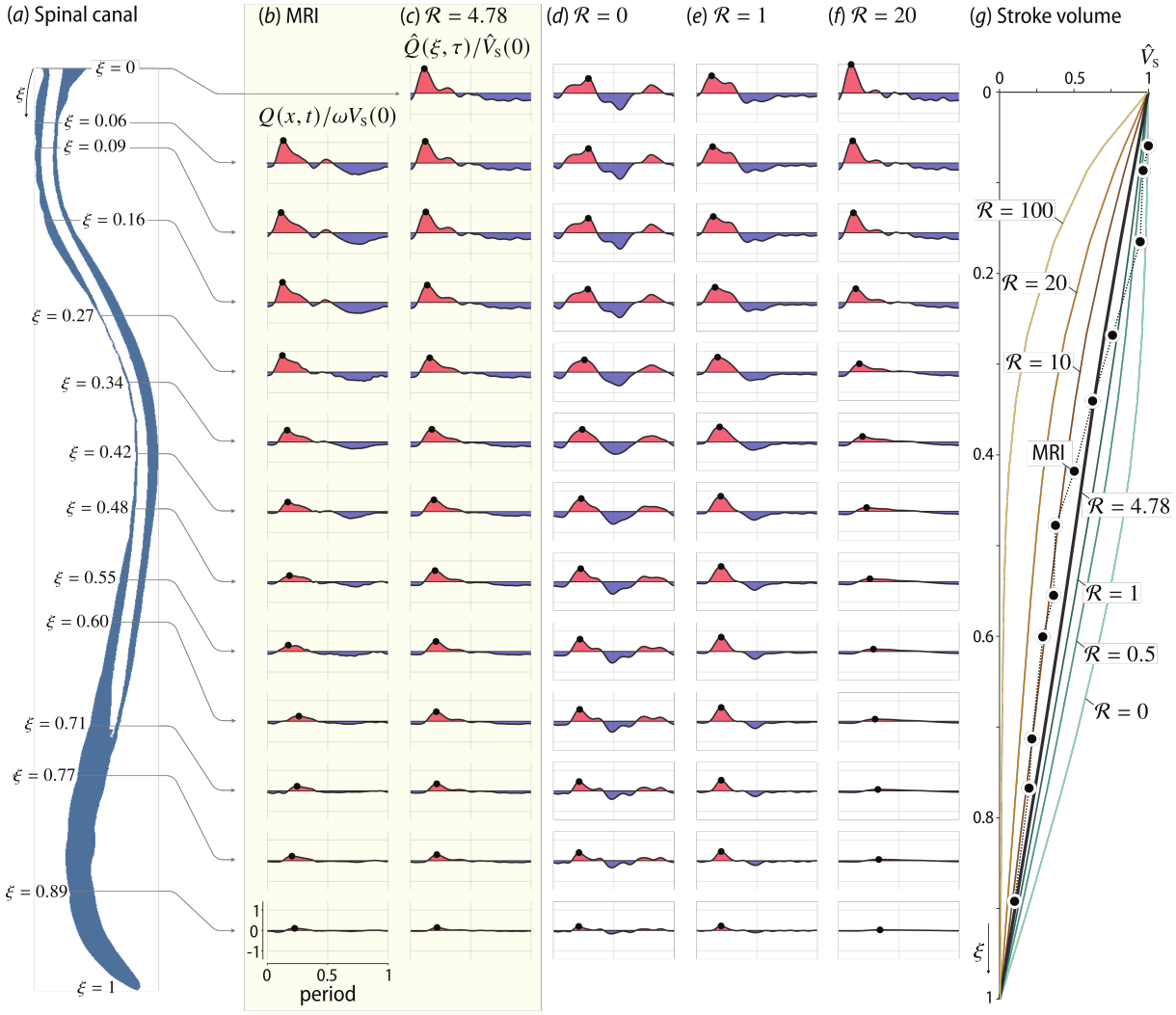

Figure 5.2. Subject 1. Selected spinal cord locations (a) with corresponding flow rate variation obtained from phase-contrast MRI measurements (b) and from model predictions for $\mathcal{R} = 4.78$ (c), $\mathcal{R} = 0$ (d), $\mathcal{R} = 1$ (e), and $\mathcal{R} = 20$ (f), with associated normalized stroke volumes shown in (g).

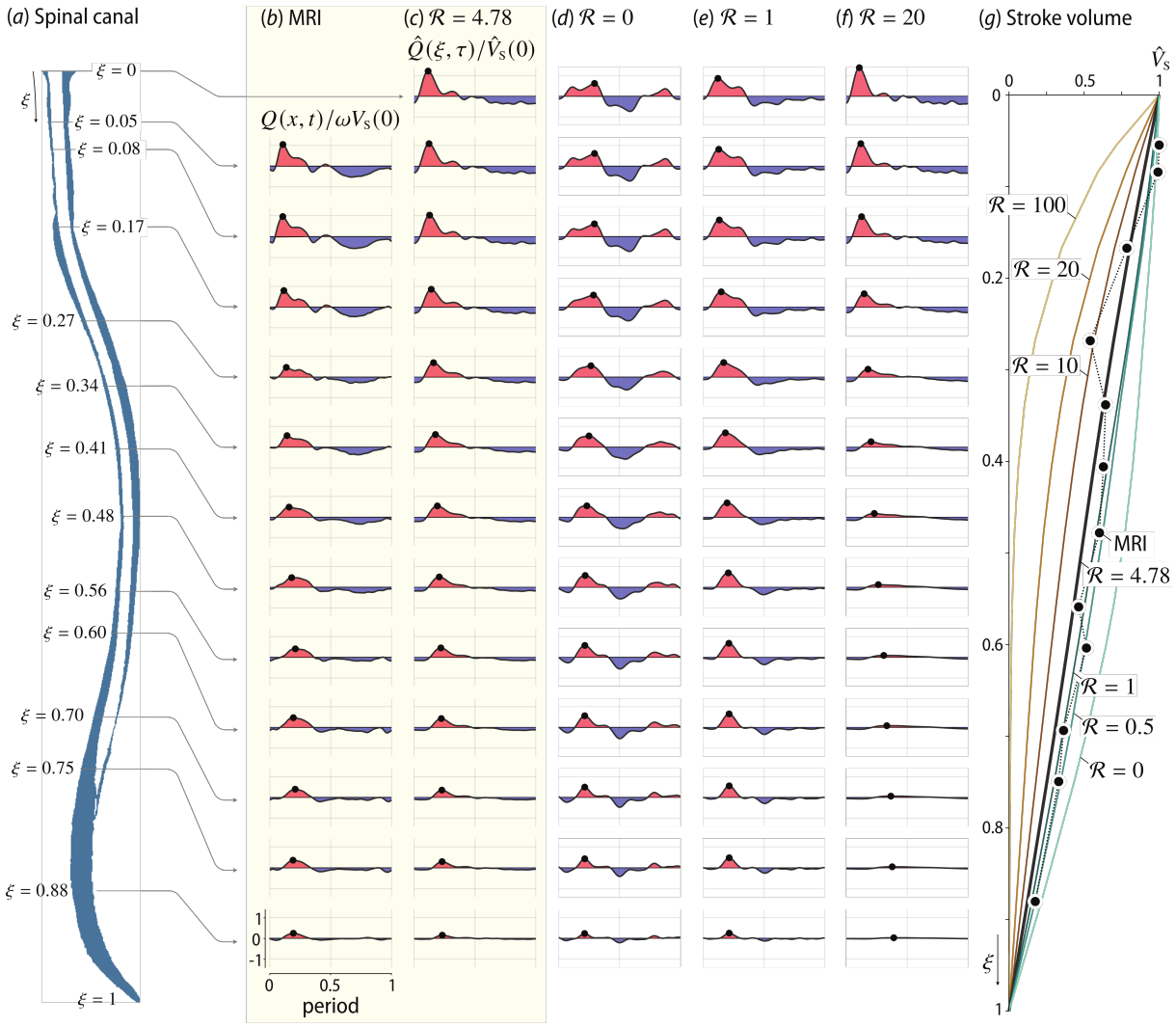

Figure 5.3. Subject 2. Selected spinal cord locations (a) with corresponding flow rate variation obtained from phase-contrast MRI measurements (b) and from model predictions for $\mathcal{R} = 4.78$ (c), $\mathcal{R} = 0$ (d), $\mathcal{R} = 1$ (e), and $\mathcal{R} = 20$ (f), with associated normalized stroke volumes shown in (g).

$\alpha = (A_o\omega/\nu)^{1/2} = 40$ (subject 1), and a healthy 39-year-old male with $L = 64$ cm, $A_o = 138$ mm^2 and $\alpha = 35$ (subject 2), both with cardiac period $T = 2\pi/\omega = 1$ s. The functions $\hat{A}(\xi)$ and $\hat{\ell}(\xi)$ shown in Figure 5.1(b) are obtained by the boundaries of the binary image stack resulting from segmentation of the high resolution MRI images.

The value of $\mathcal{R} = \nu/(\kappa\omega)$ depends on the permeability κ, which in turn is a function of the SSAS porosity ϵ and trabeculae transverse size. In the following, we shall assume that κ is uniform and adopt the approximate formula $\kappa = \pi a^2\epsilon(1-\sqrt{1-\epsilon})^2/[24(1-\epsilon)^{3/2}]$, derived by [26] for a trabeculae network comprising cylindrical posts of radius a extending normally to the arachnoid layer. For a porosity $\epsilon = 0.99$, a value estimated by [33], and a trabeculae radius $a = 15$ μm [34] this approximate formula gives $\kappa = 2.362 \times 10^{-8}$ m^2, corresponding to a dimensionless resistance factor $\mathcal{R} = 4.78$, to be used below.

Limited information is available on the spinal canal compliance γ [24]. Although departures of γ from its mean value γ_o can be expected as a result of the unequal distribution of fat tissue and epidural veins along the canal, possibly resulting in a smaller value of γ in the cervical region [31], a uniform value $\gamma = \gamma_o$ is to be employed in the following sample computation, for which $\hat{\gamma} = \gamma/\gamma_o = 1$. To estimate the average compliance γ_o, which determines from (5.8) the dimensionless wave number k, one may use (5.6) to relate γ_o with the elastic wavespeed c. Using the value $c = 4.6$ m/s reported in [35] for healthy humans, it follows from (5.6) that $\gamma_0 = 8.6 \cdot 10^{-9}$ m^2/Pa and from (5.8) that $k \simeq 0.81$ for subject 1, with corresponding values $\gamma_0 = 6.5 \cdot 10^{-9}$ m^2/Pa and $k \simeq 0.86$ for subject 2.

The modes $\hat{Q}_n$ determined from (5.21) with use made of the anatomical values reported above were used in (5.16) to compute the corresponding dimensionless flow rate $\hat{Q}$ yielding the results shown in Figures 5.2(c) and 5.3(c). The computation of $\hat{Q}$ involves ten Fourier coefficients B_n, corresponding to the function $\Pi(\tau)$ shown in Figure 5.1(b), taken as representative of a healthy state ICP waveform [36]. The results are compared in Figures 5.2 and 5.3 with flow-rate measurements acquired at twelve vertebral levels using phase-contrast MR imaging with retrospective cardiac gating in in-vivo experiments

involving the two subjects (see [32] for details of the data-acquisition process). To establish a quantitatively consistent comparison, the results are presented in normalized form. Thus, the stroke volume $V_{\mathrm{S}}(\xi) = \frac{1}{2}\int_t^{t+T} |Q|\mathrm{d}t$ measured via MRI is scaled with its entrance value (i.e. $V_{\mathrm{S}}(0) = 0.7$ cm^3 for subject 1 and $V_{\mathrm{S}}(0) = 0.6$ cm^3 for subject 2), while the model prediction $\hat{V}_{\mathrm{S}}(\xi) = \frac{1}{2}\int_\tau^{\tau+2\pi} |\hat{Q}|\mathrm{d}\tau$ is correspondingly scaled with $\hat{V}_{\mathrm{S}}(0)$, with $\hat{V}_{\mathrm{S}}(0) = 1.9$ for subject 1 and $\hat{V}_{\mathrm{S}}(0) = 1.8$ for subject 2. Similarly, the PC-MRI flow-rate measurements are scaled with its characteristic value $\omega V_{\mathrm{S}}(0)$ while the predicted flow rate $\hat{Q}$ is scaled with $\hat{V}_{\mathrm{S}}(0)$.

With the uniform values $\hat{\gamma} = 1$, and $\mathcal{R} = 4.78$ selected in the computations, the comparisons in Figures 5.2 and 5.3 indicate that the model is able to describe reasonably well the main features of the pulsating flow rate, including its particular shape and the phase lag of its peak value. In addition, the streamwise decay of the stroke volume (Figures 5.2(g) and 5.3(g)), a metric often used in the medical community to characterize CSF flow, is seen to agree well with the corresponding values computed from the MRI data, with root-mean-square differences between model and MRI remaining below 0.09 for both subjects. As a further consistency check, one may use the measured value of $V_{\mathrm{S}}(0)$ along with the accompanying dimensionless prediction $\hat{V}_{\mathrm{S}}(0)$ to obtain from the definition $V_{\mathrm{S}}(0) = \gamma_o L \Delta p \hat{V}_{\mathrm{S}}(0)$ an estimate for the mean fluctuation amplitude Δp. The value obtained, $\Delta p = 73$ Pa for subject 1 and $\Delta p = 80$ Pa for subject 2, corresponding to a peak-to-peak value of about 200 Pa, is well within the range of values reported in the literature [37], thereby providing additional confidence in the model.

To investigate the sensitivity of the model predictions to changes in trabeculae resistance, results for varying $\mathcal{R}$ are also included in Figures 5.2 and 5.3. In the absence of trabeculae, i.e. for $\mathcal{R} = 0$, both the rate at which the flow-rate fluctuation decays along the canal and the general flow-rate waveform, including the associated phase lag, are in poor agreement with the MRI measurements. Consequently, for $\mathcal{R} = 0$ the modeled streamwise decay of stroke volume, shown in Figures 5.2(g) and 5.3(g), is also seen to

strongly overpredict the amount of CSF flow in the thoracic and lumbar regions compared to the MRI measurements. These quantitative findings emphasize the important effects of trabeculae, previously pointed out by [24]. As can be seen in Figures 5.2 and 5.3, the results are not very sensitive to the specific choice of $\mathcal{R}$, provided that an order-unity value is selected. Nevertheless, the computations obtained with $\mathcal{R} = 4.78$, the value determined using the permeability and other anatomical features taken from the literature [26, 33, 34], appear to give better overall agreement with the MRI measurements, providing the optimal amount of attenuation all along the canal.

5.5 Concluding remarks

The temporal and spatial variation of the flow rate predicted by the one-dimensional model developed here supplemented with a presumed ICP waveform has been shown to predict the main features revealed in in-vivo experiments. Utilization of the model in future efforts to develop non-invasive measurements of ICP requires the solution of the inverse problem, i.e., the computation of the ICP fluctuation from the PC-MRI flow measurements. Given the uncertainty regarding the canal compliance and the trabeculae-network properties, it is unclear whether conventional parameter-fitting approaches will be successful in these future developments or whether more elaborate optimization algorithms, possibly based on machine-learning techniques, will be needed. In improving the model, these future efforts should also account for localized pressure losses associated with the presence of additional spinal microstructures, such as nerve roots and ligaments.

Acknowledgements

Chapter 5, in full with slight modifications, is a reprint of the material as it appears in the Journal of Fluid Mechanics, 2022. Sincomb, Stephanie; Coenen, Wilfried; Gutiérrez-Montes, Cándido; Martínez-Bazán, Carlos; Haughton, Victor and Sánchez, Antonio. The

dissertation author was the primary author of this paper.

Bibliography

[1] A. A. Linninger, K. Tangen, C.-Y. Hsu, and D. Frim. Cerebrospinal fluid mechanics and its coupling to cerebrovascular dynamics. *Annu. Rev. Fluid Mech.*, 48:219–257, 2016.

[2] Seifollah Gholampour and Nasser Fatouraee. Boundary conditions investigation to improve computer simulation of cerebrospinal fluid dynamics in hydrocephalus patients. *Commun. Biol.*, 4(1):1–15, 2021.

[3] John H Thomas. Fluid dynamics of cerebrospinal fluid flow in perivascular spaces. *J. R. Soc. Interface*, 16(159):20190572, 2019.

[4] J Brennen Carr, John H Thomas, Jia Liu, and Jessica K Shang. Peristaltic pumping in thin non-axisymmetric annular tubes. *J. Fluid Mech.*, 917, 2021.

[5] W Coenen, X Zhang, and AL Sánchez. Lubrication analysis of peristaltic motion in non-axisymmetric annular tubes. *J. Fluid Mech.*, 921, 2021.

[6] Stephanie Sincomb, Wilfried Coenen, AL Sánchez, and JC Lasheras. A model for the oscillatory flow in the cerebral aqueduct. *J. Fluid Mech.*, 899, 2020.

[7] SJ Sincomb, W Coenen, E Criado-Hidalgo, K Wei, K King, M Borzage, V Haughton, AL Sánchez, and JC Lasheras. Transmantle pressure computed from mr imaging measurements of aqueduct flow and dimensions. *AJNR Am. J. Neuroradiol.*, 42(10): 1815–1821, 2021.

[8] GH Du Boulay. Pulsatile movements in the csf pathways. *Br. J. Radiol.*, 39(460): 255–262, 1966.

[9] RA Bhadelia, AR Bogdan, RF Kaplan, and SM Wolpert. Cerebrospinal fluid pulsation amplitude and its quantitative relationship to cerebral blood flow pulsations: a phase-contrast mr flow imaging study. *Neuroradiol.*, 39(4):258–264, 1997.

[10] Mark E Wagshul, John J Chen, Michael R Egnor, Erin J McCormack, and Patricia E Roche. Amplitude and phase of cerebrospinal fluid pulsations: experimental studies and review of the literature. *J. Neurosurg.*, 104(5):810–819, 2006.

[11] Vineeta Singh and Roger Cheng. Neurovascular physiology and neurocritical care. In *Handbook of Clinical Neurology*, volume 176, pages 71–80. Elsevier, 2021.

[12] Mårten Unnerbäck, Johnny T Ottesen, and Peter Reinstrup. ICP curve morphology and intracranial flow-volume changes: a simultaneous icp and cine phase contrast mri study in humans. *Acta Neurochir.*, 160(2):219–224, 2018.

[13] Tim Ellis, James McNames, and Mateo Aboy. Pulse morphology visualization and analysis with applications in cardiovascular pressure signals. *IEEE Trans. Biomed.*, 54(9):1552–1559, 2007.

[14] Per Kristian Eide and Wilhelm Sorteberg. Outcome of surgery for idiopathic normal pressure hydrocephalus: role of preoperative static and pulsatile intracranial pressure. *World Neurosurg.*, 86:186–193, 2016.

[15] Karen Brastad Evensen and Per Kristian Eide. Measuring intracranial pressure by invasive, less invasive or non-invasive means: limitations and avenues for improvement. *Fluids Barriers CNS*, 17(1):1–33, 2020.

[16] D. A. Feinberg and A. S. Mark. Human brain motion and cerebrospinal fluid circulation demonstrated with mr velocity imaging. *Radiology*, 163(3):793–799, 1987.

[17] Mohammadreza Khani, Lucas R Sass, Tao Xing, M Keith Sharp, Olivier Balédent, and Bryn A Martin. Anthropomorphic model of intrathecal cerebrospinal fluid dynamics within the spinal subarachnoid space: spinal cord nerve roots increase steady-streaming. *J. Biomech. Eng.*, 140(8), 2018.

[18] K Berkouk, PW Carpenter, and AD Lucey. Pressure wave propagation in fluid-filled co-axial elastic tubes part 1: basic theory. *J. Biomech. Eng.*, 125(6):852–856, 2003.

[19] PW Carpenter, K Berkouk, and AD Lucey. Pressure wave propagation in fluid-filled co-axial elastic tubes part 2: mechanisms for the pathogenesis of syringomyelia. *J. Biomech. Eng.*, 125(6):857–863, 2003.

[20] Srdjan Cirovic and Minsuok Kim. A one-dimensional model of the spinal cerebrospinal-fluid compartment. *J. Biomech. Eng.*, 134(2):021005, 2012.

[21] A. L. Sánchez, C. Martínez-Bazan, C. Gutiérrez-Montes, E. Criado-Hidalgo, G. Pawlak, W. Bradley, V. Haughton, and J. C. Lasheras. On the bulk motion of the cerebrospinal fluid in the spinal canal. *J. Fluid Mech.*, 841:203–227, 2018.

[22] J. J. Lawrence, W. Coenen, A. L. Sánchez, G. Pawlak, C. Martínez-Bazán, V. Haughton, and J. C. Lasheras. On the dispersion of a drug delivered intrathecally in the spinal canal. *J. Fluid Mech.*, 861:679–720, 2019.

[23] C Gutiérrez-Montes, W Coenen, JJ Lawrence, C Martínez-Bazán, AL Sánchez, and JC Lasheras. Modelling and direct numerical simulation of flow and solute dispersion

in the spinal subarachnoid space. *Appl. Math. Model.*, 94:516–533, 2021.

[24] Kevin M Tangen, Ying Hsu, David C Zhu, and Andreas A Linninger. Cns wide simulation of flow resistance and drug transport due to spinal microanatomy. *J. Biomech.*, 48(10):2144–2154, 2015.

[25] Martin M Mortazavi, Syed A Quadri, Muhammad A Khan, Aaron Gustin, Sajid S Suriya, Tania Hassanzadeh, Kian M Fahimdanesh, Farzad H Adl, Salman A Fard, M Asif Taqi, and I. Armstrong. Subarachnoid trabeculae: a comprehensive review of their embryology, histology, morphology, and surgical significance. *World Neurosurg.*, 111:279–290, 2018.

[26] S. Gupta, M. Soellinger, P. Boesiger, D. Poulikakos, and V. Kurtcuoglu. Three-dimensional computational modeling of subject-specific cerebrospinal fluid flow in the subarachnoid space. *J. Biomech. Eng.*, 131(2):021010, 2009.

[27] Mark E Wagshul, Per K Eide, and Joseph R Madsen. The pulsating brain: a review of experimental and clinical studies of intracranial pulsatility. *Fluids Barriers CNS*, 8 (1):1–23, 2011.

[28] M Edsbagge, G Starck, H Zetterberg, D Ziegelitz, and C Wikkelso. Spinal cerebrospinal fluid volume in healthy elderly individuals. *Clin. Anat.*, 24(6):733–740, 2011.

[29] Vartan Kurtcuoglu, Kartik Jain, and Bryn A Martin. Modelling of cerebrospinal fluid flow by computational fluid dynamics. In *Biomechanics of the Brain*, pages 215–241. Springer, 2019.

[30] James B Grotberg and Oliver E Jensen. Biofluid mechanics in flexible tubes. *Annu. Rev. Fluid Mech.*, 36:121–147, 2004.

[31] N Yallapragada and N Alperin. Characterization of spinal canal hydrodynamics and compliance using bond graph technique and csf flow measurements by mri. *Proc. Int. Soc. Magn. Resonan. Med.*, 11:2658, 2004.

[32] W. Coenen, C. Gutiérrez-Montes, S. Sincomb, E. Criado-Hidalgo, K. Wei, K. King, V. Haughton, C. Martínez-Bazán, A. L. Sánchez, and J. C. Lasheras. Subject-specific studies of CSF bulk flow patterns in the spinal canal: Implications for the dispersion of solute particles in intrathecal drug delivery. *Am. J. Neuroradiol.*, 40:1242–1249, 2019.

[33] Yukio Tada and Tatsuya Nagashima. Modeling and simulation of brain lesions by the finite-element method. *IEEE Eng. Med. Biol. Mag.*, 13(4):497–503, 1994.

[34] H. W. Stockman. Effect of anatomical fine structure on the flow of cerebrospinal fluid

in the spinal subarachnoid space. *J. Biomech. Eng.*, 128(1):106–114, 2006.

[35] Wojciech Kalata, Bryn A Martin, John N Oshinski, Michael Jerosch-Herold, Thomas J Royston, and Francis Loth. Mr measurement of cerebrospinal fluid velocity wave speed in the spinal canal. *IEEE Trans. Biomed.*, 56(6):1765–1768, 2009.

[36] Antonio Di Ieva, Erika M Schmitz, and Michael D Cusimano. Analysis of intracranial pressure: past, present, and future. *Neuroscientist*, 19(6):592–603, 2013.

[37] PK Eide and A Brean. Intracranial pulse pressure amplitude levels determined during preoperative assessment of subjects with possible idiopathic normal pressure hydrocephalus. *Acta Neurochir.*, 148(11):1151–1156, 2006.

Chapter 6

Additional results concerning the spinal canal

6.1 Introduction

The use of the spinal canal model in Chapter 5 has been limited to the analysis of the dependence of the results on the trabeculae resistance. In this chapter, we present additional results. We first demonstrate the effect of the ICP morphology on the resulting flow rate for the same subjects. This sensitivity analysis sheds light on the potential use of the model in combination with MR flow-rate measurements as a diagnostic tool to predict altered ICP signals corresponding to diseased states such as normal pressure hydrocephalus (NPH) patients. We then present a plausible method for in-vivo validation of our model using the lumbar pressure in lieu of the ICP.

6.2 Effect of ICP signal morphology

Our results from Chapter 5 used a normal ICP waveform, which exhibits three distinct peaks referred to as percussion, tidal and dicrotic [1]. Characterizing the ICP waveform morphology has been of interest clinically [2–4]. It is generally accepted that the ICP morphology can change as a result of diseases that affect the mean ICP. For example, it has been shown that for increased mean ICP the waveform becomes more round, as

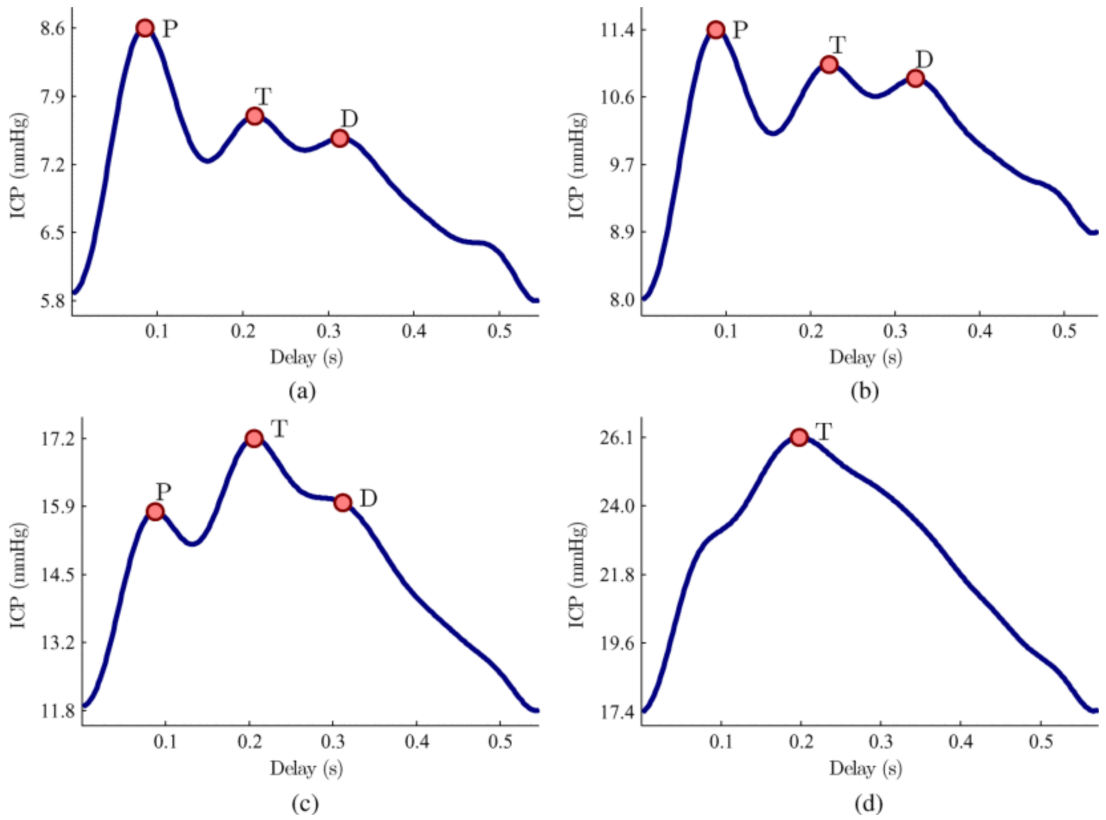

Figure 6.1. Example of the ICP pulse morphology becoming more rounded, or sinusoidal, as the mean ICP increases. Peaks labeled are the percussion (P), tidal (T), and dichrotic (D). (a) Mean ICP=7.12 mmHg, (b) Mean ICP=10.1 mmHg , (c) Mean ICP=14.7 mmHg , and (d) Mean ICP=22.5 mmHg. © 2007 IEEE [5]

shown in Figure 6.1 [5]. Using our model, it is of interest to assess the extent to which the ICP morphology has visible effects on the flow rates along the canal.

Two altered ICP waveforms were used in conducting flow-rate evaluations for the two subjects investigated in Chapter 5. The first altered waveform, shown in Figure 6.2, was simply the original signal, but low-pass filtered, which smoothed the signal. The second waveform comes from Figure 6.1(d), which shows a complete roundness to the ICP. The same subject parameters were used as reported previously, i.e. a healthy 27-year-old female with $L = 60$ cm, $A_o = 182$ mm^2 and $\alpha = (A_o\omega/\nu)^{1/2} = 40$ (subject 1), and a healthy 39-year-old male with $L = 64$ cm, $A_o = 138$ mm^2 and $\alpha = 35$ (subject 2), both with cardiac period $T = 2\pi/\omega = 1$ s. The results with both ICP variations are shown in

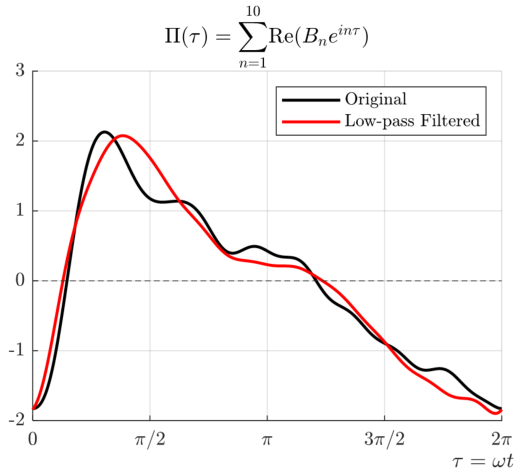

Figure 6.2. Original ICP signal used for results in Chapter 5 (black) and the low-pass filtered signal with a cutoff frequency of 2 Hz (red).

Figures 6.3 and 6.4, respectively.

The sensitivity of the flow rate to the ICP morphology is visible with the one-dimensional model. Once characteristic ICP peaks were smoothed or completely rounded, the resulting flow rates followed similar behavior. In fact, in the case of the rounded ICP with the tidal peak the highest (Figure 6.1(d)), the resulting flow rate also showed the second peak as dominant. This is consistent with a report that made simultaneous measurements of the ICP and the flow rate at the foramen magnum shown in their reported Figure 1, where the highest peak of the ICP signal, which is the percussion, coincides with the peak of the flow rate [6].

6.3 Lumbar pressure

There are inherent challenges with finding subjects undergoing continuous ICP monitoring to validate our model. This is because, in addition to the invasive procedure, the subject would have to willingly undergo additional MRI imaging. However, because the spinal compartment is closed, lumbar pressure measurement would be a suitable replacement for the ICP signal.

Lumbar pressure has been examined in previous studies as an alternative to the

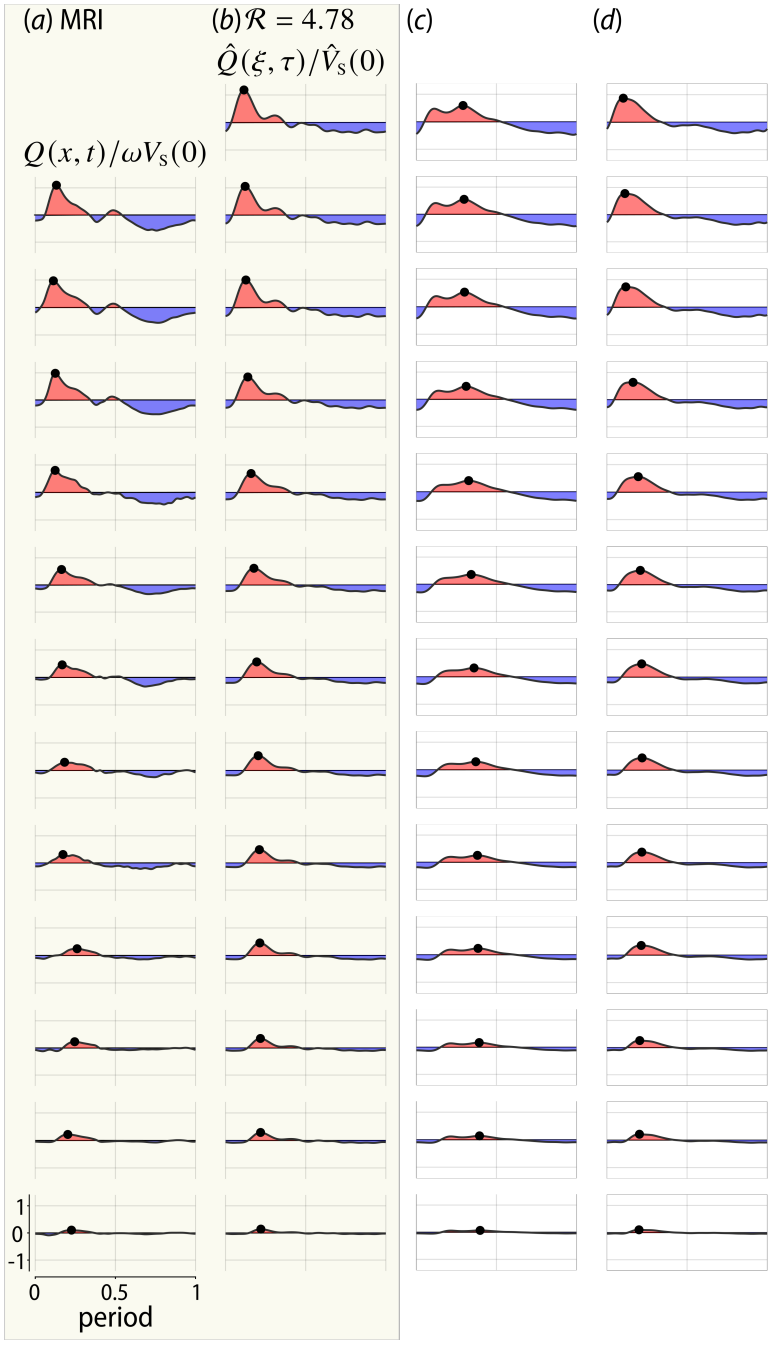

Figure 6.3. MRI flow rate measurements along the canal (a) and model results with normal ICP signal (b) rounded ICP with tidal peak as highest (c) and smoothed signal with percussion as highest (d) for subject 1.

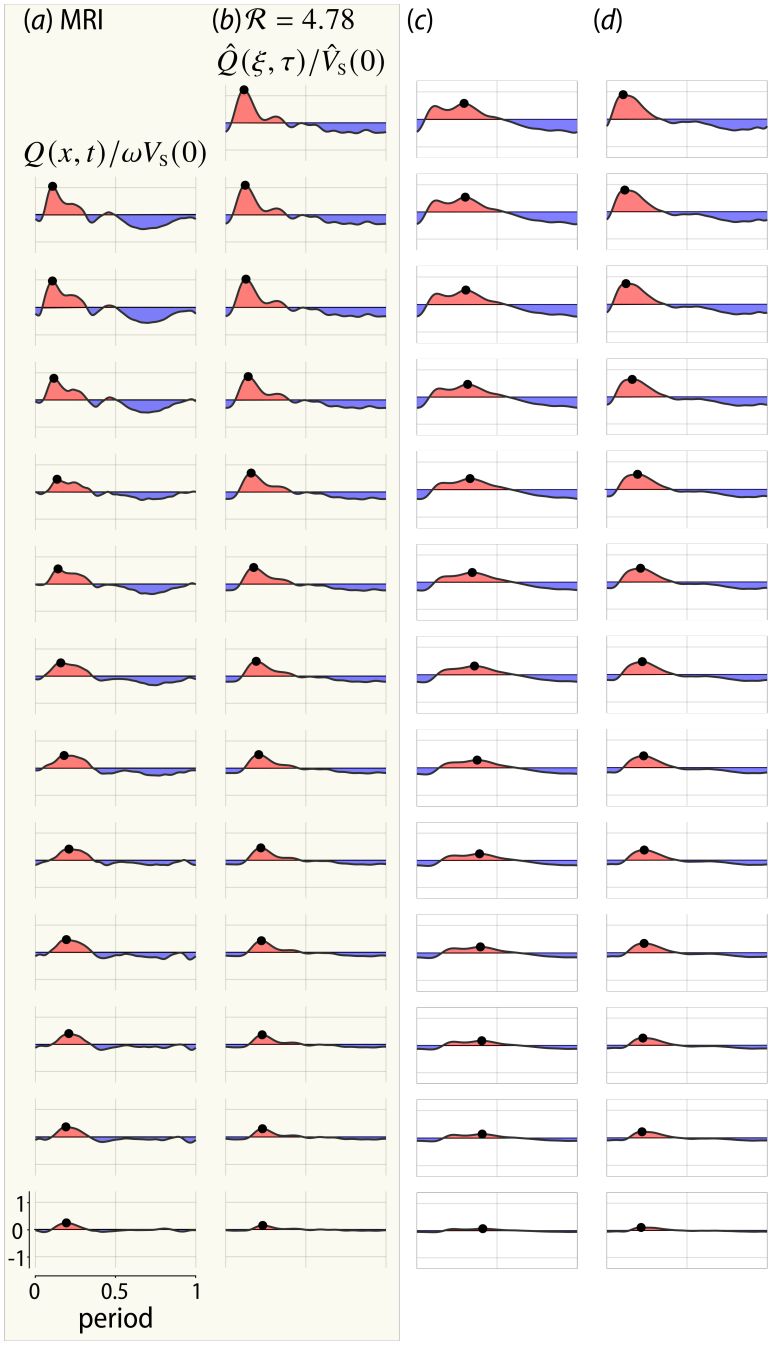

Figure 6.4. MRI flow rate measurements along the canal (a) and model results with normal ICP signal (b) rounded ICP with tidal peak as highest (c) and smoothed signal with percussion as highest (d) for subject 2.

ICP. In fact, one such study asked specifically if the ICP wave amplitudes can be measured through a lumbar puncture and found that it does [7]. As anticipated, there was a delay and decay in the amplitude of the signal. These trends are also observed in another study comparing the ICP and lumbar pressures in patients with Chiari malformation type 1 [8]. For illustrative purposes, the figure showing the main results of this previous in-vivo study is reproduced here in Figure 6.5. It is of interest to investigate the ability of the model to reproduce these previously observed trends.

The pressure at any section along the canal can be expressed in the form

$$\frac{p - \langle p_c \rangle}{\Delta p} = \Pi(\tau) + k^2 \tilde{p}(\xi, \tau) \tag{6.1}$$

thereby yielding

$$\frac{p - \langle p_c \rangle}{\Delta p} = \sum_{n=1}^{\infty} \mathrm{Re}\{B_n \mathrm{e}^{\mathrm{i}n\tau}[1 + k^2 P_n(\xi)]\}. \tag{6.2}$$

upon substitution of the Fourier series expansions given in (5.15) and (5.16). Using (5.19) finally gives

$$\frac{p - \langle p_c \rangle}{\Delta p} = -\sum_{n=1}^{\infty} \mathrm{Re}\left\{ B_n \mathrm{e}^{\mathrm{i}n\tau} \frac{1}{\tilde{\gamma}(\xi)} \frac{\mathrm{d}Q_n}{\mathrm{d}\xi}(\xi) \right\}, \tag{6.3}$$

which allows us to compute the temporal variation of the pressure at any given location ξ in terms of the local values of the functions $\tilde{\gamma}$ and $\mathrm{d}Q_n/\mathrm{d}\xi$. Results corresponding the original ICP signal for subject 1 assuming $\tilde{\gamma} = 1$ are shown in Figure 6.6, with the pressure evaluated at $\xi = 0.89$, selected as representative of the lumbar region. The average of the lumbar pressure increased slightly from the original ICP, as shown in the inset of the figure.

As can be seen in Figure 6.6, using our model to compute the lumbar pressure associated with a healthy ICP results in a signal that closely resembles that shown in Figure 6.5b (bottom), in that the predicted wave exhibits both amplitude decay and phase lag. The previous in-vivo study [8] reports a static pressure gradient, mean ICP –

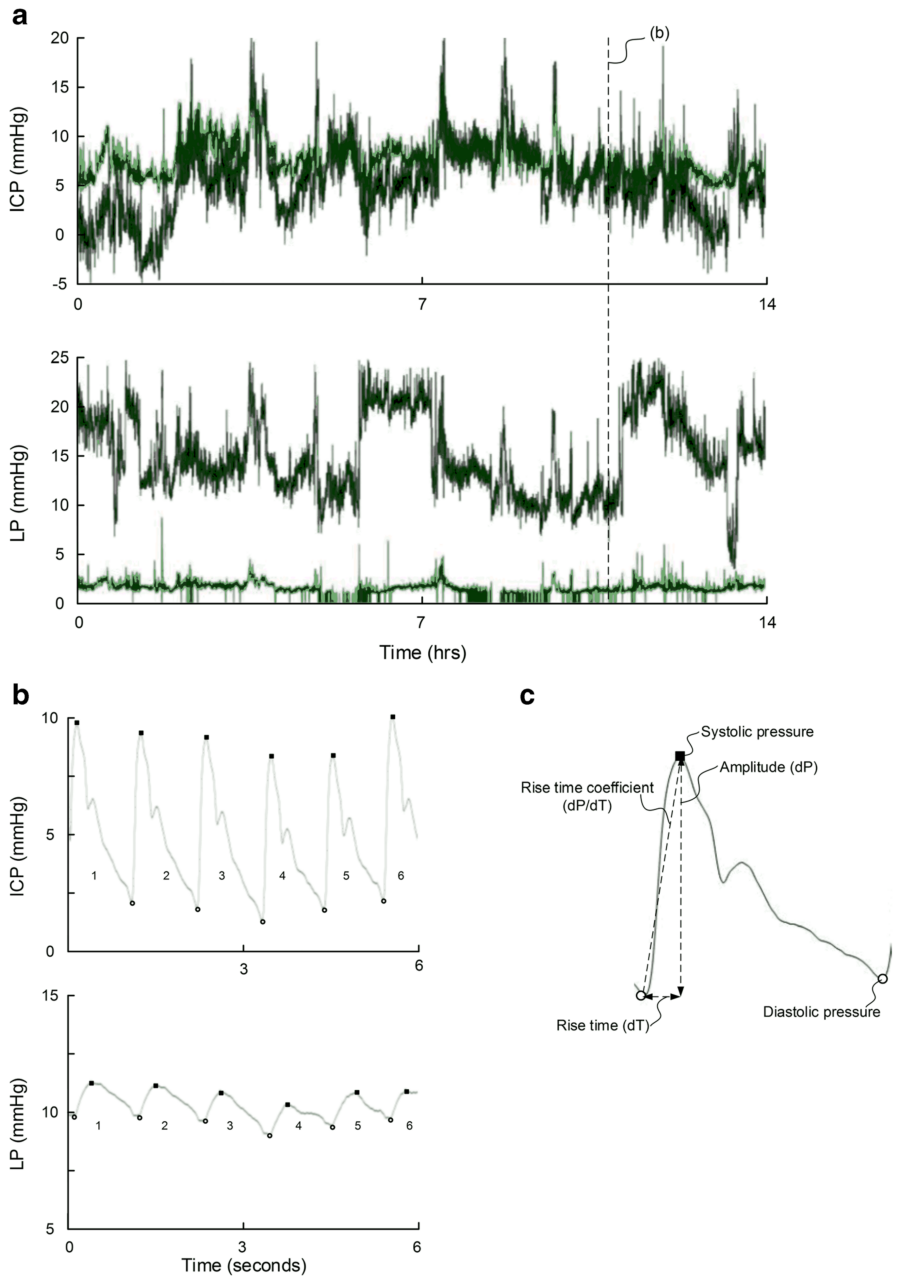

Figure 6.5. Figure a shows the trend plots for the ICP (upper plots) and LP (lower plots) signals, respectively. In b, one 6-s time window showing the ICP (upper) and LP (lower) signals with six cardiac-induced ICP waves is presented. The ICP wave attributes that were determined automatically are shown in c. Each wave was characterised by the amplitude (dP), rise time (dT) and rise time coefficient (dP/dT). Reprinted by permission from Springer Nature: Springer Nature, Acta Neurochirurgica, [8], Copyright 2015

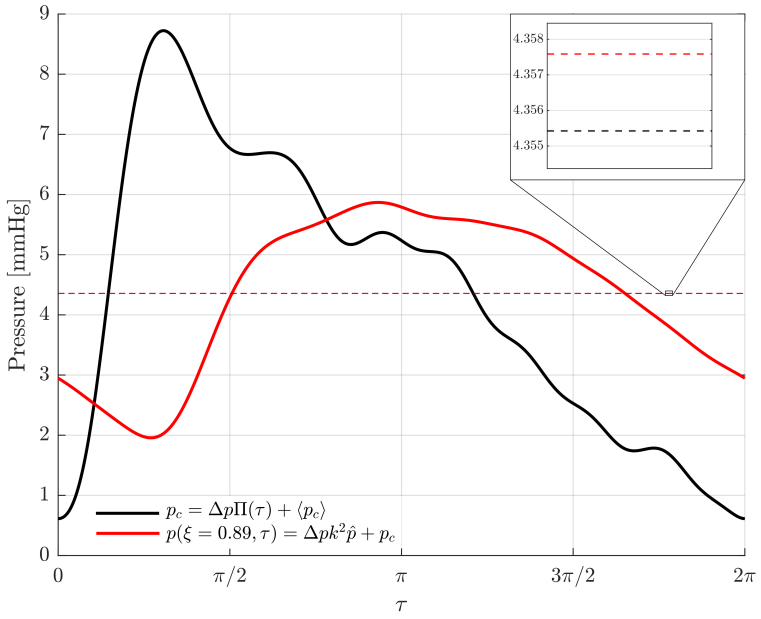

Figure 6.6. Lumbar pressure (red) computed from original ICP signal (black). Averages for lumbar and ICP are given by the red and black lines, respectively. Difference in value shown in inset.

mean lumbar pressure, ranging from -27.7 to 3.5 mmHg. The static pressure tended to be higher in the lumbar region, which is consistent with our computation. It should be noted, however, that these previous in-vivo measurements are for patients with Chiari malformation type 1. A similar study investigating the ICP and lumbar pressures in patients with NPH [7] also found a phase lag and decrease in the amplitudes of the signals. Although these studies included diseased subjects, it should be noted that in all cases the mean ICP values are within the normal range (i.e. $\leq$15-20 mmHg) [9] emphasizing the need to study the pulsatile component of the ICP.

6.4 Concluding remarks

In summary, in this brief qualitative assessment, our model demonstrated the morphology of the ICP correlates to the resulting flow rate waveform. In addition, the lumbar pressure signal predicted with the model is consistent with reported in-vivo

measurements. This latter finding suggests that measurements of the flow rate and lumbar pressure may be used as an alternative solution to the ICP to validate our model.

Acknowledgements

Chapter 6, in part is currently being prepared for submission for publication. Sincomb, Stephanie; Coenen, Wilfried; Gutiérrez-Montes, Cándido; Martínez-Bazán, Carlos; and Sánchez, Antonio. The dissertation author was the primary author of the material.

Bibliography

[1] Antonio Di Ieva, Erika M Schmitz, and Michael D Cusimano. Analysis of intracranial pressure: past, present, and future. *Neuroscientist*, 19(6):592–603, 2013.

[2] Erico R Cardoso, Jack O Rowan, and Sam Galbraith. Analysis of the cerebrospinal fluid pulse wave in intracranial pressure. *Journal of neurosurgery*, 59(5):817–821, 1983.

[3] D John Doyle and Patrick WS Mark. Analysis of intracranial pressure. *Journal of clinical monitoring*, 8(1):81–90, 1992.

[4] PK Eide and A Brean. Intracranial pulse pressure amplitude levels determined during preoperative assessment of subjects with possible idiopathic normal pressure hydrocephalus. *Acta Neurochir.*, 148(11):1151–1156, 2006.

[5] Tim Ellis, James McNames, and Mateo Aboy. Pulse morphology visualization and analysis with applications in cardiovascular pressure signals. *IEEE Trans. Biomed.*, 54 (9):1552–1559, 2007.

[6] Mårten Unnerbäck, Johnny T Ottesen, and Peter Reinstrup. ICP curve morphology and intracranial flow-volume changes: a simultaneous icp and cine phase contrast mri study in humans. *Acta Neurochir.*, 160(2):219–224, 2018.

[7] Anders Behrens, Niklas Lenfeldt, Sara Qvarlander, L-O Koskinen, Jan Malm, and Anders Eklund. Are intracranial pressure wave amplitudes measurable through lumbar puncture? *Acta Neurologica Scandinavica*, 127(4):233–241, 2013.

[8] Radek Frič and Per Kristian Eide. Comparison of pulsatile and static pressures within

the intracranial and lumbar compartments in patients with chiari malformation type 1: a prospective observational study. *Acta neurochirurgica*, 157(8):1411–1423, 2015.

[9] Marek Czosnyka and John D Pickard. Monitoring and interpretation of intracranial pressure. *Journal of Neurology, Neurosurgery & Psychiatry*, 75(6):813–821, 2004.

Chapter 7

Conclusions

The aim of this dissertation was to develop simplified flow descriptions that can be combined with phase-contrast magnetic resonance imaging for implementation in clinical studies. Separate models have been developed for the pulsatile flow of CSF in the cerebral aqueduct and the spinal canal. Both models allow clinicians to obtain quantitative information that may assist in diagnostic and treatment therapy of CSF-related disease cases such as normal pressure hydrocephalus (NPH), Chiari malformation, or syringomyelia.

In Chapter 2, we presented a non-dimensional model of the oscillatory flow in the cerebral aqueduct that incorporates all the relevant parameters of the flow to estimate the dimensionless pressure difference across the cerebral aqueduct from the third to the fourth ventricle. This pressure difference provides an estimate for the transmantle pressure (i.e. the instantaneous pressure difference between the ventricles and subarachnoid space in the brain). Its value was found to be a few pascals, consistent with previously reported invasive pressure measurements. This finding poses important questions to be addressed in the future: how does the transmantle pressure vary for healthy individuals? Can transmantle pressure be used to differentiate between healthy individuals and those with NPH?

In an attempt to answer some of the former questions, in Chapter 3 we implemented our model to compute the transmantle pressure. The study involved a large cohort of healthy individuals with ages ranging from 25 to 92 years. The results indicate that there

may be an influence of age on the magnitude of the corresponding transmantle pressure, although this result needs further corroboration. The preliminary results of the validation exercises presented in Chapter 4, involving canonical in-vitro experiments, suggest that our model captures with sufficient accuracy the flow behavior observed in the aqueduct and also provides an avenue for future studies involving a more detailed examination of the velocity field.

Future studies are warranted involving disease cases of interest, in particular NPH. Previous investigations have utilized the flow rate and stroke volume [1, 2] to guide NPH diagnosis or shunt responsiveness assessments, with limited success [3]. As an alternative, we postulate that transmantle pressure plays a role in the development of ventriculomegaly characterizing NPH [4] and therefore can be used as a clinical quantitative parameter. The disease progresses insidiously over long periods, over which the individual experiences many million cardiac cycles, suggesting that we are dealing with a problem described in engineering applications as fatigue. In essence, we hypothesize that in individuals with elevated transmantle pressure differences (but otherwise normal intracranial pressure), cyclic loading may lead to an increase in the recovery time of the brain tissue and a gradual strain accumulation that ultimately produces enlargement of the ventricles. Thus, transmantle pressure should be investigated as an alternative parameter in future clinical studies to settle the debate on its relevance in NPH, particularly for ventriculomegaly.

Regarding the pulsatile flow along the spinal canal, we presented in Chapter 5 a one-dimensional model that was able to reproduce the amplitude decay and phase lag of the measured flow rates at various locations along the spinal canal, yielding results in agreement with previous reports [5, 6]. This model depends on information that can be obtained directly from MRI measurements, such as the geometry of the canal, but also requires both the ICP waveform and knowledge of the variation of the canal compliance and the density of the trabeculae along the spinal canal, which cannot be measured by MRI. Preliminary computations using an assumed ICP waveform together with educated

estimates for the constant canal compliance and trabeculae resistance provided qualitatively correct flow rate predictions for two different subjects. To further investigate our model, we performed in Chapter 6 additional tests by varying the morphology of the ICP waveform. We found that it does visibly alter the resulting flow rate measurements. And since direct ICP measurements might not be easily accessible, an alternative validation method has also been proposed using lumbar pressure measurements, with preliminary observations showing promising potential.

Having the ability to estimate the temporal variation of the ICP non-invasively has been stated as the "holy grail" in the medical community. Based on the preliminary results in Chapter 6, we believe that our model has the potential to determine the temporal variation of the ICP based on non-invasive flow-rate measurements along the spinal canal, but much remains to be done. For example, we are currently investigating the use of an in-silico data set for a simple multi-output Convolutional Neural Network (CNN). The CNN can be developed to output the corresponding ICP signal from the measured flow rate MRI measurements. In addition, future efforts to investigate the accuracy of the spinal-canal model should consider in-vitro experiments involving 3D-printed MRI-compatible models.

In conclusion, we believe that the models, results, and preliminary validation on the flow in the cerebral aqueduct and spinal canal presented in this dissertation constitute a critical step in our efforts to develop tools that can help clinical researchers investigate CSF-related disorders.

Bibliography

[1] William G Bradley Jr, David Scalzo, John Queralt, Wolfgang N Nitz, Dennis J Atkinson, and Priscilla Wong. Normal-pressure hydrocephalus: evaluation with cerebrospinal fluid flow measurements at mr imaging. *Radiology*, 198(2):523–529, 1996.

[2] Geir Ringstad, Kyrre Eeg Emblem, and Per Kristian Eide. Phase-contrast magnetic resonance imaging reveals net retrograde aqueductal flow in idiopathic normal pressure hydrocephalus. *Journal of Neurosurgery*, 124(6):1850–1857, 2016.

[3] A Scollato, R Tenenbaum, G Bahl, M Celerini, B Salani, and N Di Lorenzo. Changes in aqueductal csf stroke volume and progression of symptoms in patients with unshunted idiopathic normal pressure hydrocephalus. *American journal of neuroradiology*, 29(1): 192–197, 2008.

[4] David N Levine. Intracranial pressure and ventricular expansion in hydrocephalus: have we been asking the wrong question? *Journal of the neurological sciences*, 269 (1-2):1–11, 2008.

[5] N Yallapragada and N Alperin. Characterization of spinal canal hydrodynamics and compliance using bond graph technique and csf flow measurements by mri. *Proc Int Soc Magn Resonan Med*, 11:2658, 2004.

[6] Kevin M Tangen, Ying Hsu, David C Zhu, and Andreas A Linninger. Cns wide simulation of flow resistance and drug transport due to spinal microanatomy. *Journal of biomechanics*, 48(10):2144–2154, 2015.